Thomson Scattering Measurements in MAST-U Super-X Divertor Plasmas

by

James George Clark

University of Liverpool

Department of Electrical Engineering and Electronics

Supervised by:

Dr Mark Bowden
Department of Electrical Engineering and Electronics
University of Liverpool

Dr Rory Scannell
Mega-Ampere Spherical Tokamak - Upgrade
United Kingdom Atomic Energy Authority

Thesis submitted in accordance with the requirements of the University of Liverpool for the degree of Doctor in Philosophy by James George Clark

March 2023

Dedicated to

Gary Clark and Roger Terence Hough

Abstract

In the field of nuclear fusion research plasma diagnostics are vital. They provide measurements of key plasma properties and are used to assess the performance of experiments and inform theoretical models. Thomson scattering uses high power monochromatic laser light that is injected into the plasma. Based on the wavelength of the light collected from the plasma, electron density and temperature values can be obtained at very high spatial resolution using bespoke spectrometers. The temporal resolution is determined by the repetition rate of the laser used. Thomson systems can consist of multiple spectrometers and lasers to improve the spatial and temporal resolution in order to measure certain physical phenomena.

In the current generation of tokamaks the power loading in the exhaust is unsustainable for future tokamaks operating to produce power. To study this the Mega-Ampere Spherical Tokamak-Upgrade (MAST-U) has installed a "Super-X" divertor configuration to test a solution to the exhaust problem. A low temperature Thomson scattering system has been installed in the lower Super-X divertor. This system produces electron density and temperature profiles in this region of the plasma which has shown typical electron density and temperature values in the Super-X divertor to be $\sim 1 \times 10^{19}\,\mathrm{m}^{-3}$ and $\sim$1 eV respectively. Despite operating in attached and detached conditions at a range of plasma current and fuelling levels, the electron temperatures showed little variation on the order of a few electron-volts. This data enabled study of the electron parameters during the detachment process to assess the performance of the Super-X divertor as an exhaust solution. It is shown that the divertor Thomson system is capable of diagnosing a rollover in the electron density measured in the Super-X chamber. These measurements showed good agreement with the ion saturation current measurements from Langmuir probes near the divertor strike point. While observing the rollover it was also

shown that there was little effect of the electron properties in the midplane SOL when the Super-X divertor entered a detached state. Comparisons to other divertor diagnostics such as various spectroscopy systems are presented in this thesis and compare favourably. Higher power experiments will be run in the future to see how the Super-X divertor will scale for the power loading levels in the next generation of tokamaks. The results presented in this thesis show that the effect on the electron population in the MAST-U core and divertor is promising for these future experiments.

Acknowledgements

The work presented in this thesis would not be possible without the help and support of a number of people that are gratefully acknowledged here.

Firstly I would like to thank Dr Mark Bowden, without your willingness to accommodate a student at the other end of the country, this project would not have been possible.

I would like to sincerely thank Dr Rory Scannell, your knowledge of all things MAST-U and diagnostics, particularly Thomson scattering, has been invaluable to this work. Having the opportunity to work of someone of your calibre and standing in the field has been a privilege and your enthusiasm for all things Thomson has inspired me greatly. Without your direction, open door and eagerness to help me solve even the stupidest of problems, this project would have been a very different experience.

I would like to sincerely thank Chris Hickling for always being there during the peaks and troughs associated with research. Starting out in the field as two undergraduates from a University nobody had ever heard of, massively out of their depth, all the way through to completing doctorates with as many house moves as years experience along the way has been one hell of a ride. I wish you all the success in the future and I hope our paths cross again wherever we both end up.

UKAEA has been a fantastic place to work during the course of my time on MAST-U. I have been afforded the opportunity to work alongside some of the best fusion scientists in the field and the ability to pick their brains has been a particular highlight. In particular I would like to thank Dr Andrew Kirk, Dr James Harrison and Dr Kevin Verhaegh for their expertise and insight at various points throughout this work.

There are too many to name but without the many students who make up

the Fusion CDT, the York Plasma Institute and those who have passed through D3/2.15 at various times, my PhD would have been a much less enjoyable experience.

I would like to thank Ann and Alan Hickling for your assistance during various house moves around the country over the last six years and your endless supply of someone else's furniture to furnish a property at short notice.

I would like to thank Dr Fenton Glass, Dr Thomas O'Gorman and Dr Tom Carlstrom for your assistance and expertise remotely during my work on DIII-D while I was on the wrong side of the Atlantic. Navigating this would have been tricky at any point let alone during a global pandemic.

I would like to thank Janet and Andrew (Jandy) Smith for your constant support, life advice and endless enthusiasm for my work. Your generosity, humour and willingness to welcome me into your family as 'part of the furniture' means more than you will ever know. This experience would have been a great deal poorer without you both as part of it.

I would like to thank Dandy for your company during the majority of this write up and your ability to perk up and create as much noise as possible whenever I was on an important call.

I would like to sincerely thank Christine Hough for always fighting my corner. None of what I have achieved both inside and outside of academia would have been possible without your endless love and support. Your advice has always been invaluable and your presence during the darkest times in my life, particularly those during my PhD, is something I will never be able to thank you for.

Finally I would like to sincerely thank Laura Smith for your love and support throughout the various personal and professional challenges that have arisen in the past six years. None of this would have been possible without you by my side, in particular your support during the Covid-19 lockdowns and the writing of this thesis as I worked towards "sixteen sixteenths". The sacrifices you have made to support me during this work are something I will be eternally grateful for and I look forward to our adventures in the future and wherever life takes us.

Declaration

I declare that the work presented in this thesis, other than contributions cited or acknowledged in the text, is my own.

James George Clark

March 2023

Publications

The work carried out in support of this thesis has contributed to a number of publications either as lead investigator or as a co-author. In the case of the latter, the contribution to the work was either novel data analysis or comparison to plasma diagnostic systems beneficial to the research. The work in these publications covers a variety of topics within magnetically confined fusion research such as pedestal physics, exhaust physics and plasma diagnostic development.

J. G. Clark, M. D. Bowden and R. Scannell. *Low temperature Thomson scattering on MAST-U.* Rev. Sci. Instrum. **92**, 043545 (2021)

S. F. Smith, A. Kirk, B. Chapman-Oplopoiou, J. G. Clark, C. J. Ham, L. Horvath, C. F. Maggi, R. Scannell, S. Saarelma and the MAST Team. *Pedestal analysis of MAST ELMy regimes.* Plasma Phys. Controlled Fusion **64**, 045024 (2022)

J. G. Clark, M. D. Bowden, Y. Kim, B. Parry, E. Rose, R. Sarwar and R. Scannell. *First divertor Thomson scattering measurements on MAST-U.* Rev. Sci. Instrum. **93**, 103534 (2022)

J. G. Clark, M. D. Bowden, J. R. Harrison and R. Scannell. *Thomson scattering measurements in MAST-U Super-X divertor plasmas.* Proc. 48th European Conference on Plasma Physics, (2022)

K. Verhaegh, B. Lipschultz, J. R. Harrison, N. Osborne, A. C. Williams, P. Ryan, J. Allcock, J. G. Clark, F. Federici, B. Kool, T. Wijkamp, A. Fil, D. Moulton, O. Myatra, A. Thornton, T. O. S. J. Bosman, C. Bowman, G. Cunningham, B. P. Duval, S. Henderson, R. Scannell and the MAST

Upgrade Team. *Spectroscopic investigations of detachment on the MAST Upgrade Super-X divertor*. Nucl. Fusion. **63**, 016014 (2023)

R. Scannell, J. G. Clark, Y. Kim, D. Kos, M. Maslov, and L. Giudicotti. *Polarimetric Thomson scattering measurements in JET high Temperature Plasmas*. Rev. Sci. Instrum. **94**, 013506 (2023)

Contents

List of Figures

List of Tables

Acronyms

AOI Angle of incidence

APD Avalanche photodiode

CAD Computer Aided Design

CCFE Culham Centre for Fusion Energy

ELM Edge Localised Mode

FIG Fast ionisation gauge

GDC Glow discharge cleaning

HeNe 656nm wavelength Hellium-Neon laser

ITER International Thermonuclear Experimental Reactor

LIDT Laser induced damage threshold

MAST Mega Ampere Spherical Tokamak

MAST-U MAST-Upgrade, upgraded version of MAST

Nd:YAG Neodymium-doped Yttrium alluminium garnet

NTM Neoclassical Tearing Mode

PCB Printed circuit board

PCI Peripheral Component Interconnect

QE Quantum efficiency

SOL Scrape-off layer

ST Spherical Tokamak

START Small Tight Aspect Ratio Tokamak

TS Thomson scattering

UFDS Ultra fast divertor spectroscopy

Chapter 1

Introduction

This chapter provides a background to the underlying theory and techniques relevant to the work carried out in support of this thesis. Section 1.2 covers the use of nuclear fusion and its fuels as a potential energy source and its use in magnetically and inertially confined fusion experiments. Section 1.3 introduces the tokamak and the reasons behind its development into the primary device for magnetically confined fusion research.

Section 1.4 introduces the MAST-U tokamak and its development based on previous incarnations of spherical tokamak into the United Kingdoms flagship fusion experiment in 2023. Section 1.5 details the basic concept of the scrape-off layer and its importance to current magnetically confined fusion research. Section 1.6 outlines the function of a divertor and its role in future fusion devices. The Super-X divertor and the principles that have led to its study in relation to the conventional divertor configuration are also discussed.

Section 1.7 gives a summary of divertor detachment and the physical processes that govern it as a potential solution to the exhaust problem for the future generation of tokamaks. Section 1.8 gives a summary of Thomson scattering and its place in current magnetically confined fusion research, particularly the development of low temperature Thomson scattering systems for MAST-U.

Section 1.9 provides an overview to some of the diagnostics that are used to assess the performance of MAST-U and analyse some of the experiments that were carried out during the work of this thesis, as discussed in Chapter 5. Section 1.1 gives a summary of the subsequent chapters of this thesis.

1.1 Thesis Outline

This thesis consists of six chapters. Chapter 1 outlines the key topics and techniques relevant to the work carried out in support of this thesis. Chapter 2 presents a review of the basic physics that govern a plasma, including the properties of plasma that permit the scattering of electromagnetic radiation, particularly Thomson scattering. A review of the Thomson scattering spectrum and its relevance to the work carried out on MAST-U, with a particular focus on the low electron temperature region of the scattering spectrum, is also discussed in Chapter 2. Chapter 3 introduces the MAST-U divertor Thomson scattering system where the optical and electrical setup is detailed as well as the procedure carried out to generate electron density and temperature values from the scattered signals measured by the diagnostic. Chapter 4 covers calibration of the MAST-U divertor Thomson scattering system. The calibration procedures for each of the MAST-U Thomson polychromators is described. Work carried out to optically align the system and absolutely calibrate the system via rotational Raman scattering is also discussed in this section. Chapter 5 presents the main body of results obtained from Super-X divertor experiments on the MAST-U tokamak and compares the electron density and temperature measurements to observations made on other tokamaks during detachment experiments and other diagnostic systems operating during the same MAST-U plasmas. Conclusions on the research presented in Chapters 3-5 and suggestions for future work based on the results presented in this thesis are outlined in Chapter 6.

1.2 Nuclear Fusion

Since the middle of the 20th century nuclear fusion has been viewed as a potential energy source. Many in the energy sector earmarked fusion as a power source with essentially limitless capacity, but more importantly in the immediate future, one that produces minimal CO_2. For this reason fusion has long been viewed at as the natural successor to fossil fuels as the main energy source for large scale power networks.

While the degree of nuclear waste produced by nuclear fusion reactors is a

debated topic, it is accepted that they will produce significantly less nuclear waste than fission alternatives. A viable fusion reactor will almost certainly utilise one of the following reactions involving Deuterium (D) and Tritium (T) [1]:

$$
\begin{aligned}
{}^{2}_{1}\mathrm{D} + {}^{3}_{1}\mathrm{T} &\rightarrow {}^{4}_{2}\mathrm{He} + {}^{1}_{0}\mathrm{n} + 17.6\,\mathrm{MeV} \\
{}^{2}_{1}\mathrm{D} + {}^{2}_{1}\mathrm{D} &\rightarrow {}^{3}_{2}\mathrm{He} + {}^{1}_{0}\mathrm{n} + 3.27\,\mathrm{MeV} \\
{}^{2}_{1}\mathrm{D} + {}^{2}_{1}\mathrm{D} &\rightarrow {}^{3}_{1}\mathrm{T} + {}^{1}_{1}\mathrm{H} + 4.03\,\mathrm{MeV}
\end{aligned}
$$

The cross sections for these reactions can be seen in Figure 1.1. The cross section for each of the D-D reactions is similar and as a result the curve for the D-D reaction is the sum of the two. It can be seen that the D-T reaction not only has the largest cross section but it also occurs at the lowest energy, making it the most viable.

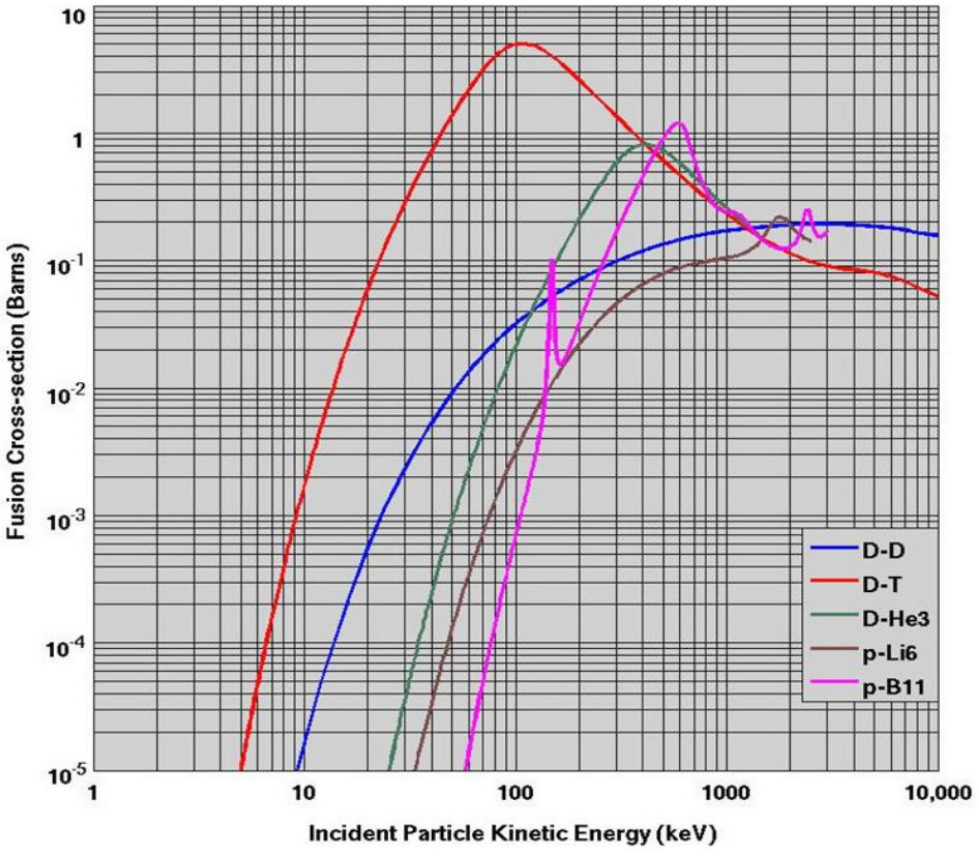

Figure 1.1: Fusion cross sections [2]

In terms of public research there are generally two streams which are working towards the energies needed to utilise one of these reactions. One is inertial confinement where small pellets of a D-T fuel mix are heated with very high energy

laser pulses to initiate the reaction. The other method is magnetically confined fusion where a gas in a vacuum chamber is heated to extremely high temperatures where it transitions to a plasma. At this point the plasma can be controlled with magnetic fields to keep the plasma from touching the walls and cooling. While there are a number of different devices capable of confining a high temperature plasma, historically research has focused around a device called a tokamak. There are a number of different types of tokamak but the work in this thesis will focus on specific areas of one particular type of tokamak, the spherical tokamak.

1.3 Tokamaks

The term Tokamak is a Russian acronym from the phrase "toroidal'naja kamera s magnitnymi katushkami" which roughly translates to "toroidal chamber in magnetic coils". Originating in Russia, the tokamak was shown to generate much higher plasma temperatures than had been achieved in the rest of the world by the late 1960s [3]. Since then the tokamak has largely been the plasma confinement device of choice for large scale experimental fusion research. There are a number of different tokamaks around the world with each device generally specialising in a certain area of fusion research as part of the global pursuit of power generation from nuclear fusion. A basic representation of a tokamak can be seen in Figure 1.2.

The tokamak and its toroidal shape allow the plasma to wrap around allowing additional coils to be positioned closer to the plasma to improve the radial confinement. However these coils alone are not enough to confine the plasma to achieve fusion relevant conditions. The plasma acts as the secondary coil of a transformer with the poloidal field coils being the primary loop. This field adds a twist to the magnetic field lines to help the confinement but it also provides ohmic heating to the plasma due to its inherent resistance. Even though the plasma produces its own poloidal field, additional coils are required to stop the plasma from drifting outwards radially. This is to be avoided as any contact with the walls will cause a dramatic loss in the energy stored in the plasma and can even cause the plasma to dissipate. As a result there has been decades of research into plasma surface interactions as part of the various fusion experiments around the world.

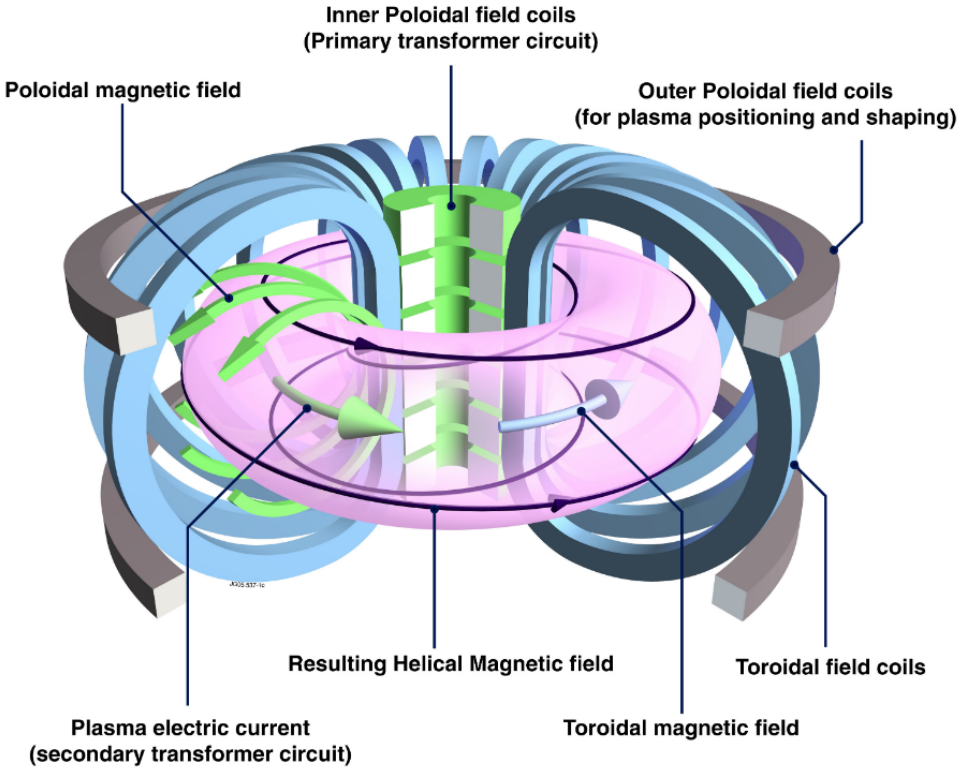

Figure 1.2: A basic representation of the coils on a tokamak, image courtesy of EUROfusion

1.4 MAST-U

The spherical tokamak (ST) is a variation of the 'conventional' tokamak that is closer to spherical than the toroidal shape of conventional tokamaks. Spherical tokamaks are defined by their small aspect ratio, the ratio between the major, R, and minor radius, r. The first spherical tokamak, START, was built at Culham in 1990 and operated until 1998 when it was retired to build a more sophisticated experiment, MAST which operated from 1999 to 2013. Over the course of its operation MAST conducted 30,471 experiments and was a resounding success, consolidating the promise shown by START that the spherical tokamak was a worthwhile area of research for fusion power generation. As a result a £45 m upgrade of MAST commenced in 2013 and first plasma was achieved on MAST-U in October 2020. Despite it only being an upgrade by name, MAST-U is effectively a new tokamak with nearly every major component apart from the vacuum vessel being replaced. A comparison of the engineering parameters for MAST and MAST-

U can be seen in Table 1.1

Parameter	MAST	MAST-U
Major radius (m)	0.85	0.85
Minor radius (m)	0.65	0.65
Plasma current (MA)	1.3	2.0
Magnetic field at R = 0.85 m (T)	0.52	0.75
Total NBI power (MW)	3.8	5.0
On-axis NBI power (MW)	3.8	2.5
Off-axis NBI power (MW)	0.0	2.5
Pulse length (s)	0.6	5.0

Table 1.1: Comparison of engineering parameters for MAST and MAST-U taken from MAST-U research plan [4]

MAST-U is located at the CCFE in Oxford, England. It features a large suite of diagnostics that measure a wide variety of physical phenomena all over the tokamak. One of the goals of the upgrade was to implement a novel "Super-X" divertor configuration which was built to further study the area of divertor physics. MAST-U completed its first physics campaign in 2021. One of the goals of these experiments was to characterise the Super-X divertor and study the mechanisms behind the detachment process. This divertor study is part of a campaign of research being undertaken around the world in the run up to ITER which is a next generation tokamak being built in the south of France which is currently predicted be begin plasma operations in the early part of the 2030s.

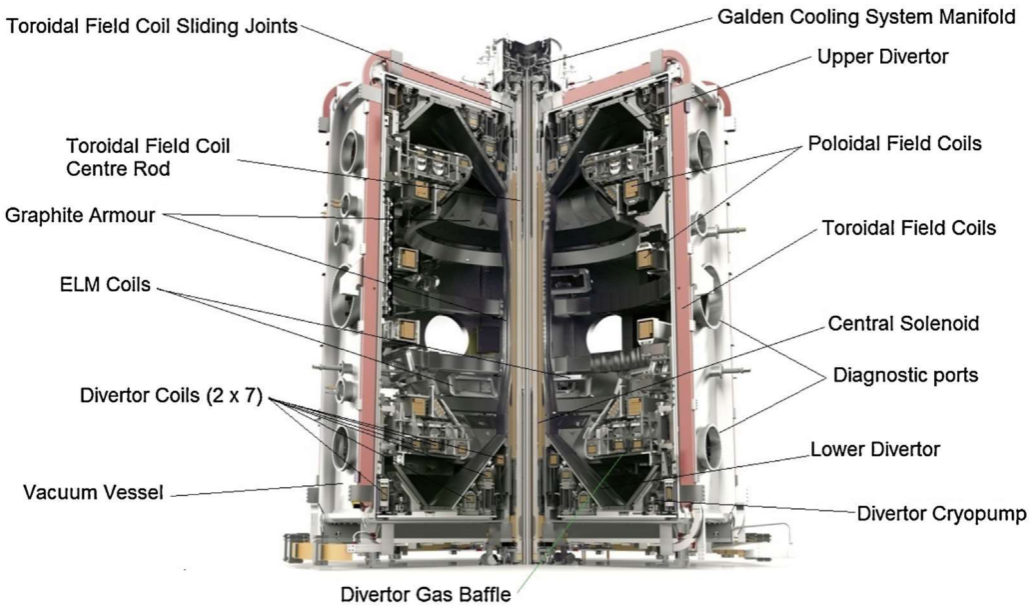

Figure 1.3: A cross section of the new MAST-U vessel [5]

1.5 Scrape-off Layer

The scrape-off layer (SOL) is an area of open magnetic field lines created by cross-field transport. It is a heavily studied area of the tokamak as the field lines extend out onto the plasma facing components. If the generation of the SOL is considered as purely a diffusive process the radial width is given by:

$$\lambda_{SOL} = \left(\frac{D_\perp L_\parallel}{C_s} \right)^{1/2} \tag{1.5.1}$$

where $D_\perp$ is the radial diffusion coefficient, $L_\parallel$ is half the distance along an open field line between two surfaces intersecting the plasma and C_s is the plasma sound speed given by $C_s = (2T_s/m_e)^{1/2}$ where T_e and m_e are the temperature and mass of the electron respectively. Typical values on MAST-U are a couple of centimetres.

While the SOL width is not a quantity that is directly controlled during tokamak operation it still needs to be considered as its width has a big impact on the heat and particle fluxes seen by the plasma facing components. For the purposes of this calculation it is assumed that the difference in electron and ion temperature is negligible. Given the typical electron and ion temperatures in the SOL in comparison to those in the plasma core this is a reasonable approximation.

1.6 Divertors

The divertor is an area found at the poloidal limits of a tokamak in the scrape-off layer, as seen in Figure 1.4. While the geometry of a divertor will vary with each device, most tokamaks operating in the present day have some form of divertor configuration. In practice, a divertor consists of a number of dedicated coils that manipulate the poloidal magnetic field away from the core of the plasma on to a dedicated surface, known as the strike point, which is chosen to handle large heat and particle fluxes. These additional coils create a "null" in the poloidal magnetic field and a region of open field lines extending outwards radially. The magnetic null is often referred to as the X-point due to the shape it makes on a magnetic equilibrium. The last closed flux surface is sometimes referred to as the separatrix due to the transition between open and closed field lines and can be seen as the thick blue line in Figure 1.5.

Despite causing a drop in plasma temperature and confinement conditions, plasma surfaces and the reaction between the plasma and plasma facing components is a key area of fusion research. In current generation tokamaks most of this is focused towards the divertor. Heat flux levels observed in conventional divertor devices are unsuitable for next generation devices based on the current $10\,\mathrm{MWm^{-2}}$ material limit. Advanced divertor concepts such as the Snowflake [6] and Super-X [7] are being investigated as methods of reducing the heat flux experienced at the divertor strike point. The MAST-U divertor is capable of both Super-X and Snowflake geometries as well of variations of these concepts to alter the magnetic flux expansion reaching the target. The aim of the research into these configurations is to deliver a successful power loading solution that will enable future devices such as ITER [8] and STEP [9] to operate with viable plasma facing component lifetimes.

Operating a tokamak with a divertor configuration has shown to have a number of benefits by trapping neutral species away from the plasma and subsequent removal of species contaminating the confinement of the core plasma. These play a key role in the transition to the high confinement (H-mode) operating regime [10]. Divertors also facilitate a process called detachment, as described in Section 1.7, where the power and particle flux delivered to plasma facing components is signif-

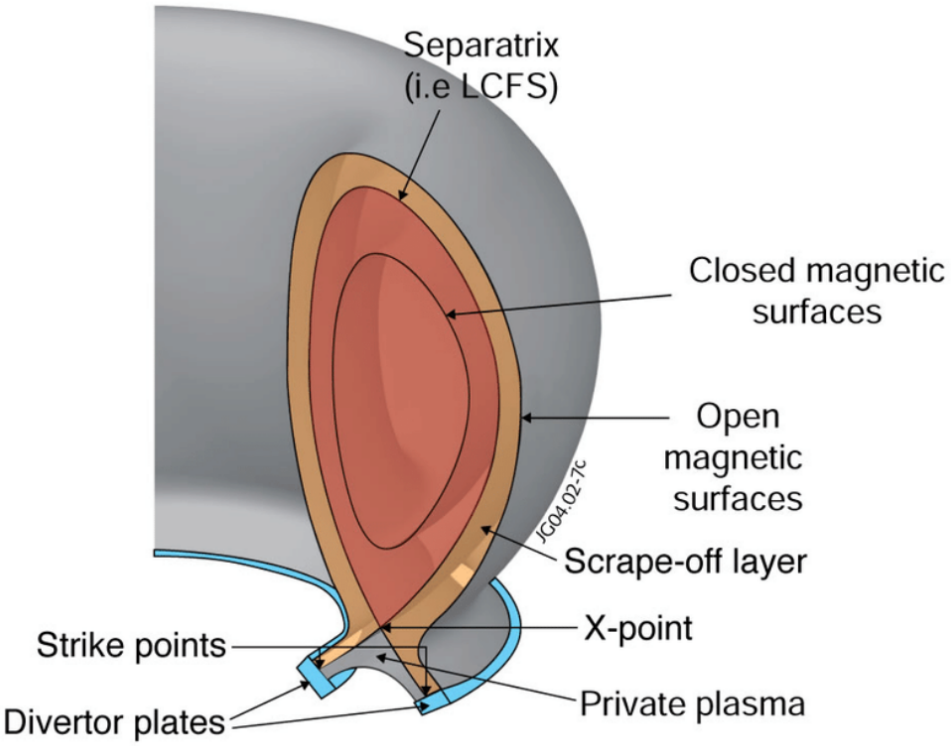

Figure 1.4: A cut through of a tokamak showing the divertor and edge regions, image courtesy of EFDA-JET

icantly reduced. The Super-X divertor [7] on MAST-U and a comparison to the conventional divertor configuration can be seen in Figure 1.5.

The dedicated divertor coils increase the connection length of the magnetic field lines to the divertor and increase the magnetic flux expansion to an area of increased radius and lower magnetic field. By increasing the magnetic flux expansion the wetted area on the divertor tiles is increased, which reduces the heat and particle fluxes to the surface. In addition to magnetic coils the divertor is baffled which helps trap neutral particles [11] which can escape out of the divertor and move back upstream to the core. This will further reduce the temperature at the target due to plasma-neutral interactions. It has also shown to reduce the power threshold required to enter H-mode, even when operating in a conventional divertor.

To measure the properties of the plasma in the Super-X chamber a number of diagnostics have been installed. Some of these include Langmuir probes [12], infrared thermography [13], multi-wavelength imaging [14], emission spectroscopy [15] and a divertor Thomson scattering system [16, 17].

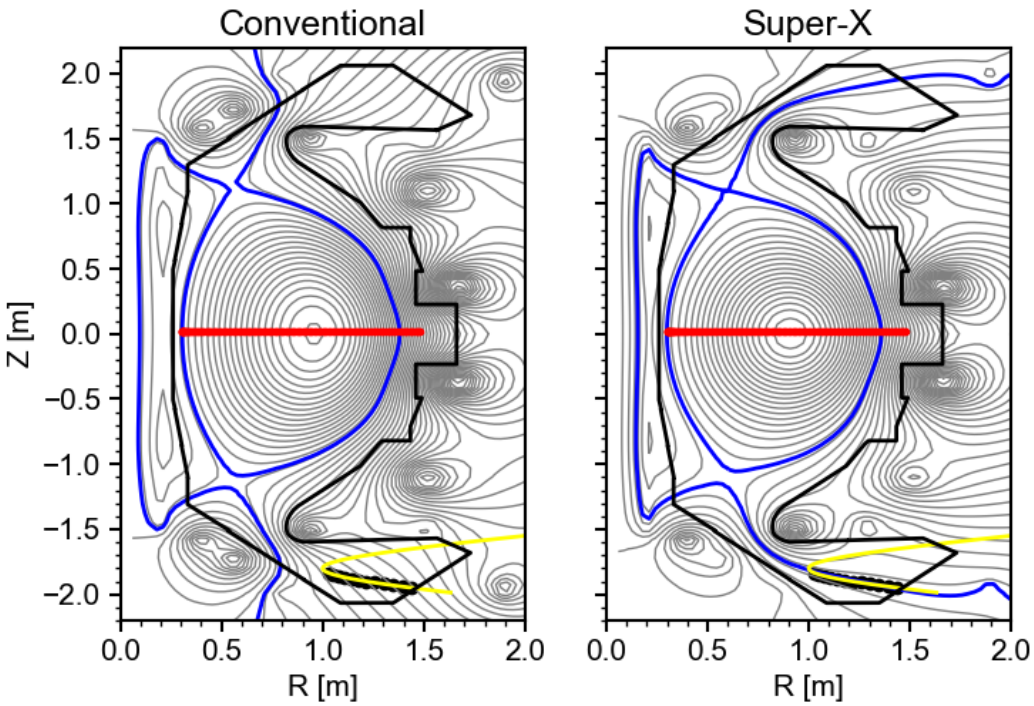

Figure 1.5: A comparison between the magnetic equilibrium reconstruction of a conventional and Super-X divertor configuration on MAST-U with the core (red) and divertor (black) Thomson scattering locations with the divertor laser beam path (yellow)

1.7 Divertor Detachment

While the final purpose for the divertor on a power producing fusion reactor will be to extract heat, on current experimental devices the divertor is principally for the study of access to detachment. It is not universally accepted why this occurs, but the physical mechanisms that result in detachment are very well studied and generally agreed upon.

When a divertor becomes detached a drop in the heat flux and ion flux to the divertor target is observed. When one of these energetic ions is carried along a magnetic field line to the divertor tile it impacts the surface and a process known as secondary emission occurs where electrons from the surface are liberated due to the energy of the incident ion. The two opposing charges combine to produce a neutral atom which is unperturbed by the magnetic field in the divertor. As the atom retains a non-zero kinetic energy it will continue to travel through the plasma until it undergoes an impact which re-ionises the atom. This process dissipates energy from the plasma and is known as recycling.

If the ion flux continues to increase then the number of neutrals generated from recycling will continue until a point where so much energy is dissipated from the plasma that it becomes so cold and de-ionised that it barely functions as a plasma. This is typically promoted by increasing the electron density in the core, upstream of the divertor, with an increase in fuelling which in turn leads to an increase in the ion flux entering the divertor. As continued increases in ion flux lead to continued energy loss from the plasma the result is a drop in temperature near the target. This will continue until the plasma becomes so cold that there is little ionisation, at this point the electron density begins to drop. This observed drop in density, specifically in the divertor, is therefore indicative of detachment. For this reason it is generally accepted that for a divertor to be in a detached state electron temperatures at the target will be below $\sim$5 eV. Although the SI unit for temperature is the kelvin (K) in plasma physics electron temperatures are commonly quoted in electronvolts (eV). Each kelvin corresponds to 8.62×10^{-5} eV. This is given by the ratio of the Boltzmann constant k_B ($1.38 \times 10^{-23}\,\mathrm{Jk}^{-1}$) to the elementary charge (1.60×10^{-19} C). As a result each eV is equivalent to 11605 kelvin which is given by $E = k_B T$. For the purposes of this thesis, all electron temperatures from this point will be quoted in electronvolts.

As the electron temperature is dropping at the target as the divertor is approaching detachment, temperature gradients begin to form. The result of this is the region of ionisation moving away from the divertor surface closer to the divertor entrance. As the density and temperature begin to drop at the point of detachment, so does the ion flux to the divertor target. As a result one of the indicators of detachment is the relationship between the target ion flux and the upstream density and the characteristic divertor 'rollover' of the quantities as the ion flux begins to decrease even though the upstream density is increasing.

The effects of this behaviour can be seen physically with diagnostic systems such as multi-wavelength imaging diagnostics [14] that image the emission from energy transitions of particles in the divertor. An image inversion of molecular Fulcher band emission for a MAST-U plasma can be seen in Figure 1.6.

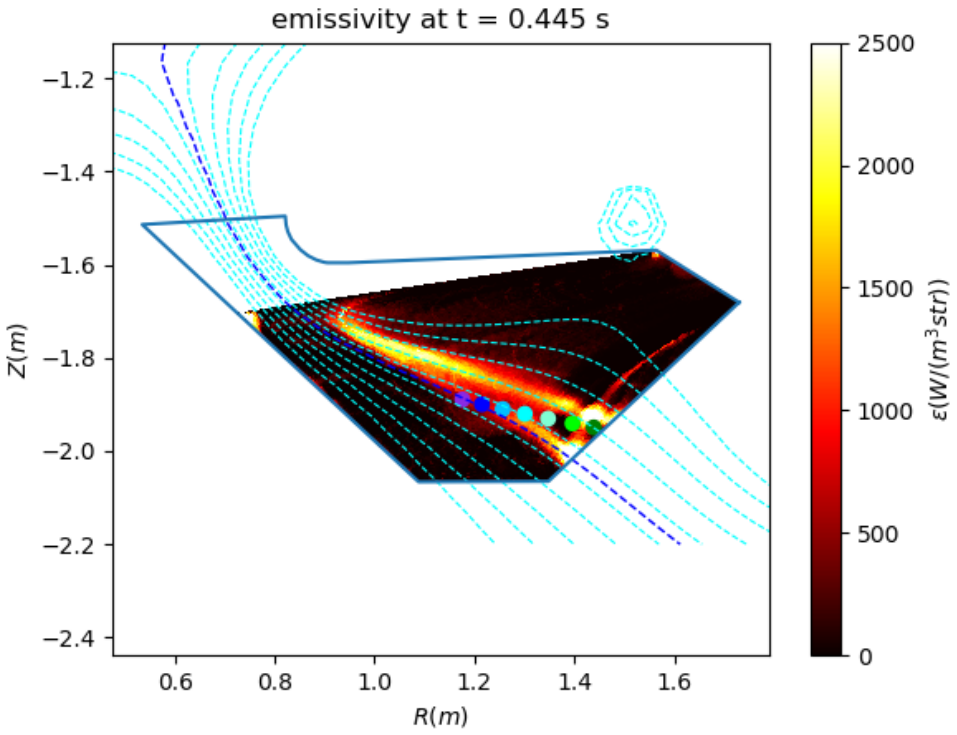

Figure 1.6: Image inversion of molecular Fulcher band emission overlayed with the strike leg position and the divertor Thomson spatial points for MAST-U plasma 45460 at 445 ms. Image provided by T Wijkamp.

1.8 Thomson Scattering

Laser Thomson Scattering, commonly referred to as Thomson Scattering (TS), is an active diagnostic used to measure the density and temperature of plasma species. Lasers have been used to facilitate plasma diagnostic systems for years due to their high power and monochromatic output. They are routinely used as a probing radiation for high temperature fusion plasmas due to their ability to take non-invasive measurements of the electron density and temperature. They were first used to show that tokamaks were capable of confining a plasma with a temperature of several million degrees celcius [3], which laid the foundations for larger modern devices [18].

Considering a simple Thomson scattering experiment, a high power monochromatic laser with a precise line width is directed into a volume of plasma. A collection of high quality optics are located away from the plasma volume to collect the radiation that is scattered from the plasma. Generally in fusion plasmas, and for the purposes of this thesis, the scattering from the plasma is specifically from the electrons.

The optics collect the light to a spectrometer which outputs a spectrum of the light. This can be used to determine the electron properties of the plasma. The width of the spectrum is proportional to the amount of light that has undergone a Doppler shift with the free electrons in the plasma before being collected. The number of photons returned is directly proportional to the density, as a result the area under the returned spectrum is used to determine the density of the plasma. The scattered spectrum can be fitted to a velocity distribution to produce an energy distribution based on the thermal energy of the electrons in the plasma.

It is now common for fusion devices to have at least one Thomson scattering system, usually along the midplane of the device, to measure the electron properties of the confined core. The first divertor based Thomson scattering system was installed on DIII-D [19, 20] and in recent years these systems have become more common [21, 22] including the design [16, 23] and operation [17] of a divertor Thomson scattering system on MAST-U, as seen in Figure 3.1. Previously systems at the edge of the plasma [24] have been utilised. In recent years these have typically been incorporated into upgraded midplane systems that achieve the same

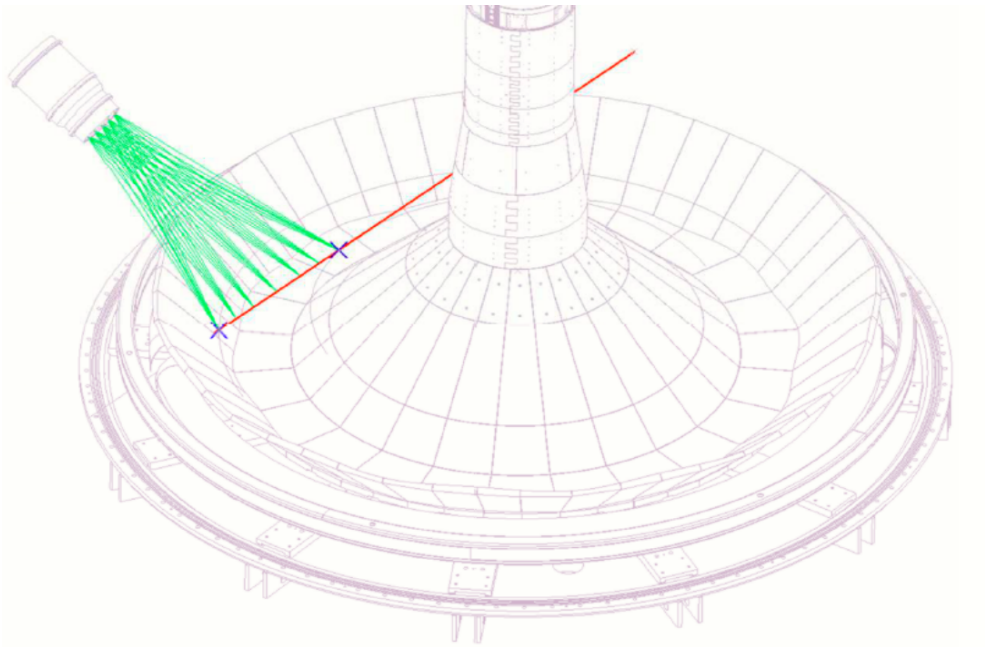

Figure 1.7: A CAD view into the lower Super-X chamber showing the divertor Thomson viewing chord and collection cell without the divertor baffle

high resolution across the whole range of the core plasma. An X-point Thomson scattering system has been designed for MAST-U and will be installed as part of future MAST-U enhancements currently scheduled in 2023.

1.9 MAST-U Diagnostics

In order to understand the context of the experiments carried out and the results presented in Chapter 5 it is worth outlining some of the diagnostics and analysis tools that are routinely used on MAST-U to develop a plasma scenario and interpret the results of an experiment.

1.9.1 EFIT

As detailed in [25] the MAST-U EFIT reconstructs the plasma equilibrium. This is used to check the plasma shape, clearance from surfaces such as the divertor baffle and the strike point position. The latter was of great importance when manipulating the divertor coils to align the strike leg, as seen in Figure 1.8, with the divertor Thomson laser line to optimise the laser alignment during experiments. A qualitative estimate of the flaring of the magnetic field lines can also be inferred

from the spacing of the magnetic surfaces in the divertor.

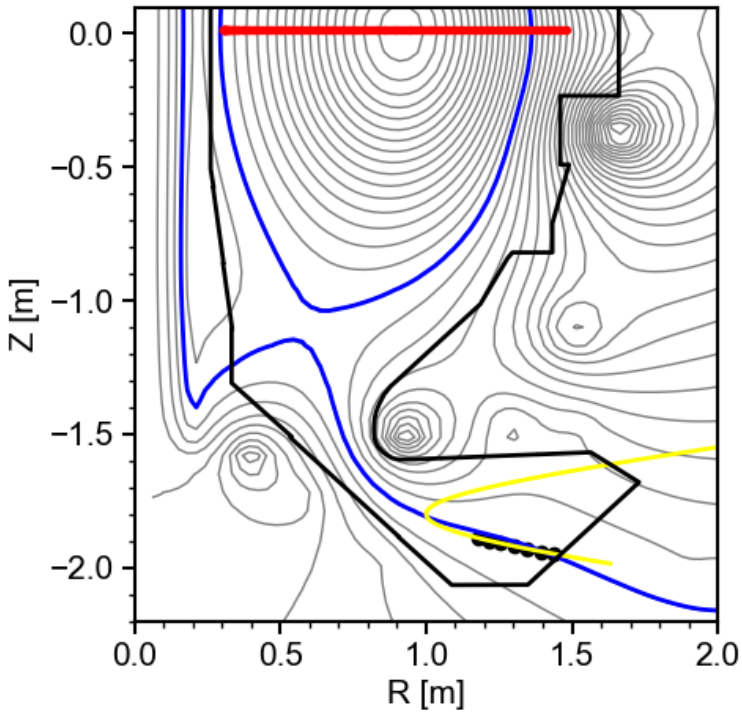

Figure 1.8: Core (red) and divertor (black) Thomson spatial points with laser line (yellow) and separatrix (blue) from MAST-U plasma shot 45463 equilibrium at 0.5 s

1.9.2 Deuterium-alpha Emission

Tokamak plasmas emit a broad band of emission based on the atomic species and energy. One of the most utilised emission lines is the Deuterium-alpha (D_α) Balmer line which occurs in Deuterium at 656.1 nm. Filtered photomultiplier tubes placed around the tokamak allow D_α to be measured at a number of key locations in the plasma such as at the edge, around the X-point and in the Super-X divertor chamber. One of the uses of this diagnostic is its indication of the transition to high confinement H-mode and the presence of edge-localised modes (ELMs) which result in the eruption of particles from the confined core. The presence of regular Type I ELMs [26] can be seen in Figure 1.9 after 300 ms.

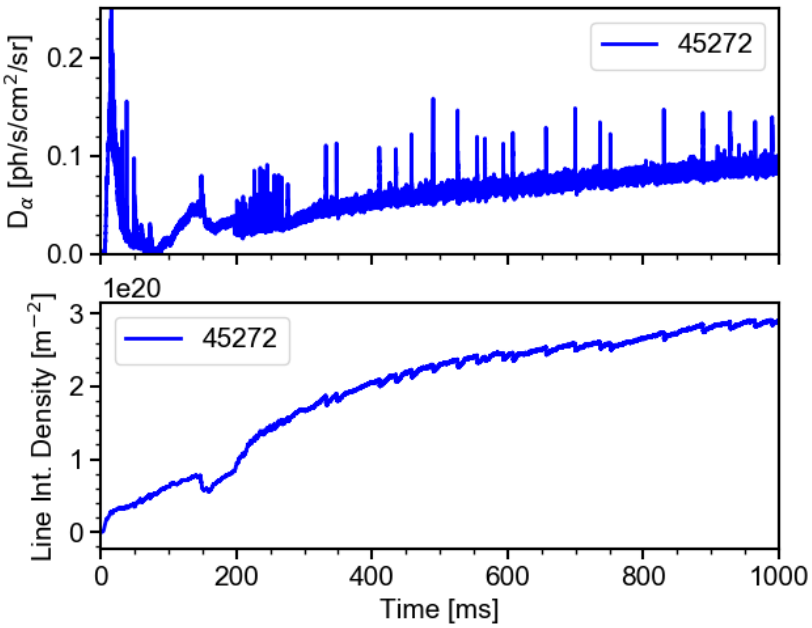

Figure 1.9: MAST-U midplane D_α and interferometer traces

The D_α signal in the lower Super-X chamber is particularly useful to determine when the strike point is swept out from a conventional divertor to Super-X which can be seen Figure 1.10 where a strikepoint sweep begins at 300 ms before reaching Super-X at 400 ms.

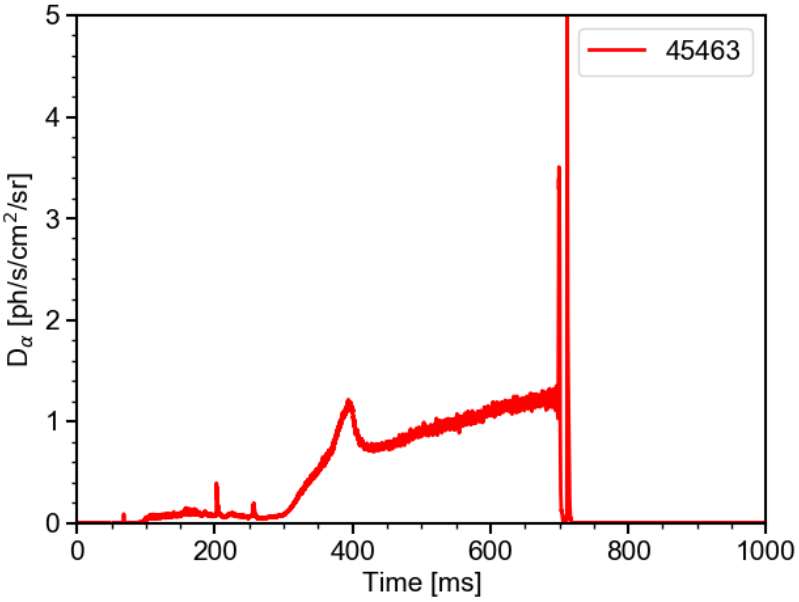

Figure 1.10: MAST-U divertor D_α showing transition to Super-X divertor at 400 ms

1.9.3 Interferometer

As detailed in [27] MAST-U has a real-time interferometer system which produces a line integrated electron density at 4 MHz. This is used to show changes in density during a shot, usually from fuelling or a plasma event. The interferometer can also be used to track the density in the core over a fuelling change either during a single shot density ramp or as a scan over multiple shots. Crashes in the density can be seen during ELMing periods in Figure 1.9 where the D_α spikes line up with the drops in the line integrated density.

1.9.4 Langmuir Probes

A Langmuir probe is a plasma diagnostic used in low temperature [28, 29] and fusion plasmas [12] around the world. MAST-U utilises over 850 probes placed within plasma facing surfaces such as tiles, particularly in the divertor. The Langmuir probe is a physically simple workhorse diagnostic which allows many to be placed around a device. This comes at the cost of complex data analysis based on numerous factors such as the probe tip geometry and the theoretical model applied to the analysis. Langmuir probes measure the current induced by the collection of a mixture of electrons or ions, depending on the polarity of the potential applied to the probe tip. Due to the sheath effects discussed in Section 2.1 this produces a predictable response known as an "I-V characteristic", which can be analysed to find information about electron temperature which is of relevance during magnetically confined fusion research. As well as measurements of electron temperature, the Langmuir probe can be electrically biased to collect only ions and determine the saturation current. This is particularly relevant for probes located in the divertor where ion saturation current measurements are used for detachment studies, particularly in determining the roll-over point as seen in Figure 1.11.

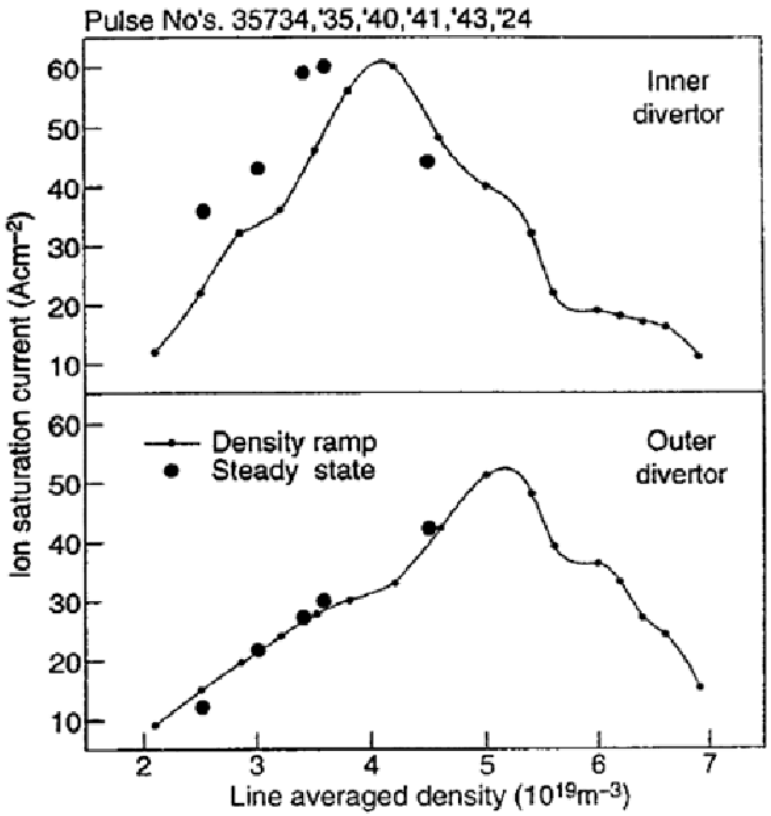

Figure 1.11: Langmuir probe measurements showing ion saturation rollover during divertor detachment. Taken from [30], originally from [31].

Chapter 2

Thomson Scattering Theory

This chapter presents basic theory of a plasma and how those properties are utilised for magnetically confined fusion experiments. Fundamental plasma principles relevant to the propagation of waves in plasmas are presented in Section 2.1 and the scattering of electromagnetic radiation in a plasma is discussed in Section 2.2. An introduction to the Thomson scattering spectrum is outlined in Section 2.3 where the challenges of using a Thomson scattering system to measure down to sub-eV temperatures is discussed.

2.1 Basic Plasma Principles

Due to ionisation, a plasma is fundamentally a sea of ions and electrons. Given the temperature of the plasma, the particles undergo significant motion over small length scales, interacting with a large number of particles. The movement of these free charges leads to electric and magnetic fields being produced from small groups of particles and the flow of charge. These created fields exhibit "collective behaviour" [32] where the fields generated by the movement of the free charges affect other charged particles, even at a considerable distance. The forces experienced by the particles cause the charges to be displaced, this displacement alters the electric field which acts to oppose the change that has been brought about. The inherent frequency at which the particles oscillate due to this interaction is referred to as the plasma frequency ω_p:

$$\omega_p = \left(\frac{ne^2}{\epsilon_0 m}\right)^{1/2} \tag{2.1.1}$$

where n is the plasma density, e is the charge of an electron, ϵ_0 is the permittivity of free space and m is the species mass. A fundamental of any plasma is its ability to shield perturbing charges. Opposite charges form clouds, known as sheaths, around each other. The sheaths screen electric potentials over a very short distance and cause a deviation from the electrostatic interaction which obeys the inverse square law [18]. The distance this occurs over is defined as the Debye length λ_D:

$$\lambda_D = \left(\frac{\epsilon_0 K_B T_e}{ne^2}\right)^{1/2} \tag{2.1.2}$$

where K_B is the Boltzmann constant and T_e is the electron temperature. Plasma appears neutral on scales longer than the Debye length, satisfying the conditions $\lambda_D \ll L$ and $n_e \approx n_i \approx n$. Where L is the length of the plasma and n_e, n_i and n are the density of electrons, ions and the plasma respectively. This is known as quasineutrality [32, 33].

2.2 Scattering of Electromagnetic Radiation

Considering an electron in the plasma, if an incident photon of frequency ω_i has a significantly smaller energy than the energy of the electron ϵ_i before the scattering, such that $\hbar\omega_i \ll \epsilon_i$, the process is Thomson scattering. If the electron is in motion when the scattering occurs, the frequency of the scattered photon will provide information about the velocity of the electron. The contribution of the ion is ignored due to negligible acceleration by the incident photon compared to the contribution made by the electron. This is due to ions having a significantly greater mass. An example scattering scenario with a charged particle can be seen in Figure 2.1.

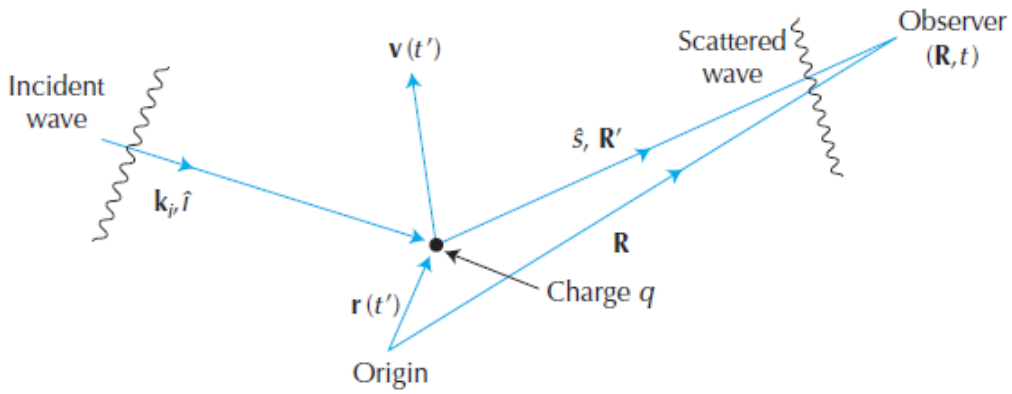

Figure 2.1: Scattering process of an electromagnetic wave incident on a charged particle. Where $\underline{k_i}$ is the incident wave vector, $\hat{i}$ is the unit vector indicating the direction of propagation for the incident wave and $\hat{s}$ is the unit vector pointing from the charge to the observer. $\underline{R'}$ is the position of the observer relative to the charge and $\underline{R}$ is the position of the observer relative to the origin of the coordinate system. $\overrightarrow{v}(t)$ is the velocity of the charge at time t and $\underline{r}(t)$ is the position of the charge relative to the origin at time t. The time when the scattering takes place is given by $t' = t - \frac{R'}{c}$ and is known as the retarded time for radiation observed at a distance $\underline{R'}$ after a time t by the observer [34, 35]. Image taken from [35].

Taking a classical electrodynamics approach for a monochromatic electromagnetic wave incident on an electron with no other forces influencing the electron. If the electron satisfies Equation 2.2.1 where v is the electron velocity and c is the speed of light, relativistic effects are negligible.

$$\frac{v}{c} \ll 1 \tag{2.2.1}$$

As a result, the electric and magnetic field components are given by Equation 2.2.2 and Equation 2.2.3 respectively [34]:

$$\underline{E}_i\left(\underline{r}, t\right) = \underline{E}_{i0}\cos\left(\underline{k}_i \cdot \underline{r} - \omega_i t\right) \tag{2.2.2}$$

$$\underline{B}_i\left(\underline{r}, t\right) = \underline{k}_i \times \frac{\underline{E}_i\left(\underline{r}, t\right)}{c} \tag{2.2.3}$$

The oscillation of these field components accelerates the electron via the Lorentz force:

$$\underline{F} = q\left(\underline{E} + \underline{v} \times \underline{B}\right) \tag{2.2.4}$$

This acceleration causes the electron to re-emit radiation, based on how it was moving prior to the acceleration. This is discussed in further detail by Sheffield et al [35].

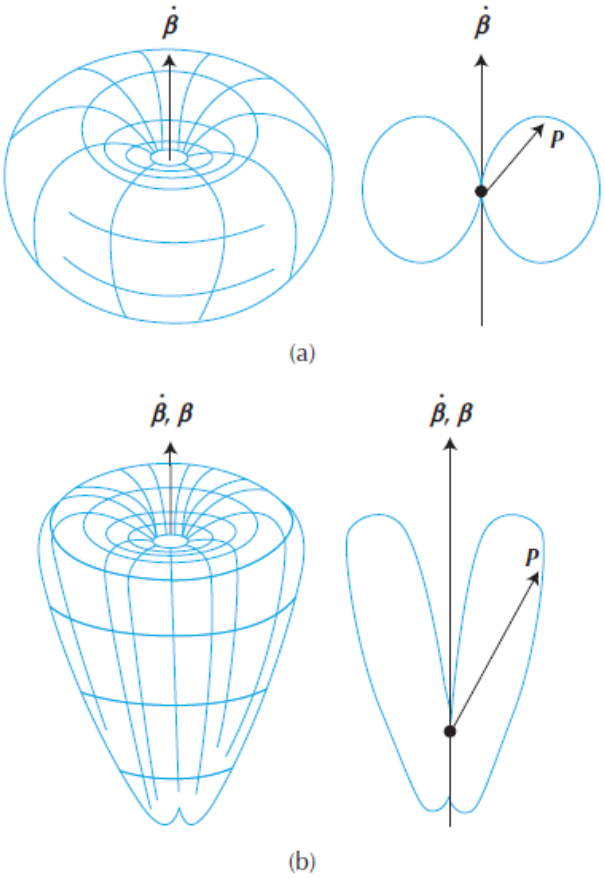

Figure 2.2: Angular variation of power radiated P by an accelerated electron. (a) shows the radiation from a stationary electron, (b) shows the radiation from a charge moving with velocity v where $\beta = \frac{v}{c}$. Image taken from [35].

If the electron has a velocity that satisfies Equation 2.2.1, the contribution of the magnetic field component B is negligible. Using Equation 2.2.4 it can be shown that the equation of motion for the electron is given by Equation 2.2.5 [35]:

$$m_e \left(\frac{d\underline{v}}{dt} \right) = q\underline{E}_{i0} \cos(\underline{k}_i \cdot \underline{r} - \omega_i t) \tag{2.2.5}$$

It can be shown that the electron re-radiates an electromagnetic field that is Doppler shifted, with an E field component of:

$$\underline{E}_s(R,t) = \left(\frac{e^2}{c^2 m_e R} \right) [\hat{s} \times (\hat{s} \times \underline{E}_{i0})] \cos[k_s R - \omega_s t - (\underline{k}_s - \underline{k}_i) \cdot \underline{r}(0)] \tag{2.2.6}$$

where $\omega_s = \frac{(1-\hat{i}\cdot\beta)}{(1-\hat{s}\cdot\beta)}\omega_i$ and $k_s = \omega_s \hat{s}$ are the frequency and wave vector of the scattered wave respectively.

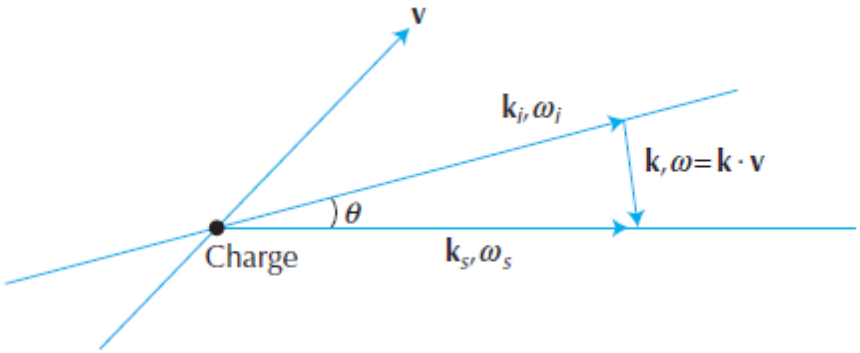

Figure 2.3: A wave vector diagram from a scattering interaction. Image taken from [35].

Using the above quantities, it can be more convenient to describe them in terms of a shift. It can be seen in Figure 2.3 that there is a relationship between the incident and scattered wave vectors where $\omega = \omega_s - \omega_i = (\underline{k}_s - \underline{k}_i) \cdot \underline{v} = \underline{k} \cdot \underline{v}$ and $\underline{k} = \underline{k}_s - \underline{k}_i$ are the scattering frequency shift and wave number shift respectively. These equations are the result of energy and momentum being conserved. They are valid for long wavelengths and resulting low energies, where Compton scattering may be neglected. The relationship between the incident and scattered wave vectors and the scattering angle θ is given by the cosine rule: $|k| = (\underline{k}_s^2 + \underline{k}_i^2 - 2\underline{k}_s \underline{k}_i \cos\theta)^{1/2}$. Again taking the classical case with no relativistic effects for the velocity of the electron, this reduces to $|k| \approx 2|\underline{k}_i| \sin\left(\frac{\theta}{2}\right)$ [35].

$$\frac{dP_s}{d\Omega} = \frac{R^2 c}{4\pi} E_s^2 \tag{2.2.7}$$

where Ω is the solid angle of observation, P_s is the scattered power per unit solid angle of observation $d\Omega$, R is the distance to the observer, c is the speed of light and E_s is the scattered electric field at the position R. Using the previous expression for E_s and averaging over time (denoted by the bar) it can be shown the time averaged scattered power through the unit solid angle $d\Omega$ is:

$$\overline{P_s(\underline{R})} d\Omega = \frac{c E_{i0}^2 r_0^2 d\Omega}{8\pi} [\hat{s} \times (\hat{s} \times \hat{\underline{E}}_{i0})]^2 \tag{2.2.8}$$

where E_{i0} is the magnitude of the incident electric field vector, $r_0 = \frac{e^2}{m_e c^2}$ is the classical electron radius and $\hat{s}$ is the unit vector pointing from the electron to

the observer. As discussed in [35], if the incident EM wave is polarised at an angle ϕ_0 relative to the observer, the $[\hat{s} \times (\hat{s} \times \underline{\hat{E}}_{i0})]^2$ term becomes $1 - \sin^2\theta \cdot \cos^2\phi_0$. If the incident wave is not polarised, an average can be taken over ϕ_0 meaning that the term becomes $1 - \frac{1}{2}\sin^2\theta$. An example of this scenario and its geometry can be seen in Figure 2.4

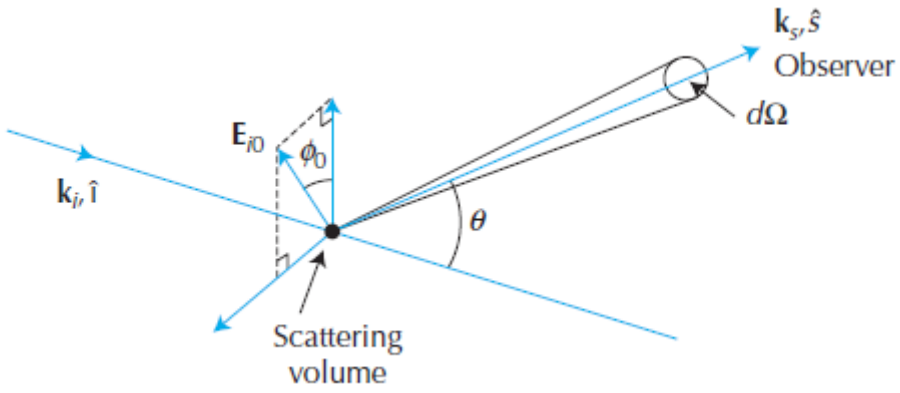

Figure 2.4: The scattering geometry through an angle θ, showing the collected solid angle $d\Omega$ and the relative orientation of the incident polarisation of the E field relative to the observer. Image taken from [35].

Alternative discussions on non-relativistic single electron Thomson scattering are discussed in [34, 36, 37].

The total scattering cross section is defined as the ratio of the total scattered power to the total incident power. This is called the Thomson scattering cross section [34–36]:

$$\sigma_T = \frac{8\pi}{3} r_0^2 \tag{2.2.9}$$

Considering scattering from multiple electrons in the plasma, Salpeter [38] included ion dynamics when attempting to calculate electron density. He showed that the extent to which ion dynamics dominate electron density fluctuations is dependant on the scale length of the perturbation, relative to the Debye length [37]. In doing this, Salpeter introduced the parameter α that is known as the Salpeter parameter:

$$\alpha = \frac{1}{k\lambda_D} \tag{2.2.10}$$

Salpeter showed that when $\alpha > 1$ the electrons behave collectively. In this regime $k\lambda_D < 1$, the motion of each electron is strongly affected by the electrostatic interaction between the other ions and electrons [39]. The probing radiation interacts with the shielded charges which results in collective behaviour. This means that a sum of the electric field contributions from the electrons is collective. Due to these interactions, properties of the ions can be extracted from scattering in this regime. The resulting spectrum is a narrow central peak with a width that is determined by the thermal velocities of the ions. The area under the spectrum is proportional to the electron density [39].

The other regime is when $\alpha < 1$, this is when $k\lambda_D > 1$ and is known as non-collective scattering. Typical α values on MAST are of the order of 10^{-3} [34]. In this regime the probing radiation "sees" the electrons on a scale length in which they appear free [35], meaning they behave non-collectively. The non-collective scattering spectrum reflects the thermal motion of the electrons. Due to this, total power of the emitted field is the vector sum of the field contribution from each individual electron [40]. The spectral shape takes the form of a Maxwellian distribution of the electron velocity due to the frequency shift of the emitted radiation. The frequency shift is simply a Doppler shift that results from the motion of the scattered electrons as the scattering takes place. As $\alpha \to 0$, the spectrum approaches a Gaussian whose half width gives the Doppler shift at the thermal electron velocity [41], which is proportional to the electron temperature. The area under the spectrum is proportional to the electron density, as seen in Figure 2.5.

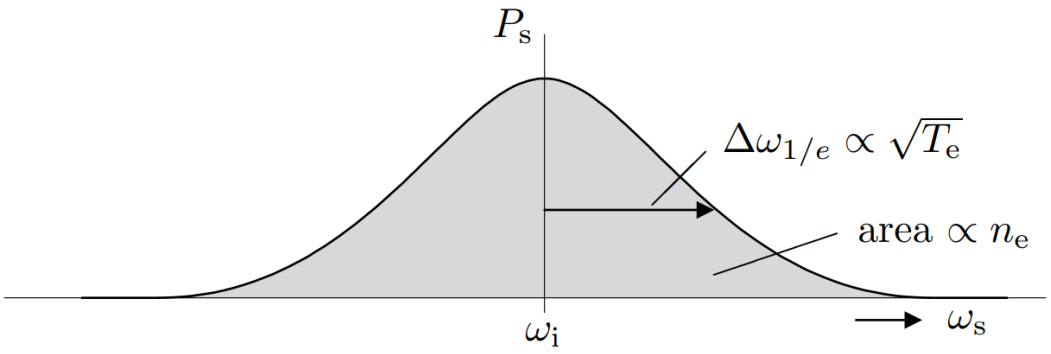

Figure 2.5: A typical non-collective Thomson scattering spectrum from a plasma with a Maxwellian energy distribution, based on the electron velocity. Area and width of the Gaussian are proportional to electron density and temperature respectively. Image taken from [40].

2.3 Thomson Scattering Spectrum

There are a number of different theoretical descriptions of the Thomson scattering spectrum. Pechacek [42] introduced the first relativistic considerations to the Thomson spectrum in 1967. This was modified by Sheffield [43] in 1972 which included a relativistic correction β. The work of Sheffield was expanded upon by Matoba [44] to extend the relativistic correction to β^2 order terms. The first widely used analytical Thomson spectrum was published in 1979 (though developed in 1977) by Zhuravlev [45] before a simplified form was developed by Selden [46] in 1980. This was in a general form that enabled it to be used for fitting routines. A part of this work was including the effect of depolarisation for high temperature (above $\sim 1\,\mathrm{keV}$) effects to a high degree of accuracy. The Selden approximation is still used as the MAST-U theoretical Thomson spectrum, for the core and divertor systems.

Given the low temperature operation of the divertor Thomson system ($T_e << 1\,\mathrm{keV}$), any depolarisation effects are not of concern for the divertor Thomson system or indeed during the scope of this thesis but are presented in [24]. At these electron temperatures the spectrum is approximately centred around the laser wavelength due to negligible depolarisation of the light. In this regime the spectral width scales with the square root of the temperature $\Delta_s \propto \sqrt{T_e}$ [47] assuming a

Maxwellian energy distribution.

An example of the Thomson scattering spectrum used on MAST-U, calculated with the Selden approximation, can be seen in Figure 2.6. In this figure the spectra at a range of relevant electron temperatures is overplotted with the transfer function of one of the divertor Thomson polychromators. It can be seen that there is an overlap with a number the narrower channels close to the laser wavelength which facilitate measurement down to $\sim$1 eV as required in the Super-X divertor.

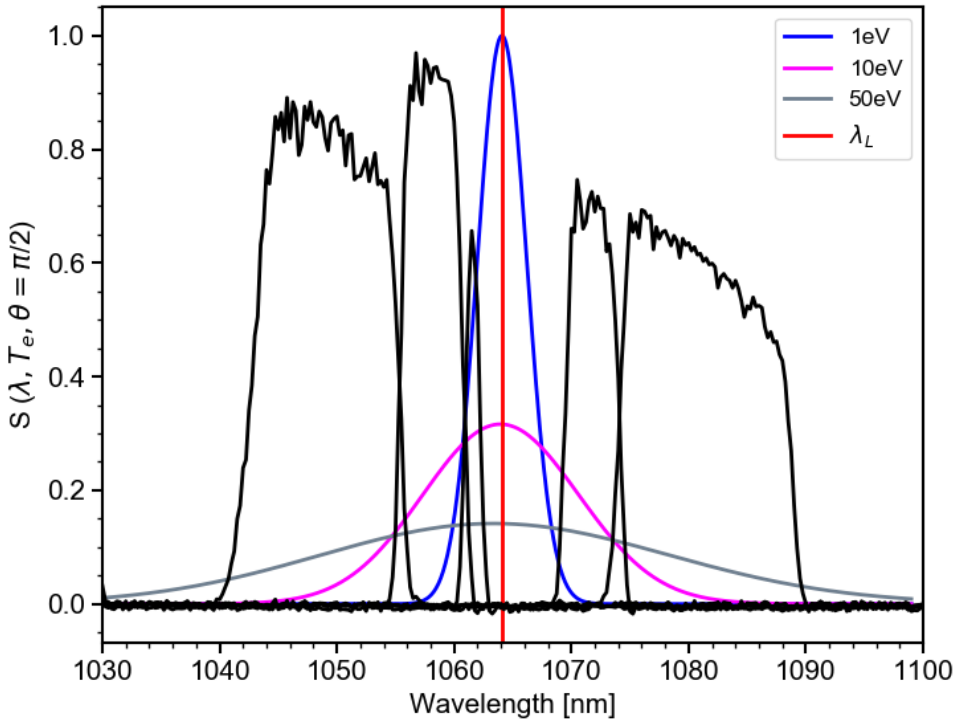

Figure 2.6: Transfer function of polychromator 204 overplotted with the Selden spectra for 1 eV, 10 eV and 50 eV

Chapter 3

MAST-U Divertor Thomson Scattering System

This chapter introduces the MAST-U divertor Thomson scattering diagnostic. Section 3.1 provides an overview of the system within the MAST-U tokamak. Section 3.2 details the design, installation and testing of the optical components that make up the viewing optics of the diagnostic. The electrical setup and modifications made to the previous polychromator design to enable electron temperature measurements down to $\sim$1 eV are presented in Section 3.3.

Plasma background emission as measured by the polychromators is covered in Section 3.4. The radial and spectral variation of the emission measured in the divertor is also detailed in this section. The procedure carried out to generate electron density and temperature values from the scattered signals collected by the diagnostic are outlined in Section 3.5. Work contributing to the optical design, in-vessel optic testing and signal fitting has been published in [16, 17].

3.1 Overview

The divertor Thomson system [16, 17], shown in Figure 3.1, measures electron density and temperature in the divertor during the Super-X phase of a MAST-U plasma pulse. The system features 8 polychromators that can be configured across 12 spatial locations determined by the collection fibres.

The MAST-U Thomson systems are designed for 1064.1 nm Nd:YAG lasers. The divertor system has a dedicated 1 J 90 Hz diode-pumped solid-state laser. For first commissioning of the diagnostic a 1.6 J 30 Hz laser was used with timing synchronised [48] to 7 similar lasers installed in the core Thomson system. The 90 Hz laser was chosen due to the existing 8 30 Hz core system lasers meaning there will be an overlap in the firing frequencies at multiple occasions during a MAST-U plasma, as seen in Figure 3.2.

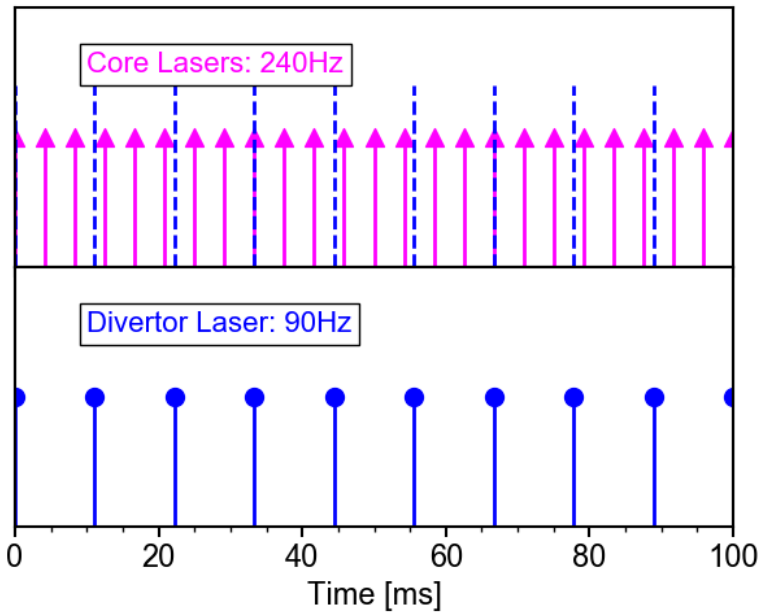

Figure 3.2: Laser timings for the core and divertor Thomson scattering systems

The 12 spatial locations used in the first MAST-U campaign are shown in Table 3.1 with the 8 polychromators designed for the system positioned to prioritise measurements close to the Super-X target (1.14 - 1.44 m in major radius) while providing roughly uniform spacing between the points. A back illumination of the fibres was carried out during calibration work and a comparison between the measured floor positions in-vessel and their projections in the MAST-U CAD can

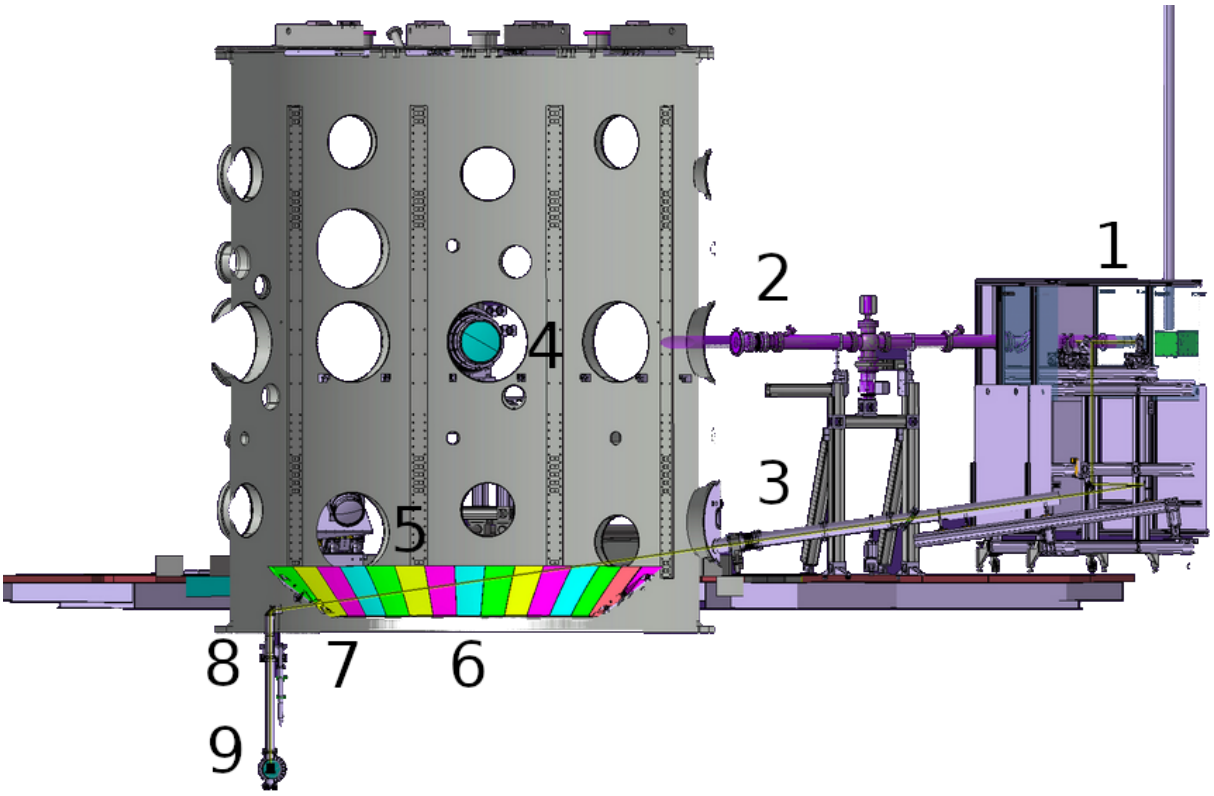

Figure 3.1: Cross section of MAST-U Super-X and divertor Thomson scattering system. (1) Separation of beamlines, (2) core beamline, (3) divertor beamline, (4) core collection cell, (5) divertor collection cell, (6) start of scattering region, (7) end of scattering region at T5 tile hole, (8) in-vacuum mirror, (9) beam dump

be seen in Figure 3.3. This showed good agreement with respect to the edges of the divertor tiles. This showed that the fibres had been installed suitably and were ready to be optimised during final optical alignment. The backplane mapping that resulted in these images can be seen in Table 3.1

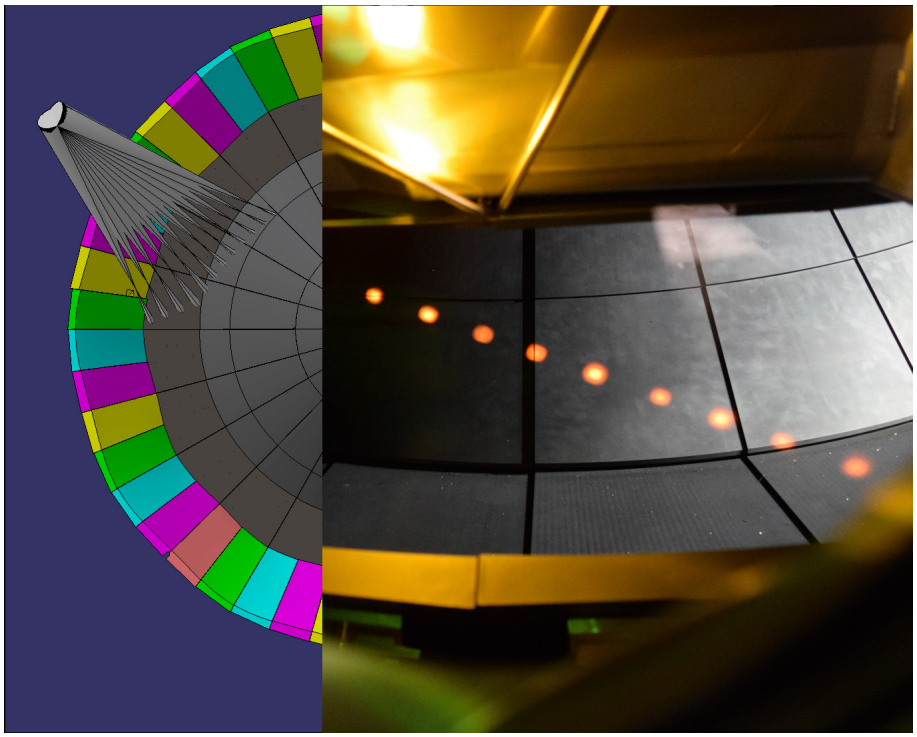

Figure 3.3: A top-down CAD view of MAST-U showing 12 fibre projections for the divertor Thomson system (left) and a view into the lower Super-X chamber from the collection window showing the divertor tiles and 9 of the back illuminated fibre projections visible from this view (right)

Index	Fibre	R (m)	Z (m)	Scattering length (mm)	Scattering angle (°)
1	DTS-10	1.03	-1.84	12.63	113.66
7	DTS-9	1.05	-1.85	12.35	110.51
13	DTS-8	1.08	-1.86	12.11	107.30
19	DTS-7	1.11	-1.87	11.92	104.02
25	DTS-6	1.14	-1.88	11.77	100.70
31	DTS-B2	1.18	-1.89	11.66	97.34
37	DTS-5	1.21	-1.90	11.59	93.96
43	DTS-4	1.26	-1.91	11.56	90.57
49	DTS-B1	1.30	-1.92	11.57	87.17
55	DTS-3	1.35	-1.93	11.63	83.79
61	DTS-2	1.40	-1.94	11.72	80.43
66	DTS-1	1.44	-1.95	11.83	77.65

Table 3.1: Divertor Thomson scattering fibre backplane mapping

While the work surrounding this thesis is centred around the divertor Thomson system, a comparison of some of the basic properties with the core Thomson system can be seen in Table 3.2. The discrepancy in collection optics transmission is a result of the divertor Thomson system not having a wire grid polariser installed. While this was designed to be included, it was not installed during commissioning of the diagnostic due to concerns at the signal level observed in the divertor at unknown electron density values and the low electron temperatures expected.

Quantity	Core System	Divertor System
Laser energy	1.6 J	1 J
F/#	6.0	6.0
Solid angle	0.022	0.022
Collection optics transmission	0.42	0.44
Scattering length	10 mm	12 mm
QE at 1064 nm	0.45	0.45

Table 3.2: Comparison of key parameters for core and divertor Thomson scattering system

3.2 Optical Setup

The core and divertor lasers follow the same ∼20 m beam path down to their respective injection optics where they enter the vessel. Just before entering the vessel the lasers pass through a cubicle which houses a series of optics designed to deliver the respective beams through the window port. The divertor Thomson laser is displaced by 15 mm vertically below the other 7 lasers. This is to separate the chosen laser off into a separate beam path and deliver it into the lower Super-X chamber. This is done with a D-shaped mirror, seen in Figure B.1, which reflects the displaced light in to a separate path to be delivered into the divertor. Due to the absence of this vertical displacement for the other core laser beams they pass over the top of the D-shaped mirror and enter the vessel through the midplane of the device.

With the divertor beam deflected it passes into a series of optics, as seen in Figure 3.4 and Appendix B, that deliver the beam into the lower Super-X chamber. Due to the geometry of the closed Super-X divertor it makes the angle of the laser and the collection optics, as seen in Figure 3.3, complex. In order to ensure the scattered light is orthogonal to the collection cell the laser undergoes a 30° vertical and 8° horizontal polarisation rotation. This is done with a plumb line and a zero degree mirror, seen in Figure B.2 on the right of the horizontal beam, which together form a periscope.

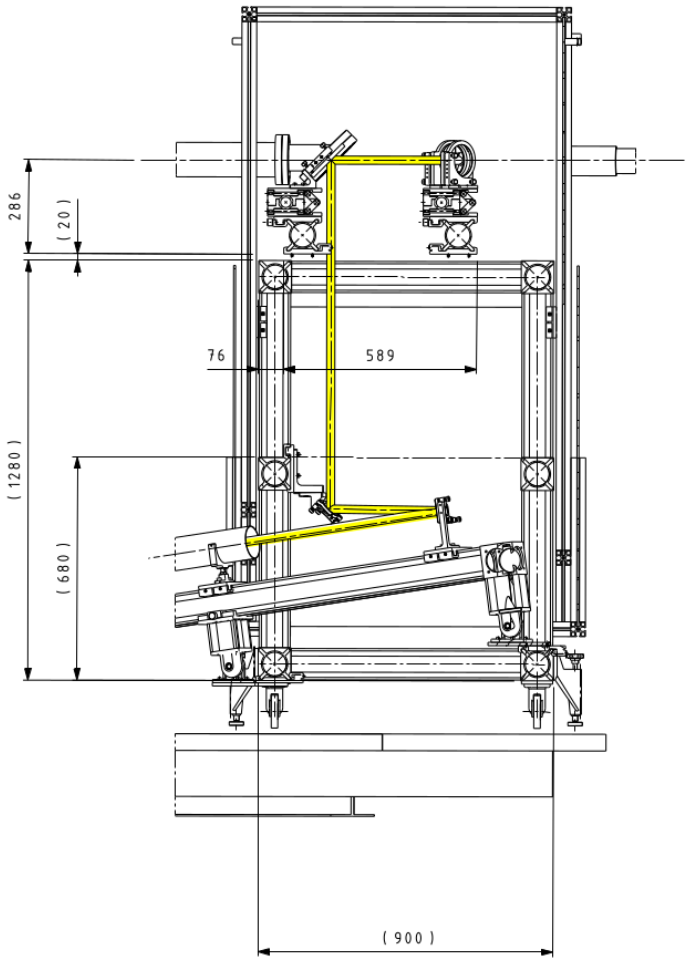

Figure 3.4: Schematic of divertor Thomson optics in the laser cubicle

3.2.1 Focusing Lens

Once the polarisation is rotated the beam is reflected towards the divertor and passes through a 3.41 m focal length lens, seen in Figure B.3. Beyond the focusing lens there is a Brewster window and an aperture before the laser beam enters the vessel. The Brewster window limits stray light by only transmitting light that has undergone the correct polarisation rotation. The lens focuses the beam into the plasma just before the start of the scattering region.

To decide the position of the focusing lens a number of factors were taken into account. Survivability of the in-vacuum mirror, as described in subsection 3.2.2, was the principal concern. Although quoted to a high LIDT ($70\,\mathrm{J/cm^2}$), if damage was done to this mirror it would stop operation of the diagnostic until the next MAST-U vacuum break. This would cause the diagnostic to be out of operation

for a number of physics campaigns where investigation into the Super-X divertor configuration, and as a result operation of the divertor Thomson diagnostic, was crucial. For this reason maximising the beam size at the mirror to reduce the laser fluence and improve the mirror survivability was the priority. Given the unscattered laser light has to pass through a hole in the divertor tile, as shown in Figure 3.1, the 18 mm width of this hole presents a size limit for the beam at this location. As a result there is a compromise between maximising the beam size on the mirror, and not being too close to the edges of the divertor tile hole which would introduce a source of stray light into the system.

Based on the system optics there is 1.5 m of space between the Brewster window and the final mirror which reflects the beam towards the vessel, with the Brewster window itself 4.5 m from the in-vacuum mirror. To determine the optimal position a simulation of the beam was performed. A Gaussian beam profile was used with the assumptions of 1 J of laser energy, 9 mm beam diameter, 23 m of beam path to the lens with 0.5 mrad divergence and M^2 of 3.32. Distances of 0 m, 0.5 m, 1.0 m and 1.5 m between the lens and the Brewster window were tested with plots of the results shown in Appendix C.

The results of these simulations showed that even putting the lens at the furthest possible position from the Brewster window, thus maximising the beam size at the divertor tile, the beam would still fit through the hole. The beam size resulting from this positioning of the focusing length would not be expected to contribute stray light to the system by clipping the divertor tile. This meant that the consideration of the beam size was for the purpose of reducing the fluence on the in-vacuum mirror.

Lens to Brewster distance (m)	**Beam diameter at T5 (mm)**	**Alignment margin at T5 (mm)**	**Beam diameter at mirror (mm)**	**Mirror loading (J/cm^2)**
0	3.93	7.54	6.10	2.42
0.5	6.69	6.15	8.87	1.14
1.0	9.46	4.77	11.64	0.66
1.5	12.23	3.38	14.40	0.43

Table 3.3: Values from Gaussian beam profile simulations of in-vacuum mirror loading from Appendix C

After simulating the beam profile tests were carried out with the focusing lens to profile the beam throughout the focal length. These tests were carried out in a 20 m test path located in the laser lab designed as a space to test optical components. The test path features a similar path length to the actual path to the vessel and one fewer optical surface. This also allows laser burns to be taken at distances of up to 20 m to test the beam quality. As seen in Figure 3.5 a series of laser burns were taken while scanning through the focal length of the lens and showed a good beam profile. Based on the results of the measurements taken in the test path and the simulations the focusing lens was placed 1.4 m from the Brewster window to achieve a mirror loading of $\sim$0.5 J/cm^2 while still maintaining a comfortable gap when the beam passes through the divertor tile.

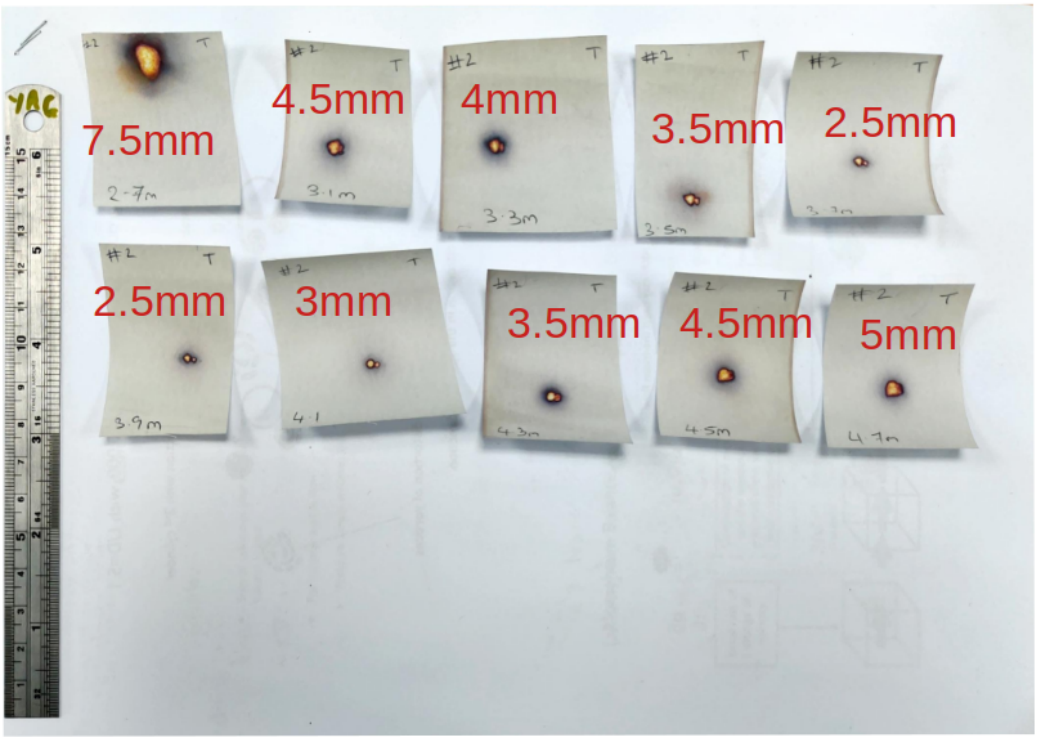

Figure 3.5: Laser burns from tests with divertor Thomson focusing lens

3.2.2 In-vacuum Mirror

Light that is not scattered in the plasma passes straight through towards the divertor tile. To allow the light to exit the divertor there is a small hole in the tile where a high LIDT mirror reflects the beam down into the beam dump located in the pit of the device. This mirror is also used during optical alignment with a HeNe where the beam is adjusted onto a target in the pit of the device on the throughput of the open beam dump, seen in Figure B.4. This allows full alignment of the ∼25 m beam path from the laser room down through the beam dump. To protect the mirror from boronisation and GDC in the divertor there is an automated shutter that is closed when the divertor laser is not firing. As this mirror is in-vacuum it cannot be accessed once the machine goes under vacuum, with the machine being kept under vacuum for extended periods at a time, up to multiple years, due to the nature of tokamak operations.

Based on the simulations of the beam described in subsection 3.2.1 a maximum achievable mirror loading of 2.42 J/cm^2 was expected. With each plasma pulse resulting in 5 s of laser loading for each plasma pulse, the mirror was expected to

be operating comfortably within the limits of the mirror coating. Despite this, it is still advantageous to minimise the loading on the mirror in order to prolong its lifetime and minimise the risk of failure during an experimental campaign. The mirror fluence was expected to be $\sim 0.5\,\mathrm{J/cm^2}$ with the chosen position of the focusing lens. The high LIDT mirror installed is coated to $70\,\mathrm{J/cm^2}$ so it was expected that the mirror should survive at least a few months of daily operation during an experimental campaign without failure. To test the survivability of the mirror, a spare of the mirror installed in the vessel was used in a test path and subjected to the typical laser loading that it would experience during 5 s of a plasma pulse.

For these tests the focusing lens was in place to ensure the size of the beam when it reaches the mirror was as close of a match as possible. The distance of the test path for this was a few metres shorter than the path of the beam to the vessel but this was accounted for by moving the focusing lens to account for this discrepancy. Table 3.4 shows the tests performed with the first set of measurements 5.8 m from the mirror which is close to the lens-mirror distance in vessel and at a slightly higher energy than was used for first operation of the system. The duty cycle was the same 5 s lasing time as that during a plasma pulse but with a 55 s cool down time as opposed to closer to 20 minutes during a plasma operations. This was done to over-stress the mirror. The test parameters (energy, distance to mirror and duty cycle) were increased with the intention of bringing the mirror to failure if needed but this was not achieved, in fact no visible damage resulted. The total exposure time of this is equal to that from 140 MAST-U plasmas. This was more than the diagnostic was likely to operate for during the first campaign. These were also carried out at a higher laser energy and fluence than the system as set up for the first campaign. The survival of the mirror in this setup showed that the high LIDT mirror chosen was suitable for the systems operation.

Cycles	Laser energy (J)	Distance from mirror (m)	Laser diameter (mm)	Laser energy density (J/cm^2)	Duty cycle (s/minute)	Mirror damage (Y/N)
20	1.1	5.8	12	0.38	5	N
20	1.1	5.3	10	0.55	5	N
20	1.3	5.3	9	0.80	5	N
10	1.3	5.3	9	0.80	10	N
10	1.3	5.2	8	1.02	10	N
10	1.3	5.1	7.5	1.16	10	N
10	1.3	4.7	6.5	1.54	10	N

Table 3.4: Results from mirror loading tests with Nd:YAG laser and 3.41 m focusing lens assuming a Gaussian beam profile with a peaking factor of 2

3.2.3 Collection Cell

The collection cell is comprised of seven lenses in close proximity designed to reduce aberrations in the light collected. The final lens focuses the light into 66 positions on the back plane, 12 of which are populated by fibre optics. As a result the scattering length is typically of order $\sim$12mm for a fully populated back plane. A Zemax [49] ray trace of the collection cell and each of its individual elements can be seen in Figure 3.6.

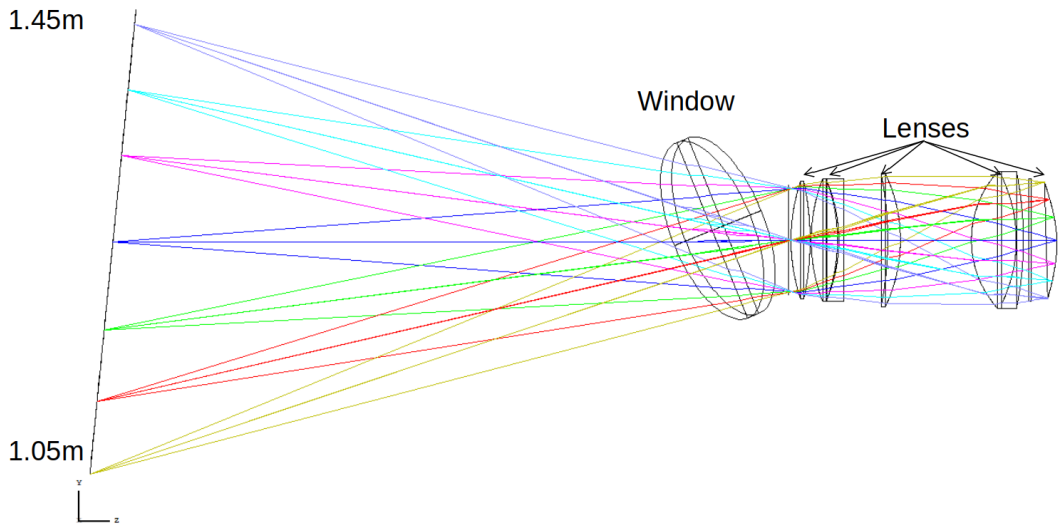

Figure 3.6: Zemax projection of divertor Thomson collection cell

Each lens is anti-reflection coated to maximise transmission in the range of 700-1100 nm while minimising reflections to ∼1% per surface. This results in a theoretical transmission of ∼86% over the spectral range. A broadband calibration of the collection cell can be seen in Figure 3.7, where the transmission is normalised to the 92.3% transmission measured with a handheld 633 nm HeNe laser power meter. This power meter is used during weekly checks to monitor the transmission of the collection cell. By normalising to a known wavelength value it allows the transmission to be monitored over a long period without being able to carry out a spectral calibration of the collection cell while it is in the tokamak area during operations. The spectral calibration showed high transmission across 1040-1090 nm which corresponds to the full electron temperature range of the divertor Thomson system.

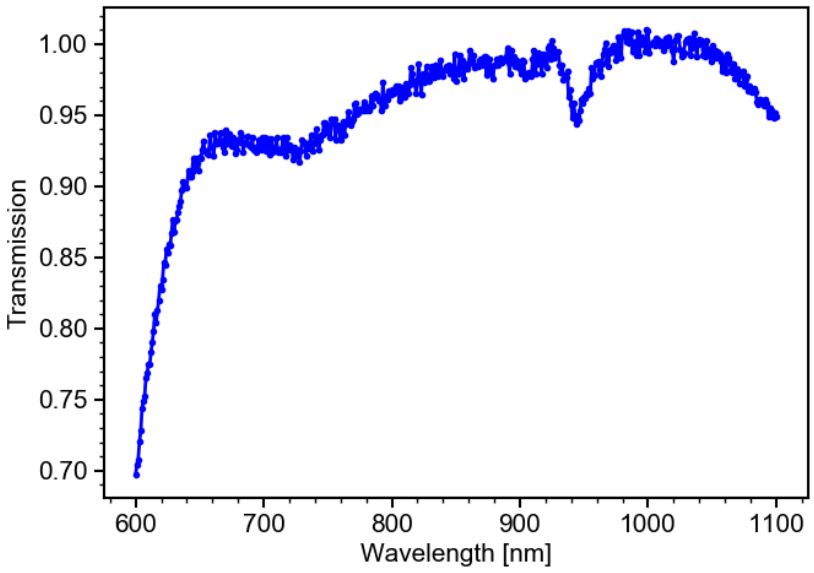

Figure 3.7: Spectral calibration of divertor Thomson collection cell using the setup in Figure 4.1a

Scattered light is collected by a 185 mm clear aperture collection cell between f/6.5 and f/7.1. Light is collected from 1.03-1.44 m along the major radius which corresponds to a range of 113.7-76.7°, as seen in Figure 3.8.

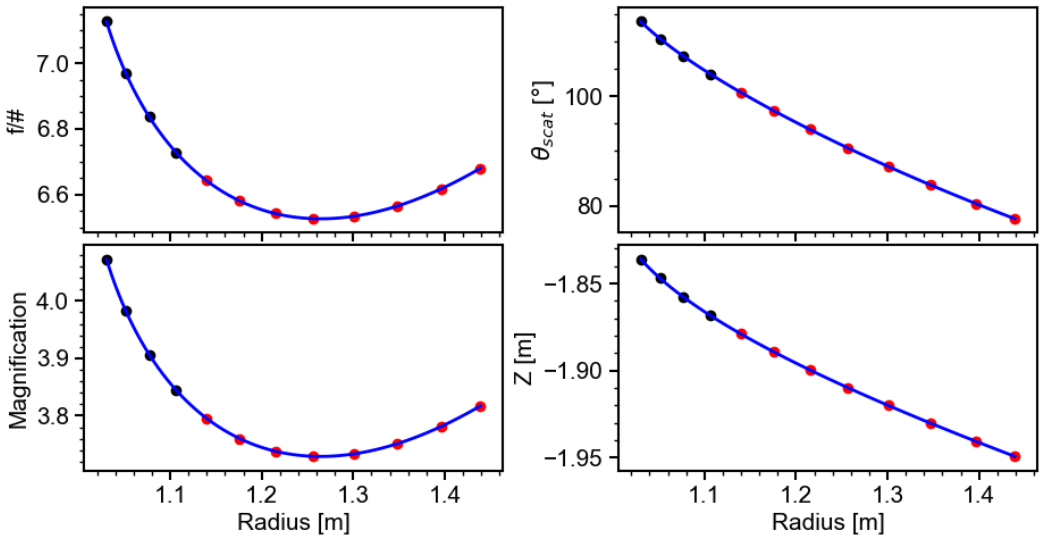

Figure 3.8: Parameters of divertor Thomson scattering collection cell showing spatial points operational during commissioning (red) and spatial points installed but not used during first plasma operation (black). Values taken from Zemax model

The collection cell views the plasma through a 300 mm window on the vessel

that looks down into the lower Super-X at 30° with an 8° horizontal tilt, as seen in Figure 3.9. To protect the window there is an automated shutter that is closed during boronisation and GDC.

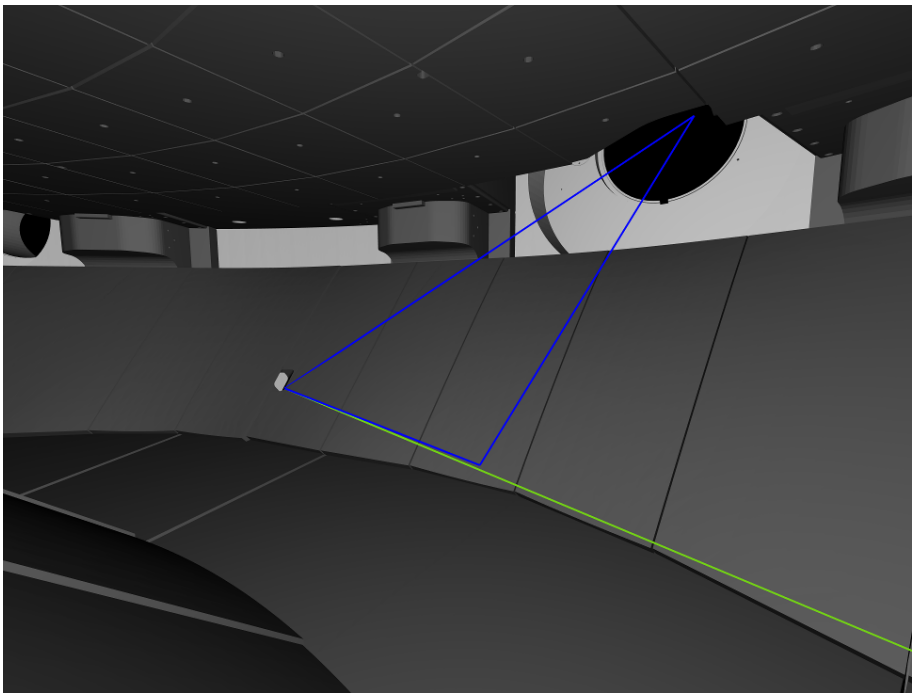

Figure 3.9: Calcam [50] CAD view of Super-X chamber with a representation of the collection cell chord (blue) and the laser line (green) passing through to the hole in the divertor tile

3.2.4 Collection Fibres

The light scattered in the plasma is imaged onto the collection fibres. There are 12 fibres that are equally spaced out across the 66 positions on the collection optic back plane, as seen in Figure 3.10 and Table 3.1. They were chosen to give complete coverage over the viewing chord, prioritising measurements towards the Super-X divertor tile. This resulted in a spatial resolution of $\sim$5 cm for measurements throughout the divertor leg based on the spatial points sampled by a polychromator.

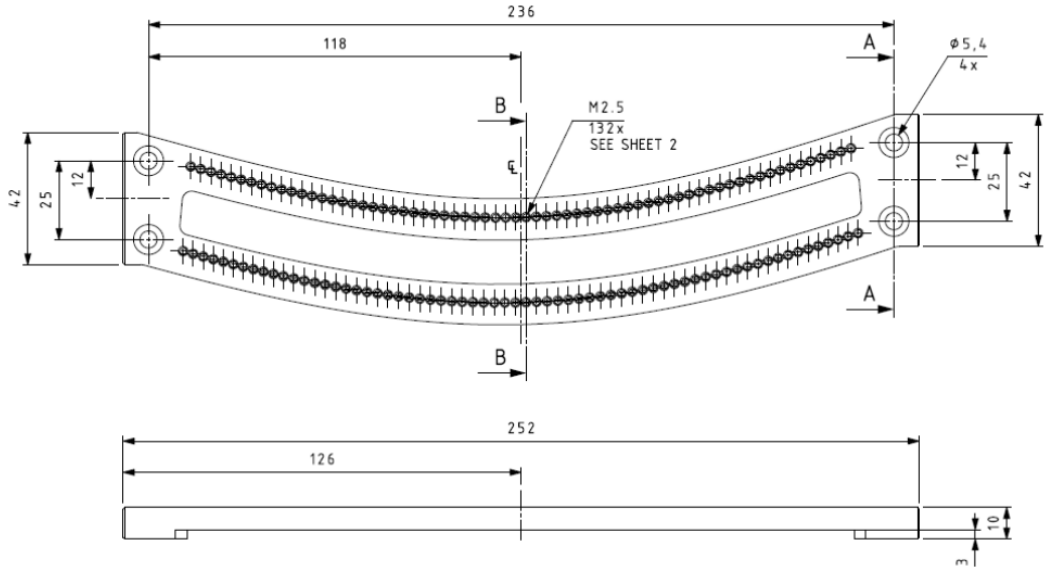

Figure 3.10: A top-down view of the collection cell back plane

The fibres themselves are 130 individual strands that are 13 fibres wide and 10 fibres deep which results in a (3.11×2.02) mm fibre bundle as seen in Figure 3.11a. Of the 12 fibres 2 of these are bifurcated, as shown in Figure 3.11b. These are positioned to aid with optical alignment, as described in subsection 4.2.2.

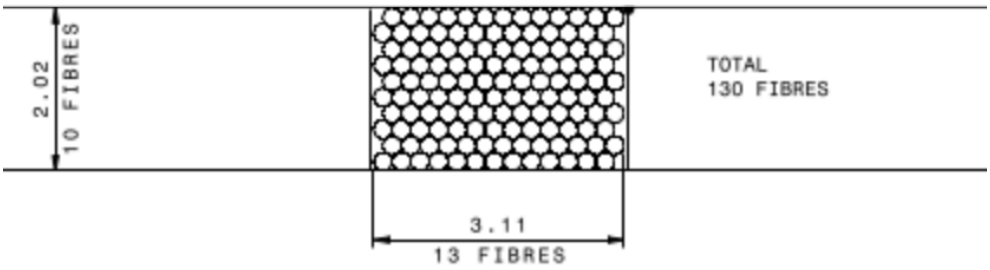

(a) Single fibre

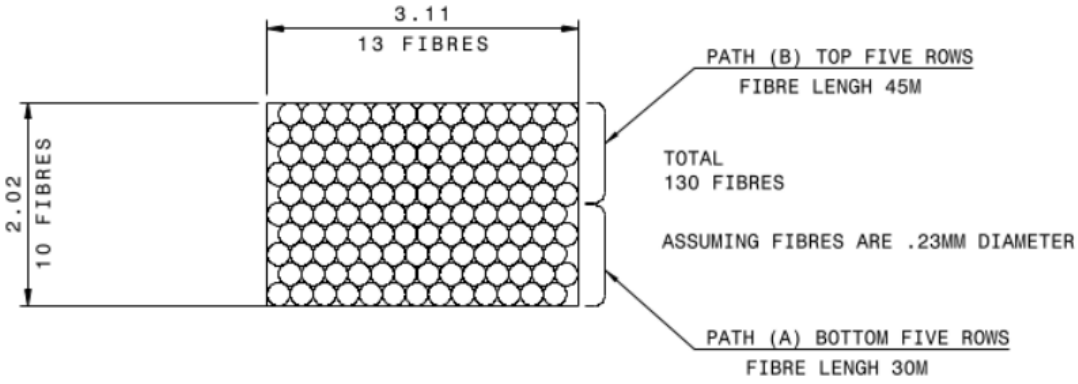

(b) Bifurcated fibre

Figure 3.11: Collection fibres used for divertor Thomson system

The 12 fibres are screwed into their respective position on the back plane as given in Table 3.1. To limit potential damage to the fibres during installation a small 3D printed 'toothpick' matching the fibre width is placed between the screw and the fibre. Given the abundance of space in the back plane for the 12 fibres this provides a lot of flexibility for the measurement locations along the viewing chord, as well as the ability to increase the number of spatial positions in the future.

The fibres are fixed in place to ensure they do not move, given they are not tightly packed. This is important as even the slightest movement would result in a change to the radial location of the measurement as well as the transmission of the fibre. For this reason the fibres are typically only moved immediately before a Raman calibration which allows for alignment checks and calibration of the fibre locations without compromising performance during plasma operations. This

process is described in further detail in Section 4.2.

3.3 Polychromator Design

The MAST-U polychromator has gone through a number of developments throughout its lifetime. With the divertor polychromator optimised for low temperature measurements in high stray light regions. It is an interference filter polychromator, a design originally developed by Carlstrom [51] at DIII-D. An example of the optical layout of the MAST-U polychromator can be seen in Figure 3.12. Each unit for this system consists of 26 bespoke lenses, six mirrors, six interference filters and six printed circuit boards.

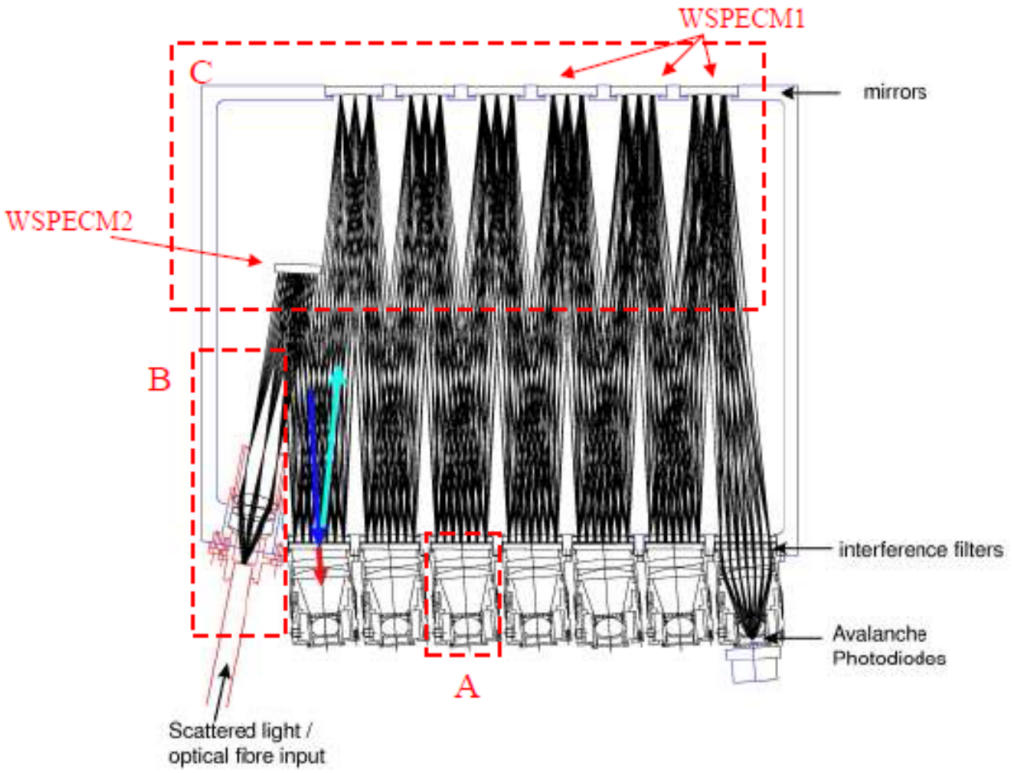

Figure 3.12: The design of a seven channel MAST-U interference polychromator

The previous polychromator design [52] was adapted to meet the requirement of measuring electron temperatures in the 1-40 eV range. Each polychromator measures five different wavelength bands, with a sixth channel installed that is not digitised, and as a result is not visible on any of the polychromator transfer functions. This channel is the first in the cascade where a laser line filter transmissive

to the 1064.1 nm laser light removes stray light that has not undergone a Doppler shift from the initial wavelength. Despite the filter itself not being digitised in the system, it was tested in-situ to determine the transmission, which can be seen in Figure 3.13. With a peak transmission of 95% and FWHM of 2.3 nm the filter is operating very close to its theoretical performance. Due to the 4.5° angle of incidence from the normal plane the laser wavelength is not centred about the filter but despite this, the laser wavelength still falls comfortably within the pass band and sees good transmission.

The light transmitted by each of the subsequent filters passes through a short focal length lens which focuses the light onto a detector. The detectors used for this system are discussed in further detail in subsection 3.3.1. The filters used for this system can be seen in Table 3.5.

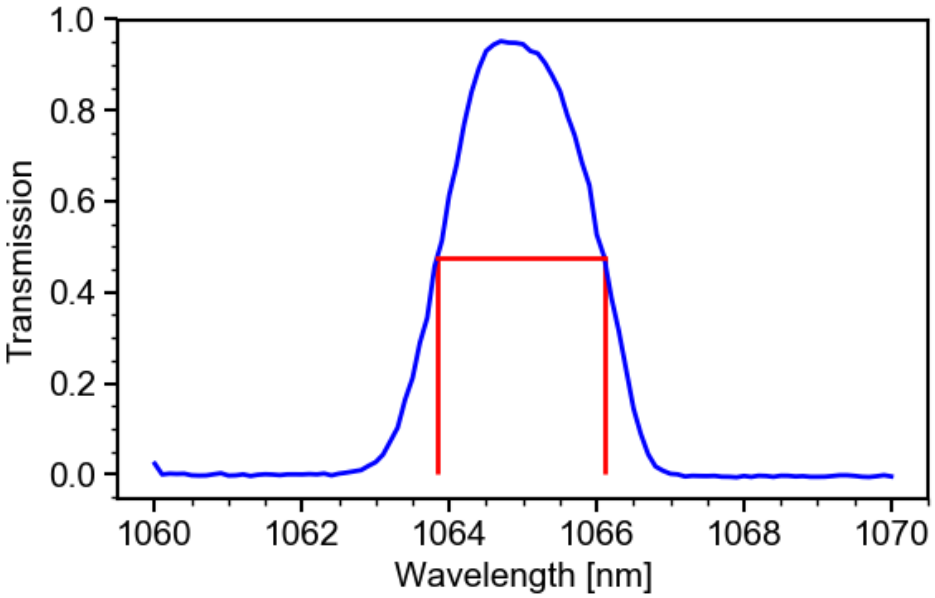

Figure 3.13: Transmission of 1064.1 nm laser line filter tested in-situ

Central Wavelength (nm)	**Bandwidth (nm)**	**AOI (°)**	**Transmission (%)**	**OD**[a]	**Digitised**
1064.1	N/A	4.5	>99	6	No
1081	15	4.5	>99	6	Yes
1071	5	4.5	>99	6	Yes
1057	5	4.5	>99	6	Yes
1047	15	4.5	>99	6	Yes
1061	2	0.0	>99	6	Yes

[a] OD = -log $\left(\frac{N_T}{N_I}\right)$ at 1064.1 nm

Table 3.5: Interference filters used in Divertor Thomson scattering polychromators manufactured by Alluxa

The core system has a measurement limit of ∼5 eV [53] due to its filter configuration. To enable measurements below this, a new 1061 nm channel with a 2 nm bandwidth was added. The Alluxa optical filters used in these polychromators have OD6 light rejection in addition to the 1064.1 nm laser line filter to reduce stray light transmission. The number of filters close to the laser wavelength, in comparison to the core Thomson system, can be seen in Figure 3.14. This facilitates the low temperature measurement required by this system for operation in the Super-X divertor.

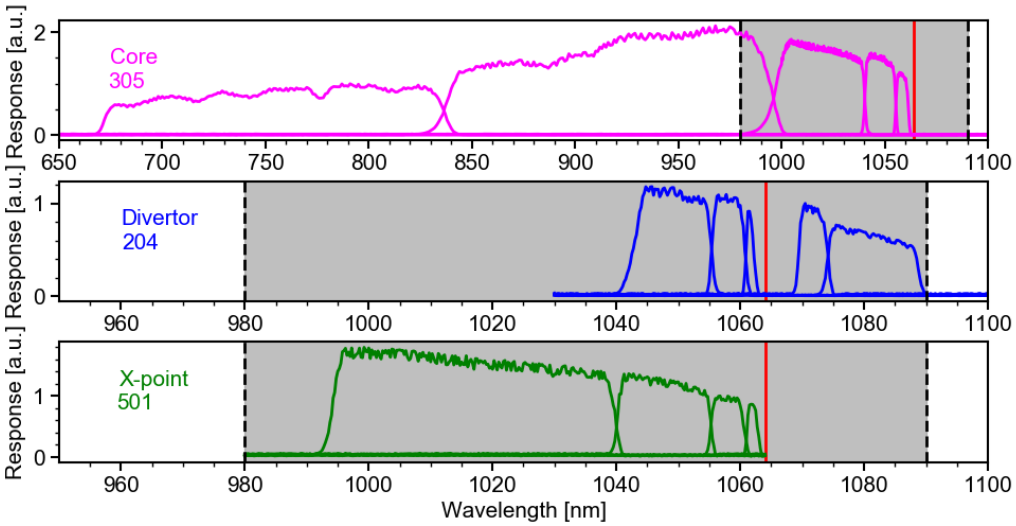

Figure 3.14: Transfer functions of core (pink), divertor (blue) and X-point (green) Thomson scattering systems

Interference filters are designed for incident light normal to the filter but they can be angled to change the central wavelength of the band pass. In this application this is crucial as it provides the opportunity to de-tilt the 4.5° angle of incidence θ. This shifts the central wavelength of the chosen filter back to its intended central wavelength, closer to that of the laser. The result is the ability to detect lower electron temperatures with measurement closer to the laser wavelength. The relationship for the tilt angle is given by: $\lambda = \lambda_0 \left(1 - \frac{\sin^2\theta}{n^2}\right)^{1/2}$ [51, 54].

As a result the last filter in the cascade for the divertor and X-point Thomson systems, the 1061/2 nm filter, is placed at a normal to the plane of incidence rather than the 4.5° for the rest of the cascade. This 4.5° tilt shifts the transmission function ∼1 nm closer to the laser wavelength which aids low temperature (sub-eV) measurements and reduces the overlap with the filter next to it. This is achieved by adding a 4.5° 3D printed tilt stage placed under the filter to adjust the angle the filter makes to the incident light, as seen in Figure 3.15. After the final interference filter the beam is reflected onto a beam dump.

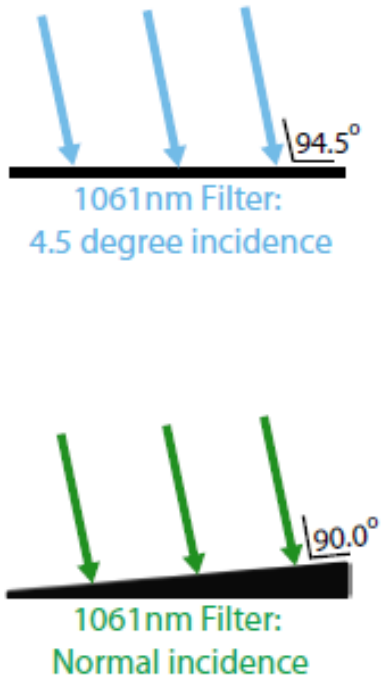

Figure 3.15: 1061/2nm filter angle with and without the de-tilting wedge

It was observed that de-tilting the filter made a negligible difference in the transmission of the filter. This was investigated in previous work done by Hawke [55] and its effect can be seen in Figure 3.16. The downside to doing this is that by moving the filter closer to the laser wavelength it increases the chance of stray light being transmitted by the filter. Given the stray light mitigation techniques featured in these polychromators, particularly the OD6 blocking and the transmissive filter this was not a concern.

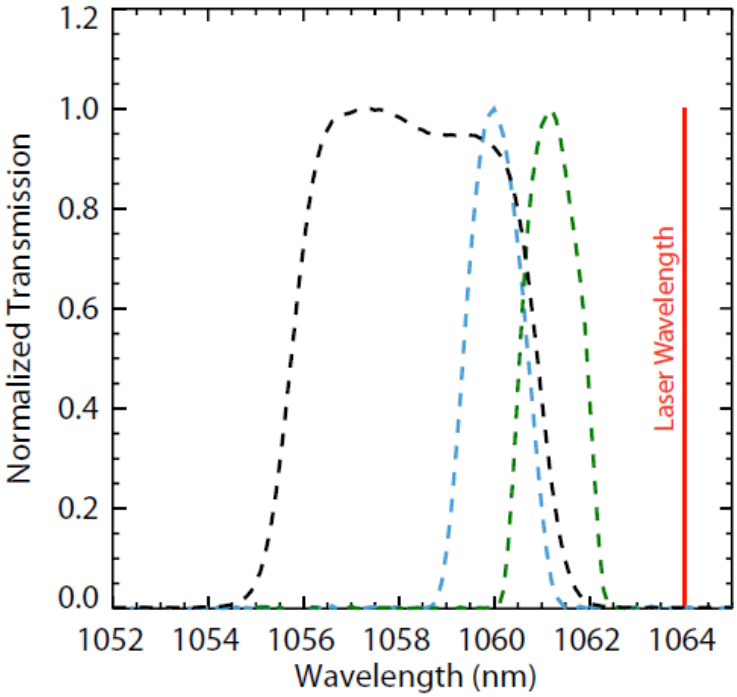

Figure 3.16: 1061/2 filter transfer function shift with the 4.5° incidence (blue) and normal incidence (green) taken from [55]

The impact of this stray light mitigation can be seen in Figure 3.17 where a divertor Thomson polychromator was installed into the core Thomson system for a MAST-U commissioning plasma. The reference shot 43738 was a magnetic calibration shot where no plasma was formed but the lasers still fired. This was taken earlier in the day without moving the laser alignment between the two shots. This showed clear stray light in the core Thomson polychromator (right) due to laser interaction with the centre column. In contrast the divertor Thomson polychromator during 43747 (left) showed no stray light in any of the channels, even the low temperature channels closer to the laser wavelength. The signal resulting from the plasma can clearly be seen in each of the channels apart from the 1017/45 nm channel. This is because there are not enough scattered photons collected at wavelengths that are passed by this filter due to the low electron temperature at the edge of plasma. This mitigation of stray light is a significant improvement on the design implemented for the core polychromators and it is a key component of the system that enables measurement down to low electron temperatures in the divertor.

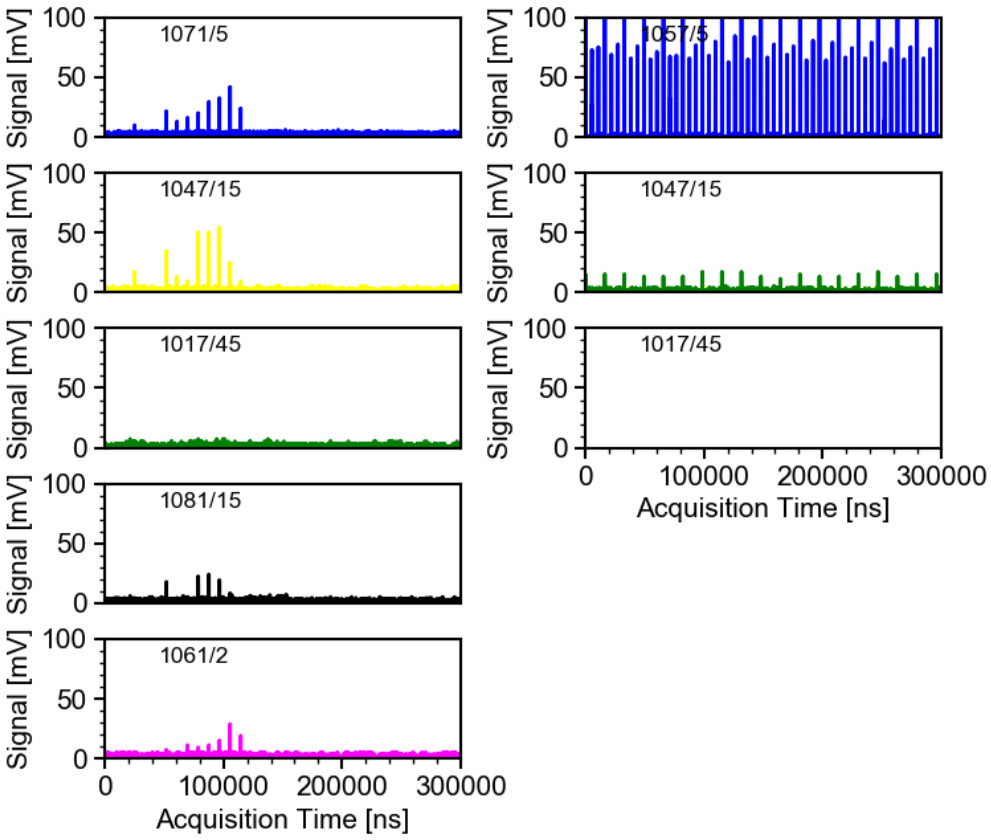

Figure 3.17: Comparison of divertor Thomson polychromator (left) data from MAST-U plasma 43747 installed in place of a core Thomson polychromator (right) for 43738 demonstrating a reduction in stray laser light in the digitised channels

It can be seen in Figure 3.18 that each filter has a well defined pass band with low ripple in its transmission. The filter configurations are designed to provide a small overlap between adjacent filters. This is to ensure that even at the temperature limits of the system signal is received in at least two spectral channels, which is needed to resolve electron temperature and density measurements. This procedure is described in further detail in Section 3.5.

Despite the requirement of having good signal level in at least two spectral channels for a Thomson measurement, a channel overlap too large can limit the signal observed in a channel. This is particularly a concern for the narrower channels closer to the laser wavelength. For this reason a well designed spectral calibration is imperative, with each of the individual filters having good transmission and a well defined pass band. The spectral calibration process is described in Section 4.1.

The divertor polychromators feature two pairs of complimentary filters which

are symmetrical about the laser wavelength, as seen in Table 3.5, with a filter on the red and blue shifted side of the wavelength spectrum. These are designed to provide contingency in high stray light regions. An example of this would be atomic line emission in the plasma which causes stray light to be present or even saturate a spectral channel. In the case that stray light does not impact the measurement, the filters simply contribute additional signal. It is expected that there will be a quantum efficiency (QE) drop off at these wavelengths compared to their filter compliments on the blue shifted side of the wavelength spectrum. It is not expected that this will make a significant effect and the Thomson spectrum is symmetrical about the laser wavelength, as seen in Figure 2.6, so there is not expected to be much impact on the Thomson signal collected despite the wavelength space being on the red shifted side of laser wavelength. Any effects from a difference in quantum efficiency will be accounted for in the spectral calibration of the polychromator, as described in Section 4.1.

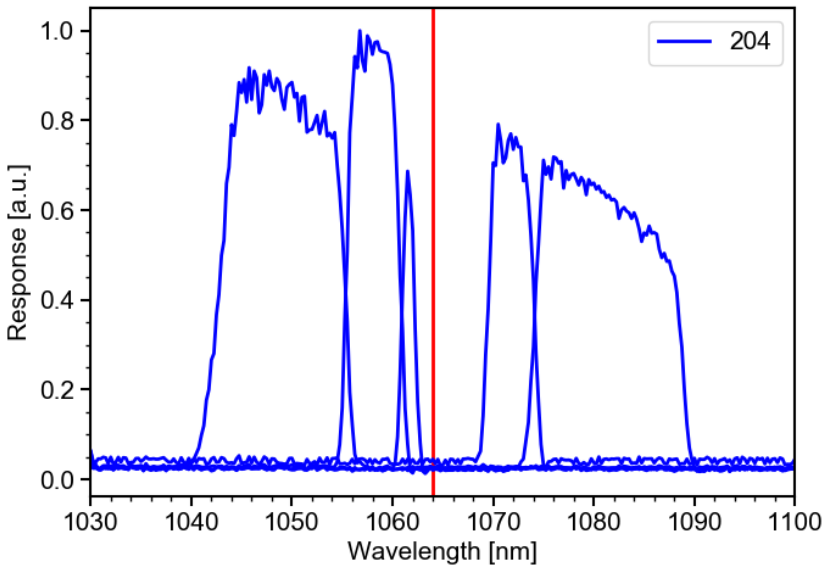

Figure 3.18: Transfer function of polychromator 204 normalised to the peak response of the 1057/5 nm filter

For the first MAST-U campaign the X-point Thomson polychromators, as seen in Figure 3.14, were used in the divertor Thomson system in place of the intended polychromators. This was done due to the 1061/2 nm filter installed in the divertor initially not having the de-tilt stage, seen in Figure 3.15, installed to have the

angle of incidence at a normal. This was done due to concerns of the level of stray light that would be seen in this narrow spectral channel. As the de-tilt results in the central wavelength of the filter being $\sim$1 nm closer to the laser wavelength the stray light blocking performance will see a reduction. When first using these polychromators the stray light was discovered not to be as much of a concern as expected, but due to the low electron temperatures observed in the Super-X the sub-eV measurement of these polychromators was under performing. A change to the X-point polychromators for a number of Super-X plasmas provided an improvement in sub-eV performance of these polychromators due to the central wavelength adjustment of the 1061/2 nm filter. The effect of this filter adjustment can be seen in Figure 3.19 where simulations were performed using photon accounting methods based on the filter central wavelength and bandwidth and the estimated QE based on the the values given in [56]. These simulations assumed 90° scattering angle, $1 \times 10^{19}\,\mathrm{m}^{-3}$ electron density and 1 J of laser energy and showed a clear improvement in the fractional error measured by the polychromator below 10 eV. As a result of the plasma measurements during commissioning of the system and these simulations a tilt stage was added to the corresponding filter in the divertor polychromators after the conclusion of the first MAST-U physics campaign.

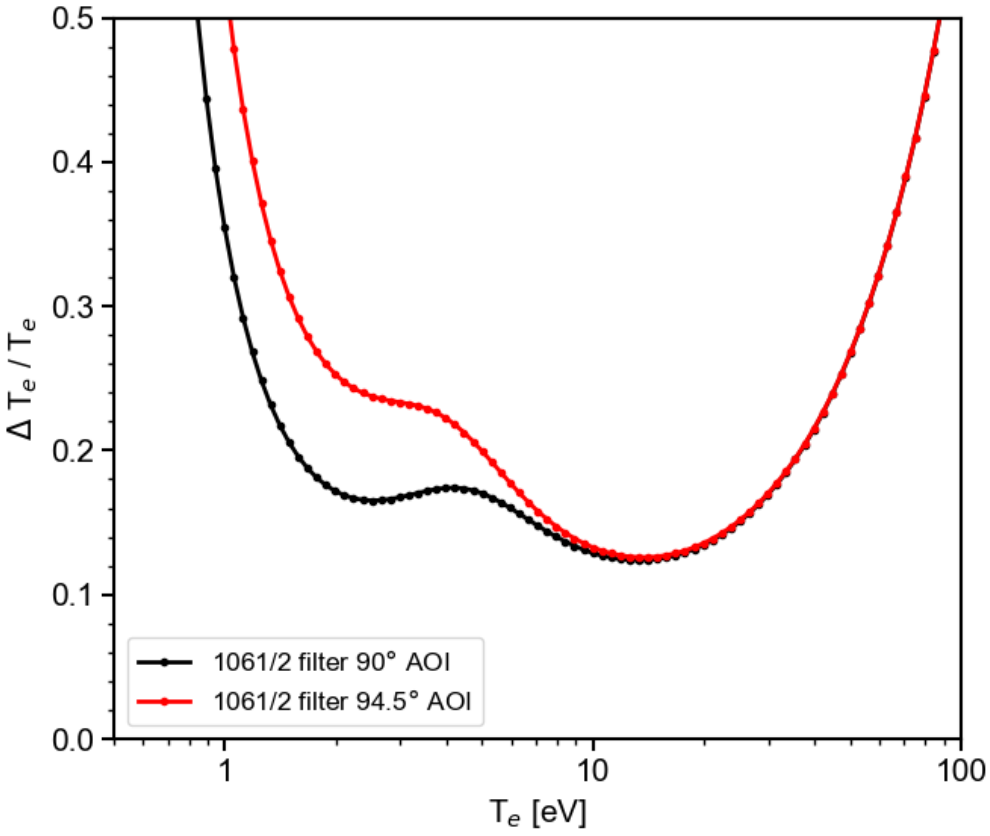

Figure 3.19: Simulated fractional error for a divertor Thomson polychromator with (black) and without (red) the AOI adjustment for the 1061/2 nm filter. Simulation assumed 90° scattering angle, 1×10^{19} m^{-3} electron density and 1 J of laser energy

With the inclusion of complementary filters on the red shifted side of the wavelength spectrum in the divertor polychromators, simulations were carried out to see what the impact of including a 1067/2 nm filter would have on the fractional error of this polychromator confiuration. This wavelength was chosen due to its symmetry about the laser wavelength with the 1061/2 nm filter. This was of interest to see the impact this filter would have on measurements below 5 eV, in the case of lower than expected electron temperatures in the Super-X divertor. Given the bandwidth of this filter it would be expected to reduce the fractional error of electron temperature measurements below 5 eV and make a negligible difference to the fractional error of electron temperatures exceeding 10 eV. The result of this simulation can be seen in Figure 3.20. The addition of this filter was shown to reduce the simulated fractional error for the electron temperature measured. It

would contribute a 2.5% reduction in fractional error at 5 eV and a 7.5% reduction at 0.5 eV while still seeing a slight improvement at 10 eV with a 0.6% reduction in the fractional error. This simulation has shown that inclusion of this filter would be a potential upgrade to the divertor polychromator and in the event that electron temperatures measured in the Super-X divertor are lower than expected, it offers a potential solution to the current limits of this polychromator specification.

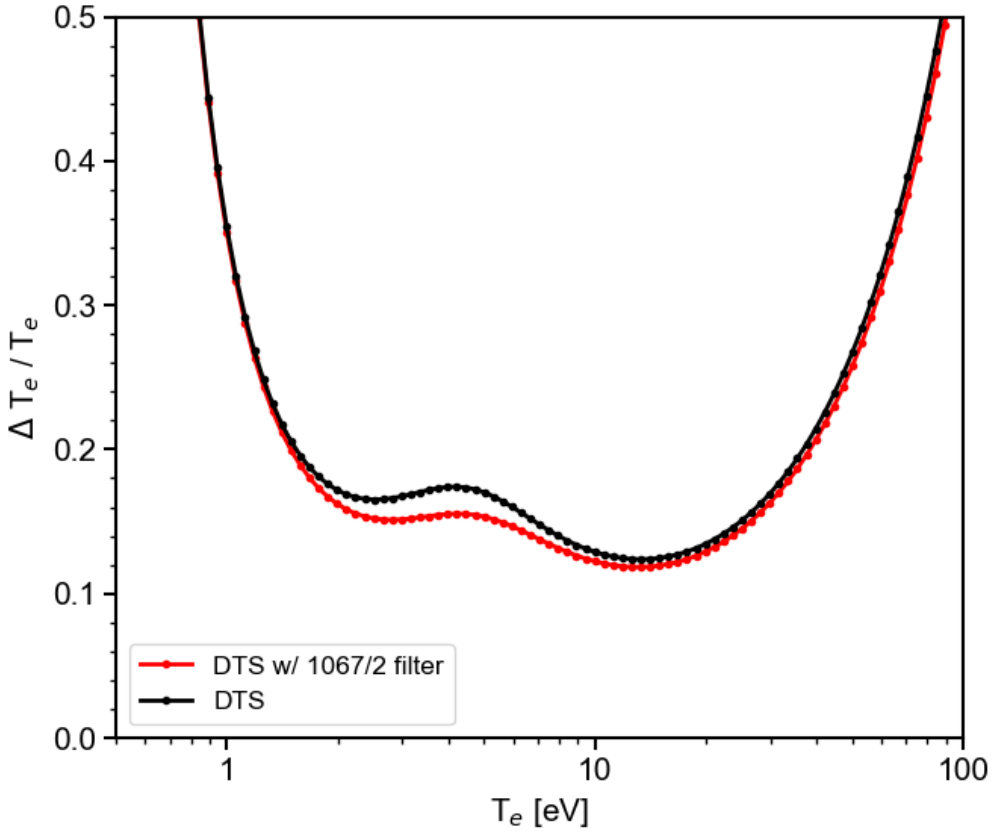

Figure 3.20: Simulated fractional error for a divertor Thomson polychromator with (red) and without (black) a 1067/2 nm filter. Simulation assumed 90° scattering angle, 1×10^{19} m^{-3} electron density and 1 J of laser energy

3.3.1 Electrical Setup

Each pass band transmitted by an interference filter is measured by a photodetector. The photodetectors used are Avalanche Photodiodes (APDs). APDs are high speed semiconductor light sensors that are used due to their high quantum efficiency (QE) and gain meaning that low intensity light can be detected. Materials

such as Silicon (Si) and Indium Gallium Arsenide (InGaAs) are commonly used materials. They are selected for a specific purpose based on their gain and photosensitivity. Silicon is sensitive up to wavelengths of 1100 nm due to its bandgap of 1.11eV [57] which makes it the choice for this Thomson systen operating up to 1090 nm.

The gain of the APD is an increasing function of the reverse bias and a decreasing function of the temperature. At 25° C the gain is set to 250 kV/W in a reverse bias voltage set by the manufacturer. The APDs have a temperature sensitive diode as part of a thermal compensation circuit that is used to control the reverse bias, which in turn controls the gain [52]. To further control the temperature variation of the polychromators, the units are kept in an air conditioned room.

The polychromators feature bespoke printed circuit boards (PCBs), as seen in Figure 3.21, that filter and amplify the detected signal. The signals from the APDs are electronically filtered by operational amplifiers with a high pass (fast) channel and a low pass (slow) channel. The fast channel measures the scattered signals with a duration of ≈ 25ns. Signals below ≈ 200kHz are removed as these are due to background plasma events. Despite this, the high pass filter has no effect on the scattered light. The slow channel measures the background light from the plasma and passes signals below 200kHz.

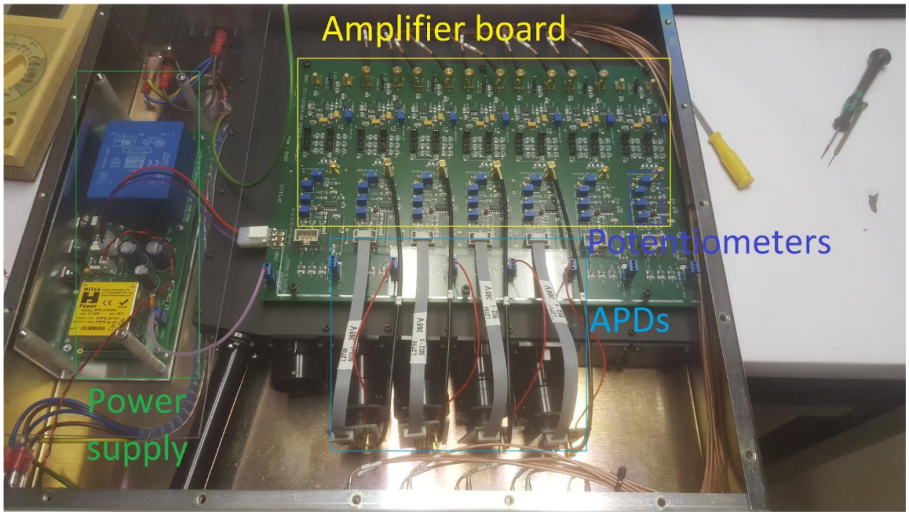

Figure 3.21: Complete electrical assembly of a MAST-U Thomson scattering polychromator

The polychromators themselves are stored in a cubicle. Each module contains eight polychromators and a compact PCI chassis containing eight anologue-to-digital converter (ADC) cards. Each card provides 1G S/s ADC channels with 40 in place to digitise the 5 fast channels of the 8 polychromators. Due to the high rate of sampling, 300 ns is recorded for each of the channels which is transferred to memory after a laser pulse. A separate module houses additional hardware for laser power measurements and the triggering system [48] which is common among the other Thomson systems.

3.4 Background Plasma Measurements

The scattered signals in Figure 3.22 represent the total incident light transmitted by a single polychromator located at the divertor tile. This is the background plasma light connected to the slow digitisers recorded at 100 kS/s. For these channels the background noise level is subtracted to account for any effects from the digitisation level or individually set gain. Given there is negligible signal in each of the channels until after 400 ms when the plasma transitions into Super-X it is a safe assumption that the light entering the plasma is from divertor plasma rather than any light from the core plasma reflected into the Super-X chamber and collected by the polychromator. There is a ∼50 ms delay in the signal reaching this polychromator after transitioning from the conventional which can be accounted by the delay in the strike point reaching the position on the Super-X divertor tile where this polychromator views.

Given a plasma emits a broadband spectrum of light, the magnitude of signal in each channel would be expected to be proportional to the bandwidth of the channels in Figure 3.22 (15:5:2:15) but this is not the case. Even accounting for the loss in QE from the silicon APD at the longer wavelengths such as the 1081/15 nm filter, the magnitude is still comparable to that seen in the 1047/15 nm filter. This filter also sees less signal than the other two channels, despite also having the largest bandwidth. This suggests that there are strong sources of line emission, from sources such as plasma recombination, that are causing significant signal to be seen in certain spectral channels. This is independent of even a narrow bandwidth

channel as seen in the 1061/2 nm channel. This shows that rejection of light from outside the pass band of the filters is imperative and the signal filtering described in subsection 3.3.1 is crucial for facilitating Thomson scattering measurements, particularly in areas of high plasma emission such as the divertor.

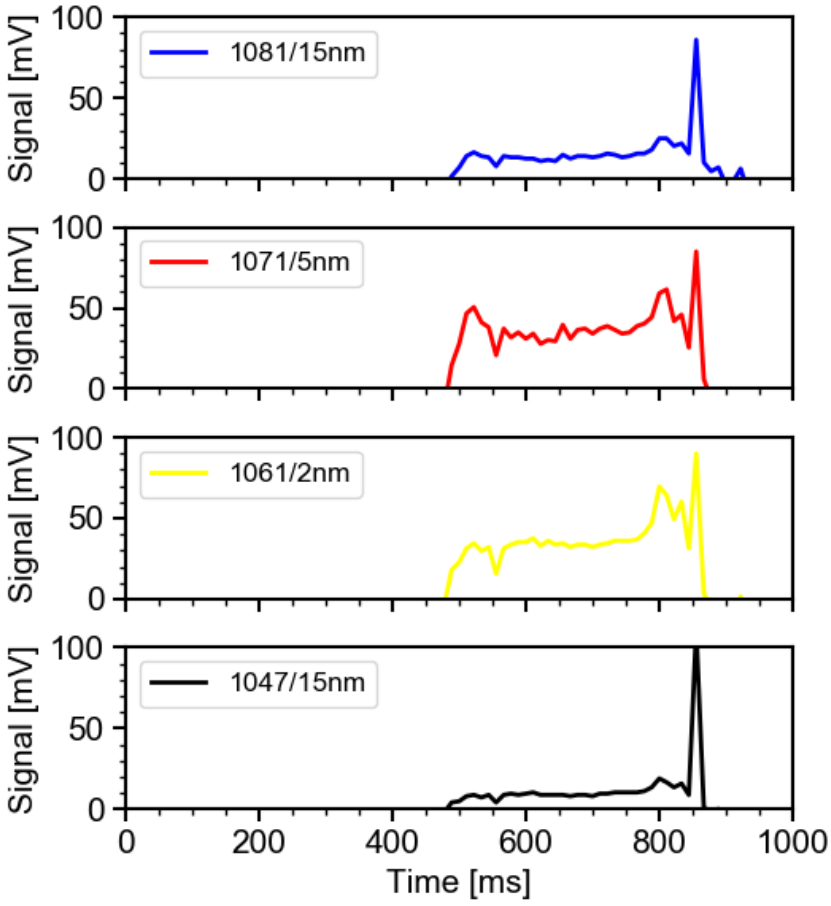

Figure 3.22: Background plasma emission from slow digitisers at the divertor target for 44158

Taking the 1047/15 nm channel which is a channel common across the polychromators, the radial variation across the viewing chord can be seen in Figure 3.23. Each of the four channels show different behaviour corresponding to each of the radial positions. As the plasma transitions to Super-X divertor configuration at 400 ms the rise in signal above the noise level can be seen to occur at different times, with this delay corresponding to the radial position. This can be accounted for by plasma reaching each of the radial positions at a later time as the divertor strike leg is swept out from nearer the throat (1.18 m) to close to the Super-X

tile (1.44 m). Each of the spatial positions has a different profile of the measured plasma emission over time, despite measuring the same portion of the wavelength spectrum. This indicates a real difference in the plasma properties amongst the radial locations sampled. Generally the radiation being measured is dependent on the local temperature of the plasma. Given the magnetic field effects on plasma, particularly in the divertor, with increasing radius it is expected that the plasma at smaller radii will generally possesses less energy, specifically lower electron temperatures. Based on the magnitude of the emission and its reduction with increasing radius, this would correspond to a reduced emission in the wavelength band which is a result of decreasing electron temperature.

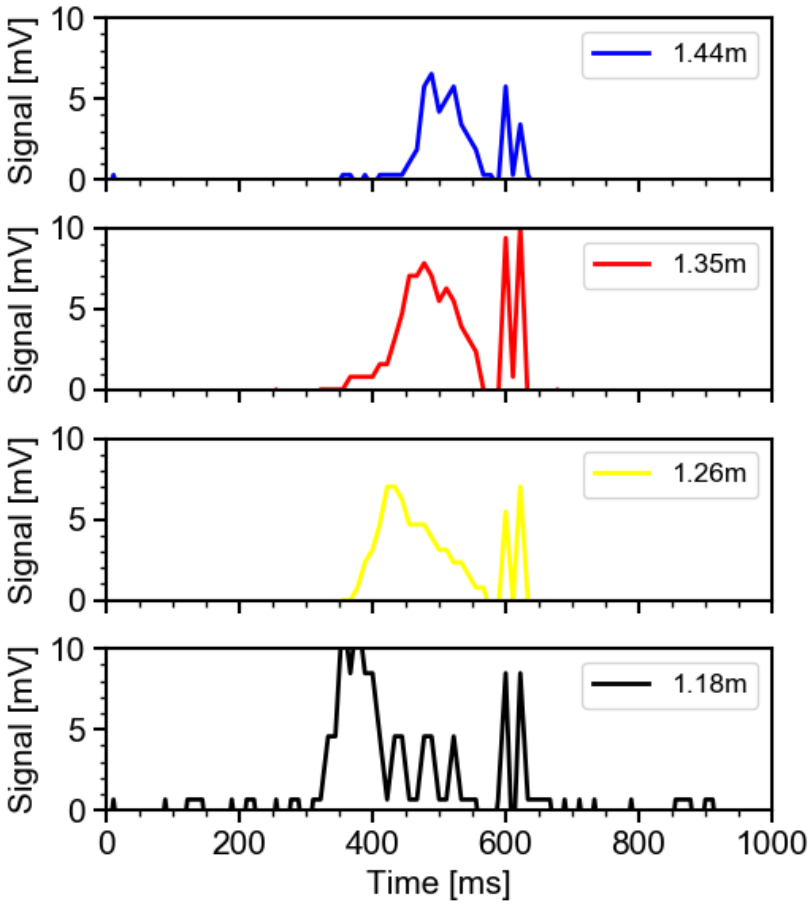

Figure 3.23: Background plasma emission for 1047/15 nm channel of a number of divertor Thomson spatial points for 44154

3.5 Signal Fitting

The scattered power P_s as a function of the scattered wavelength λ_s due to Thomson scattering is given by:

$$P_s(\lambda_s) = P_i n_e L \Delta\Omega \frac{d^2\sigma(\lambda_s, \theta, T_e)}{d\lambda_s d\Omega} \tag{3.5.1}$$

where P_i is the incident laser power, n_e is the electron density, L is the scattering length and $\Delta\Omega$ is the solid angle.

The cross section for scattered power per unit wavelength per unit solid angle is given by:

$$\frac{d^2\sigma}{d\lambda_s d\Omega} = \frac{\sigma_0}{\lambda_i} S(x, \theta) \tag{3.5.2}$$

where σ_0 is the Thomson scattering cross section, λ_i is the incident wavelength and S is the Selden equation [46].

The number of scattered photons n_s as function of wavelength is given by:

$$n_s(\lambda_s) \left(\frac{hc}{\lambda_s}\right) = n_i \left(\frac{hc}{\lambda_i}\right) n_e L \Delta\Omega \frac{d^2\sigma(\lambda_s, \theta, T_e)}{d\lambda_s d\Omega} \tag{3.5.3}$$

where n_i is the number of incident photons.

The number of photons detected $n_{detected}$ in a channel is given by:

$$n_{detected} = n_i n_e L \Delta\Omega \frac{QE}{F} \int \frac{\lambda_s}{\lambda_i} \frac{d^2\sigma(\lambda_s, \theta, T_e)}{d\lambda_s d\Omega} \phi(\lambda) d\lambda \tag{3.5.4}$$

where QE is the quantum efficiency of the detector and F is the noise factor.

In order to relate the scattered signal measured to the electron density the polychromators have to be absolutely calibrated. There are typically two methods of absolute calibration used for Thomson scattering diagnostics, Rayleigh scattering and Raman scattering, which are discussed in Section 4.2.

Based on typical numbers for the MAST-U divertor Thomson system (1 J laser energy, 15% estimated quantum efficiency (EQE), 12 mm scattering length, 44% optical transmission and 95% filter transmission) and system specifications taken from Table 3.2 the number of photoelectrons expected to be detected by the system can be calculated using Equation 3.5.4. This is using the Thomson scattering cross section and assumes no vignetting of the optics. Based on these

numbers the system would be expected to detect 3506 photoelectrons per 1×10^{19} electrons in the plasma, assuming half of the Thomson spectrum is collected. If these same values are used with the Raman scattering cross section in place of the Thomson scattering cross section the number of photoelectrons detected for a certain pressure of Nitrogen can be evaluated. For 50 mbar of Nitrogen, which is equivalent to 1.21×10^{24} molecules, 3796 photoelectrons would be detected. This is assuming that half of the Raman spectrum is collected, which would be equivalent to collecting the anti-Stokes portion of the spectrum. As a result of this comparison, the Thomson scattering signal measured from 1×10^{19} electrons would be expected from 1.16×10^{24} molecules of Nitrogen.

The laser energy for the first MAST-U campaign was reduced to 0.8 J by altering the Q-switch delay and broadening the laser pulse. This was done as a precaution to preserve the in-vacuum mirror [16] by reducing the laser fluence. The duration of the laser pulse at this energy is ∼25 ns full width at half maximum (FWHM). Scattered signals are fitted on embedded computers as part of the data acquisition to generate a Gaussian fit. Mean 1-sigma values are typically on the order of 12 ns which corresponds to a FWHM of 28 ns.

An example of fitted signals for a ∼1 eV plasma can be seen in Figure 3.24. Signal is observed in the 1057/5 nm and 1061/2 nm channels. This is due to the temperature of the plasma at this location. The 1047/15 nm and 1017/45 nm channels see no signal as they have central wavelengths further away from the Doppler shifted light collected from the plasma. At such low temperatures a negligible signal in these channels is collected despite their broader bandwidth, as expected.

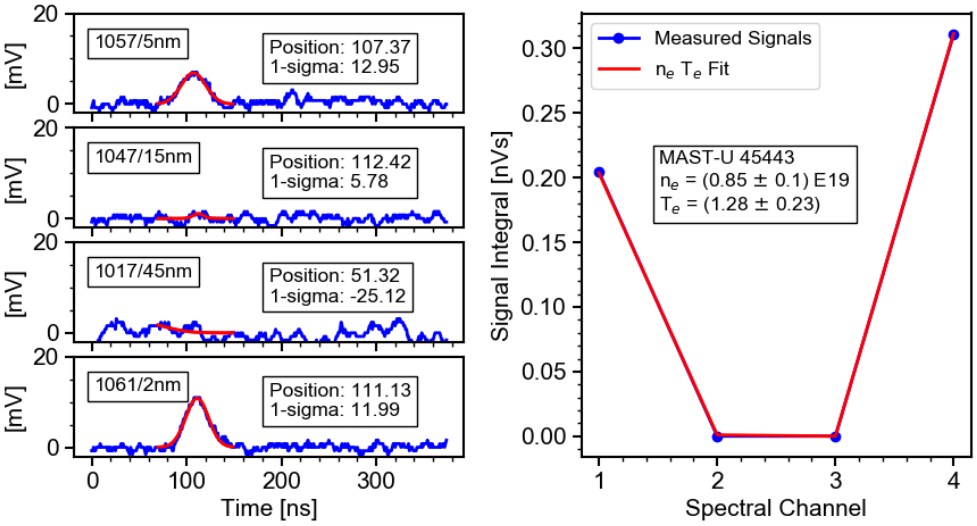

Figure 3.24: Scattered signals from MAST-U plasma 45443 and the associated fit to produce electron density and temperature values

The calculation of electron density and temperature is done in the MAST-U processing loop using the Gaussian integrals which are used in a fit to the analytical Selden function [46] along with the individual calibration values for each polychromator. The density values produced from this fit are produced with a calibration constant determined by rotational Raman scattering, as described in Section 4.2. The values of electron density and temperature at each spatial point are available several minutes after the plasma.

Chapter 4

MAST-U Divertor Thomson Scattering System Calibration

This chapter details the work carried out to calibrate the divertor Thomson scattering system. Section 4.1 covers the spectral calibration of a Thomson scattering polychromator and the methods used to calibrate the individual instruments involved in the calibration. Section 4.2 presents an introduction to Raman scattering and its for calibrating Thomson scattering diagnostics. The choice of a Raman scattering calibration over Rayleigh scattering for the MAST-U Thomson systems is also discussed.

Section 4.2 outlines the absolute calibration for the divertor Thomson system and the adjustments made to the optical alignment in order to commission the system. Results of Raman scattering experiments in Nitrogen are presented for the divertor Thomson system with a comparison to the core Thomson system which underwent a Raman calibration in parallel. Work contributing to the absolute Raman calibration and comparison of these results to the calibration of the core Thomson system is already published in [17].

4.1 Spectral Calibration

As spectral calibrations are routinely done for the Thomson polychromators there is a dedicated setup, seen in Figure 4.1a, used to perform these measurements. A white light source is directed through a rotating disc light chopper and a Princeton Instruments SpectraPro 2500i monochromator. A time-varying signal is needed to ensure that any DC offset measured by the polychromator electronics is not overlooked. This would cause . The monochromator has a variable slit width to set the measurement resolution. A typical value for this is 0.1 mm. The detector is connected to a PicoScope digital oscilloscope which digitises the signal and interfaces with a PC.

The output from a monochromator is produced by a Czerny-Turner spectrometer. A broadband white light source is input into the spectrometer. The light source passes through a narrow slit where it is imaged onto a diffraction grating. This grating spreads the incident light and images the varying wavelengths of light onto different spatial locations. The monochromator output is determined by a computer interface which allows the wavelength of the light to be controlled. The instrument function of the monochromator is determined by the diffraction grating and the width of the slit that images the light onto the grating. The output light passes through a lens which focuses the light into the fibre optic where the light illuminates the filter or polychromator under test.

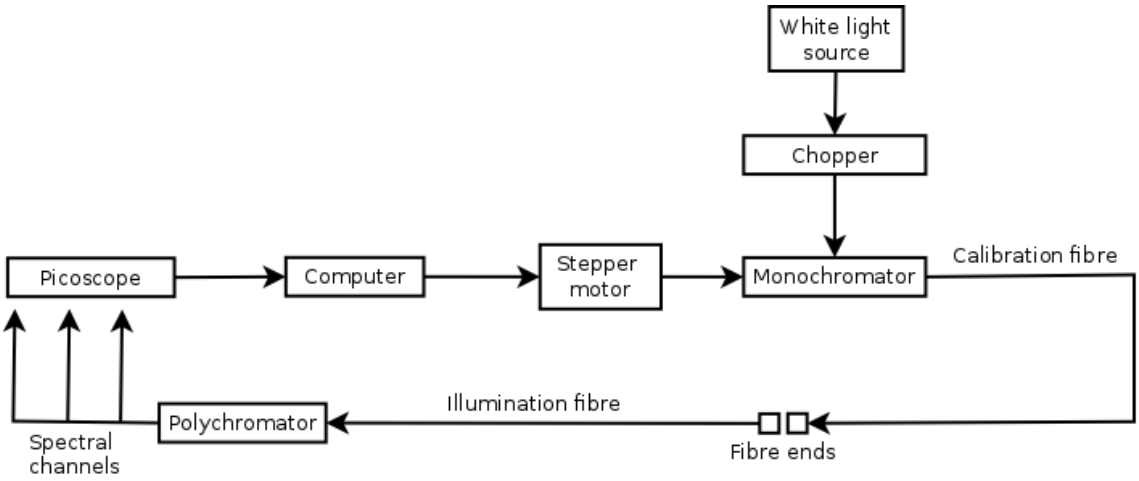

(a) Spectral calibration

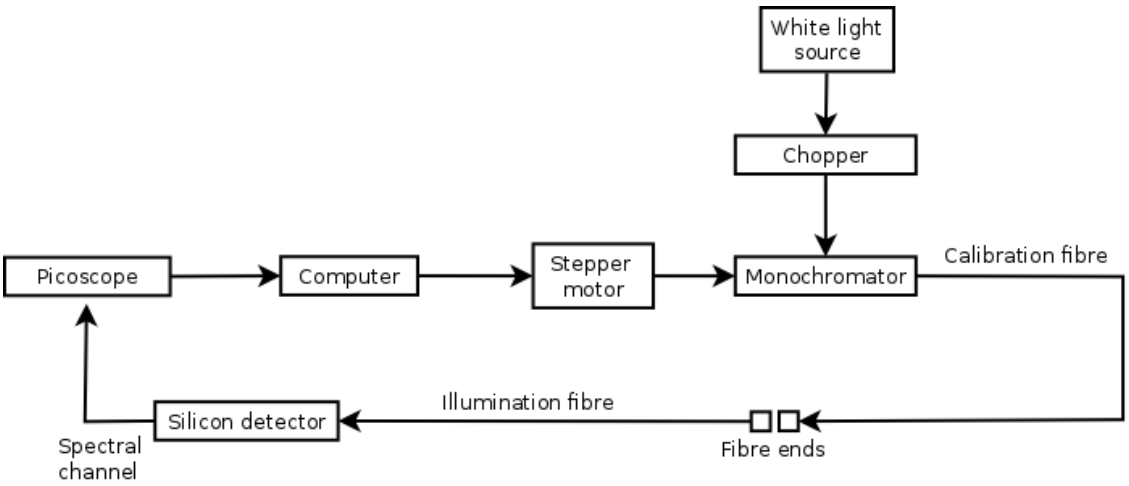

(b) Power calibration

Figure 4.1: Setup diagrams for polychromator calibrations

To account for the light source, and its variation in transmission as a function of wavelength due to the detector, a power calibration is performed using the setup shown in Figure 4.1b. A silicon detector is chosen to digitise the signal which has a calibrated wavelength response, as seen in Figure 4.2. This allows the natural variation in white light source spectrum to be accounted for when analysing the polychromator transfer functions.

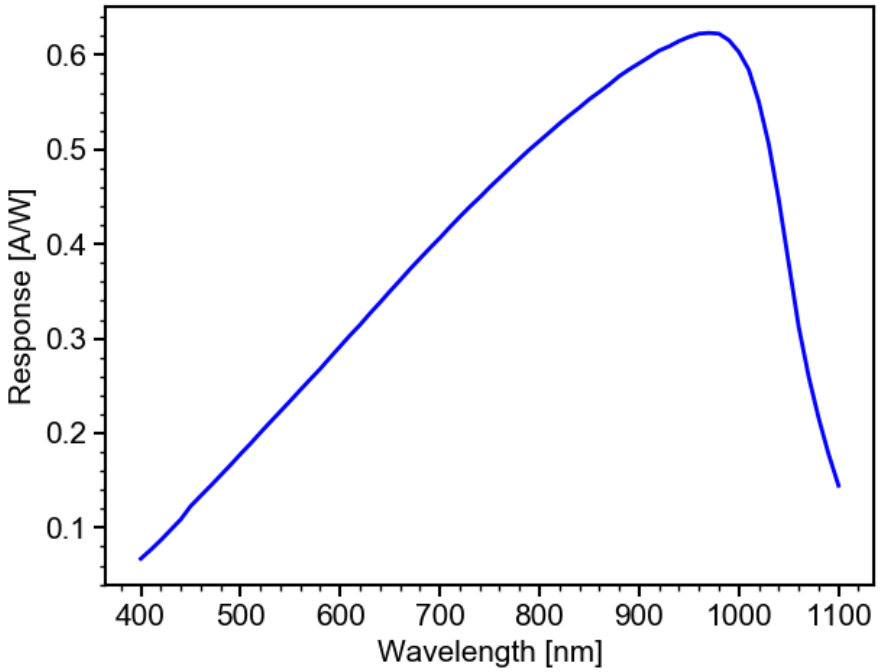

Figure 4.2: Responsivity of silicon detector used for power calibration

To ensure high resolution measurements of narrow band pass filters can be taken with this setup a Xenon source was tested in the same calibration setup, excluding the optical chopper, with a Xenon source replacing the white light source. This was done to see if the instrument function width of the monochromator would allow narrow line emission to be measured by the calibration system. This capability is required for the narrow band filter tests where the number of photons are vastly restricted. The instrument function defines the ability to determine the spectral resolution of the system. If the instrument function of the monochromator is too wide then the result of the measurement will be smeared at the edges. The 980.0 nm Xenon emission line was used for this with slit widths of 0.1 mm. The FWHM of the peak was measured to be 0.2 nm making it suitable for measurements of this nature. Given the line is meant to be at 980.0 nm and the peak corresponds to 980.1 nm it can be seen that the monochromator is suitably calibrated within the bounds of its error and this is appropriate to perform polychromator calibrations using a white light source.

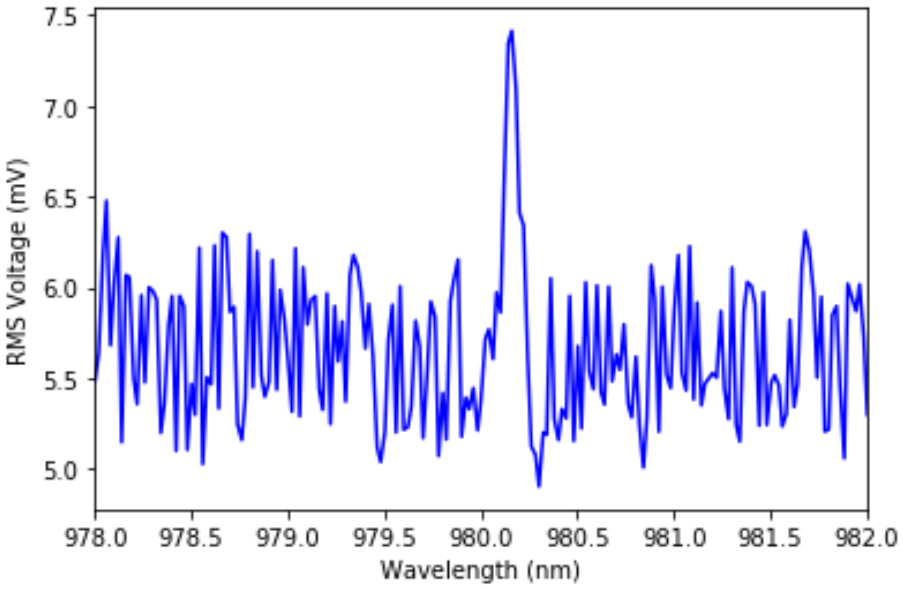

Figure 4.3: Emission from a Xenon lamp showing line at 980 nm used for calibration

4.2 Absolute Density Calibration

Absolute calibration of a Thomson scattering system is described in [58]. It is vital for a divertor based Thomson system in particular with the development of advanced operating scenarios. Detachment in particular adds significant interaction with neutral species into an already active region of the plasma. It undergoes a vast number of atomic processes such as excitation and recombination. These lead to intense levels of background light emitted from the plasma. This can saturate any of the Thomson spectral channels but it is a particular concern in the narrow spectral channels which are required for low electron temperature measurements in this region of the plasma.

A spectral calibration with a white light source and monochromator, as described in Section 4.1, is common for an interference filter based polychromator. The MAST-U Thomson system and a few other systems [53, 59] use Raman scattering to absolutely calibrate the signal level for each of the polychromators following a successful spectral calibration.

Raman scattering, which is typically carried out in Nitrogen for Thomson calibrations, has a cross section, $\frac{d\sigma_{Raman}}{d\Omega}$, of $7.41 \times 10^{-31}\text{cm}^2\text{sr}^{-1}$ [59]. There is also no cross section at the laser wavelength which means the only signal at the laser

wavelength is inherent stray light in the system, which is useful to discover prior to plasma measurements being taken. Tokamak based Thomson scattering systems such as the core MAST-U system regularly undergo calibrations in Nitrogen at pressures exceeding 100 mBar.

4.2.1 Rayleigh Calibration

Rayleigh scattering is still used to calibrate tokamak based Thomson scattering systems [60] but it is generally accepted that the best method of absolute calibration is Raman scattering [59, 61]. Despite this, Rayleigh scattering is regularly used for calibration of Thomson systems in low temperature plasma systems such as those in [28, 29] where gases such as Argon are used. Rayleigh scattering is useful on plasma systems of this kind as the technique only requires gas pressures on the order of a few mBar. This is due to the Rayleigh scattering cross section, $\frac{d\sigma_{Rayleigh}}{d\Omega}$, of Argon being $5.4 \times 10^{-32}\text{cm}^2\text{sr}^{-1}$ [40]. This results in roughly an order of magnitude greater signal than that due to Raman scattering.

While this is an advantage for establishing the technique, the large number of Rayleigh scattered photons often leads to saturation of the digitised channels, and can even damage the photodetectors in extreme cases. Due to this light blocking techniques such as neutral density filters are typically used to reduce the signal level and avoid any adverse saturation effects. In addition, Rayleigh scattered light only occurs at the laser wavelength so any sources of stray light such as dust, system geometry or any other gases in the vessel can contribute noise during the calibration. The divertor Thomson system itself makes Rayleigh scattering impractical by not measuring the light at the laser wavelength which is filtered out as a stray light mitigation technique for plasma measurements.

4.2.2 Raman Calibration

Raman scattering occurs at a series of discrete wavelengths about the laser wavelength λ_L [58]. Further detail about these discrete emission lines is outlined in Appendix A. The wavelength and intensity of the scattered light is dependent on the rotational and vibrational state of the molecule, typically Nitrogen, chosen for scattering. Generally the contribution from the vibrational states is sufficiently

large that it is outside of the wavelength range transmitted by the polychromators so only the cross section due to rotational Raman scattering is considered for MAST-U calibrations.

If the scattering molecule loses energy then the scattered photon gains energy and scatters at a lower wavelength. Raman lines at a greater wavelength than λ_L are known as Stokes lines and lines at a wavelength less than λ_L are known as anti-Stokes lines. As the core Thomson system only transmits blue shifted wavelengths only anti-Stokes lines are considered for the calibration of those polychromators. With the addition of the two spectral channels that transmit red shifted light for the divertor Thomson polychromators it is therefore possible to consider light collected in these filters from Stokes lines for the purposes of the Raman calibration.

Given there are already a suitable number of channels to produce a quality calibration and the reduced quantum efficiency of the silicon APDs at the red shifted wavelengths, which are at values increasing towards the operational limit of 1100 nm as determined by the silicon bandgap in the APDs, the two filters on the red shifted side of the spectrum were not used for the calibration of these polychromators. The divertor polychromators also feature an additional 1061/2 nm channel on the blue shifted side of the spectrum which transmits a contribution from a number of anti-Stokes lines. Due to the narrow bandwidth the signal to noise ratio was roughly half that measured in the other two blue-shifted channels so this channel was not used. The 1047/15 nm and 1057/5 nm filters and their overlap with the anti-Stokes spectrum can be seen in Figure 4.4.

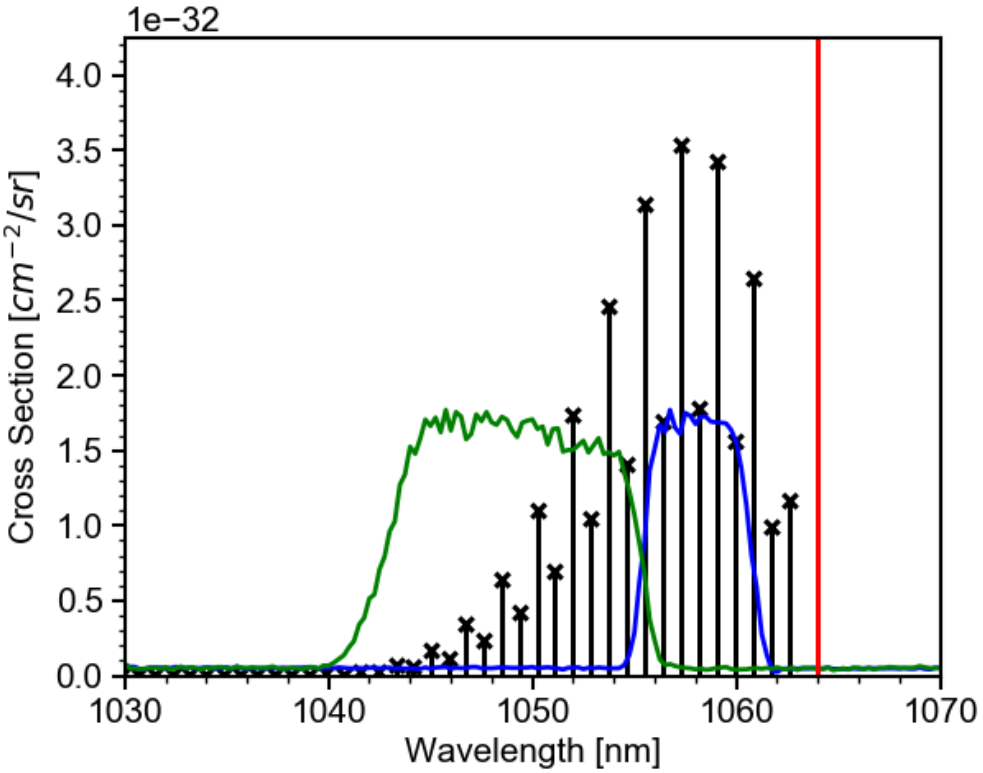

Figure 4.4: Anti-Stokes (black) lines of N_2 at 300 K with the transfer functions of the 1057/5 nm (blue), 1047/15 nm (green) filters and the 1064.1 nm laser line (red)

A Raman calibration requires a number of spectral channels close to the laser wavelength with high rejection of light outside the intended pass band. Given the design for low temperature operation of this system, with a number of spectral channels in close proximity to the laser wavelength, in an area of significant stray light such as the divertor, this requirement is comfortably met.

Unlike Rayleigh scattered light, which is singularly polarised parallel to the plane of the incident light, Raman scattered light has two polarisations:

$$\sigma_{Raman} = \eta_{\parallel}\frac{4}{7}\sigma_{Raman} + \eta_{\perp}\frac{3}{7}\sigma_{Raman} \tag{4.2.1}$$

where $\eta_{\parallel}$ and $\eta_{\perp}$ represent the fractions of the scattered light parallel and perpendicular to the incident beam polarisation respectively.

The polarisation of Thomson scattered light is parallel to that of the incident light. Any depolarisation effects [62] are negligible, as discussed in Section 2.3. A polariser positioned on the collection optic to remove perpendicularly polarised background light from being collected by the fibre optics is used on the core Thom-

son system. While this was intended as part of the design of the divertor system, this had not been installed at the time of first operation of the diagnostic. This was due to concerns about the magnitude of scattered light received during initial operation of the diagnostic, which turned out to not be a problem.

To absolutely calibrate the system the gas pressure in the vessel is varied with the scattered signal intensity measured for each gas pressure, as seen in Figure 4.5. To measure the signal intensity the lasers used for the calibration are fired for 5 s. Data is collected for ∼1 s with the 30 Hz repetition rate, as would be typical during the duration of a MAST-U plasma. After obtaining data for a number of gas pressures the reciprocal of the linear fit to the pressure scan is used to calculate the calibration constant for each of the polychromators and lasers used. This constant is determined for each of the spectral channels as the difference between the channels is accounted for by the difference in anti-Stokes cross section measured by the filters, as shown in Figure 4.4. It can be seen that the vertical offset for each channel in Figure 4.5 is negligible meaning there is minimal stray light present which is due to the stray light mitigation techniques employed in these polychromators, as discussed in Section 3.3.

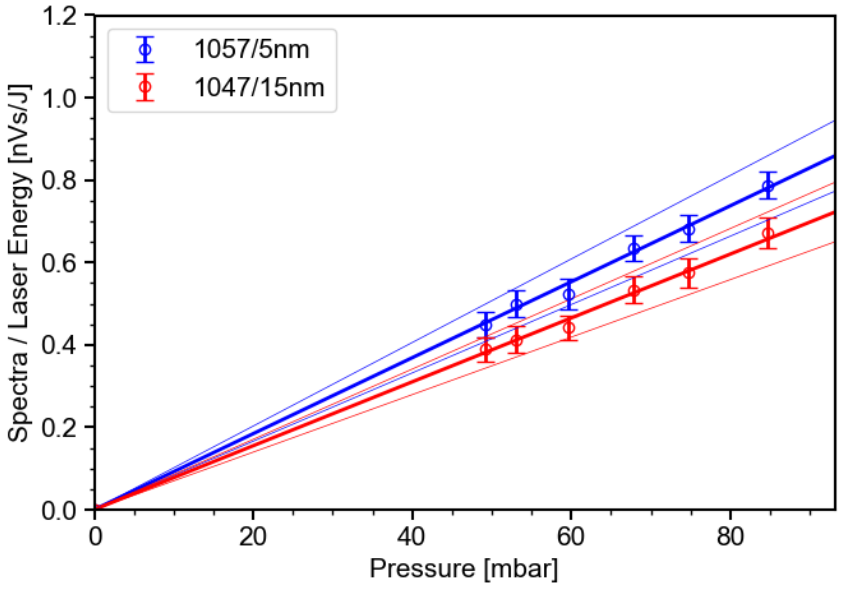

Figure 4.5: Linear pressure response for for Raman calibration of a divertor polychromator with 0.82 J of laser energy

The average scattered signal for a single pressure can be seen in Figure 4.6

which shows a comparison between the core and divertor systems during their calibration. Given the requirement of filling the vessel with Nitrogen and the associated disruption to plasma operations, it is convenient for the systems to be calibrated together as the diagnostics can run in parallel. It can be seen that accounting for the difference in laser energy there is a similar agreement in the signal transmitted at the same gas pressure which would be expected given the comparable optical transmission of the two systems.

There is a clear temporal offset in the two scattered signal pulses. While there would naturally be a small difference due to the differing optical path length of the two systems, a 30 ns offset is applied to the digitisers described in subsection 3.3.1 in order to distinguish the timing of the scattered signals between the two systems. This is particularly helpful when analysing the scattered signals in terms of their association with a particular laser. This was particularly useful during first commissioning of the diagnostic when the laser used for the divertor system was borrowed from the bank of core system lasers. The difference in Gaussian width between the core and divertor signals seen in Figure 4.6 is due to the altered Q-switch delay to reduce the laser energy, as described in Section 3.5.

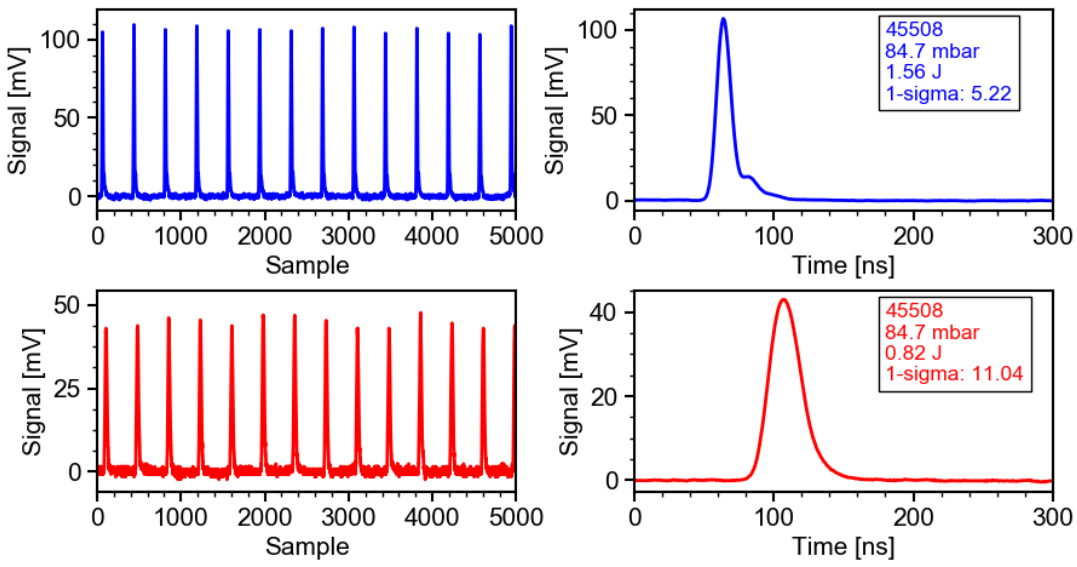

Figure 4.6: Comparison of Raman scattering signal level between a core (blue) and divertor (red) polychromator for 84.7 mbar with 1.52 J and 0.82 J of laser energy respectively

Along with the Raman signal, generated from the integral of the scattered signal, there is an associated error. This is given by the standard deviation of the Gaussian integrals over the laser pulses included in the data acquisition time. The fractional error in signal integrals can be seen in Figure 4.7. An error of $\sim$5% is observed, with variations around this value due to small fluctuations in the laser energy. Despite the fluctuations, the system demonstrates a good signal to noise level with good repeatability.

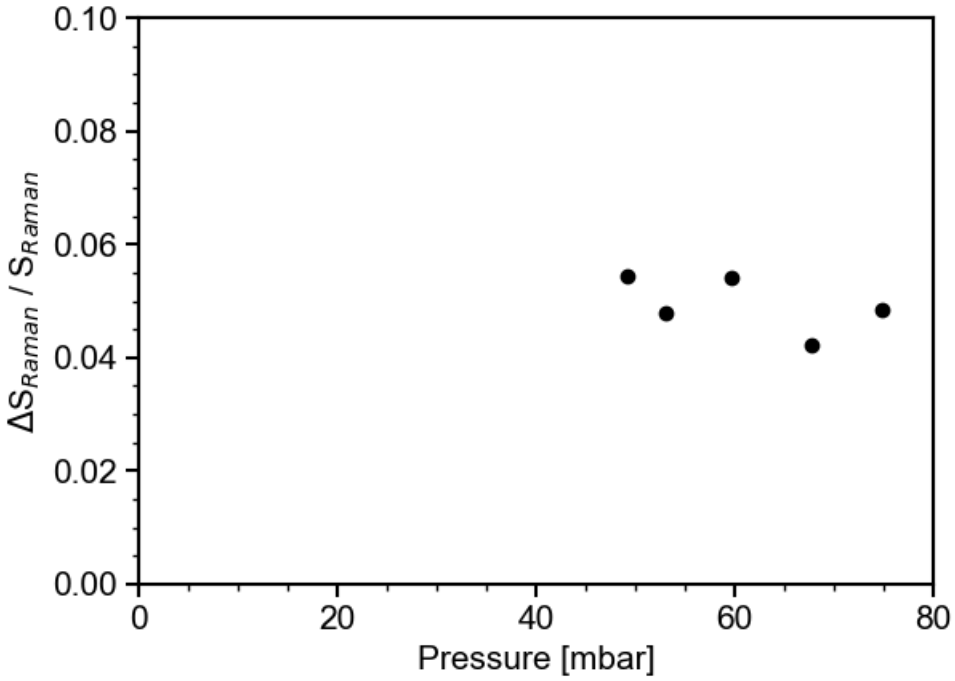

Figure 4.7: Fractional error of a 1057/5 nm channel in a divertor polychromator averaged over 1 s of laser pulses for a range of Nitrogen pressures

The backplane features two bifurcated fibres as described in subsection 3.2.4. With each fibre having a delay line, producing the second scattered signal pulse, the two bifurcated fibres are separated across the backplane. This allows for comparison between the two peaks transmitted by each fibre with the ratio between these peaks used as a measure of the system alignment. The fibre backplane allows for adjustments at both ends of the backplane in a clockwise and anti-clockwise manner which are used to raise or lower the image plane to adjust the alignment of the fibre image to that of the laser line in-vessel. The collection cell position can also be adjusted in either direction vertically to bring about a similar adjustment.

Table 4.1 shows the changes made to the backplane and collection cell over the course of a number of calibration shots as measured by their individual adjustment scales. These adjustments are very sensitive due to the size of the fibres relative to the mechanical adjustments available during the backplane movement. Despite this, it is crucial to be able to make these adjustments to alter the image plane which enables the signal received by the fibres to be optimised.

Shot	**Collection Cell (mm)**	**Backplane LHS (mm)**	**Backplane RHS (mm)**	**Comment**
46373	30.5	50.0	9.5	Starting position
46376	30.5	50.0	10.0	Slightly improvement on 201-208 but worse 506-509
46380	29.0	49.0	7.6	Best 201-208 but no signal 508 & 509
46386	29.5	49.3	7.6	Good signal across whole chord - final setting

Table 4.1: Adjustments made to collection cell during alignment procedure. Collection cell and backplane measurements are the heights according to their respective scales as fixed

Given the 2.02 mm vertical height for each of these fibres, a 2:1 ratio between the peaks shown in Figure 4.8 corresponds to a $\sim$0.5 mm discrepancy in the alignment. Considering the uncertainties associated with the sensitive adjustments to the fibre backplane and the daily fluctuations in the laser alignment, this is used as a measure of good alignment of the bifurcated fibres.

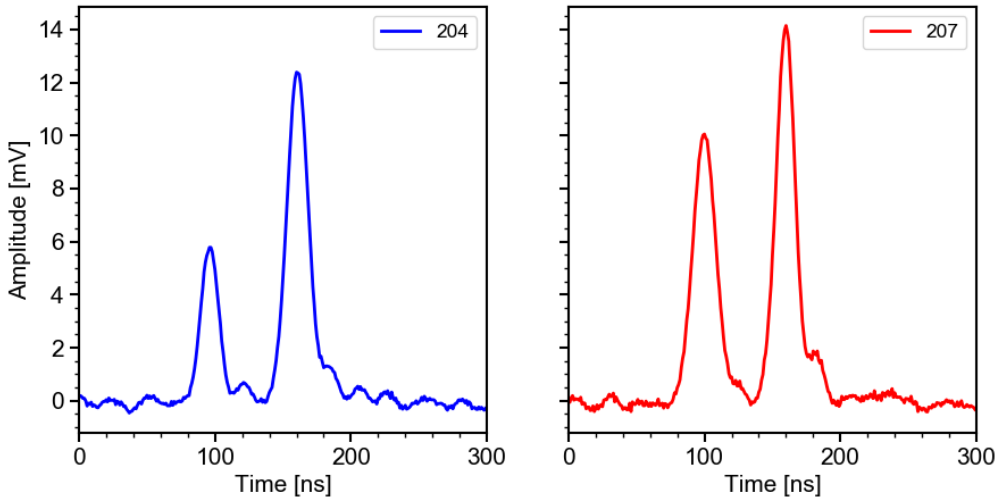

Figure 4.8: Bifurcated fibre signal traces for optical alignment in Nitrogen

Due to the precise nature of these adjustments they are typically made prior to carrying out a Raman calibration in Nitrogen as the result of any adjustments can immediately be seen without compromising plasma performance. In addition, if any further adjustments have to be made there is time allocated for subsequent entries into the tokamak area to carry out any corrections to the alignment. The Raman signal from the adjustments to the collection cell and fibre backplane outlined in Table 4.1 can be seen in Figure 4.9.

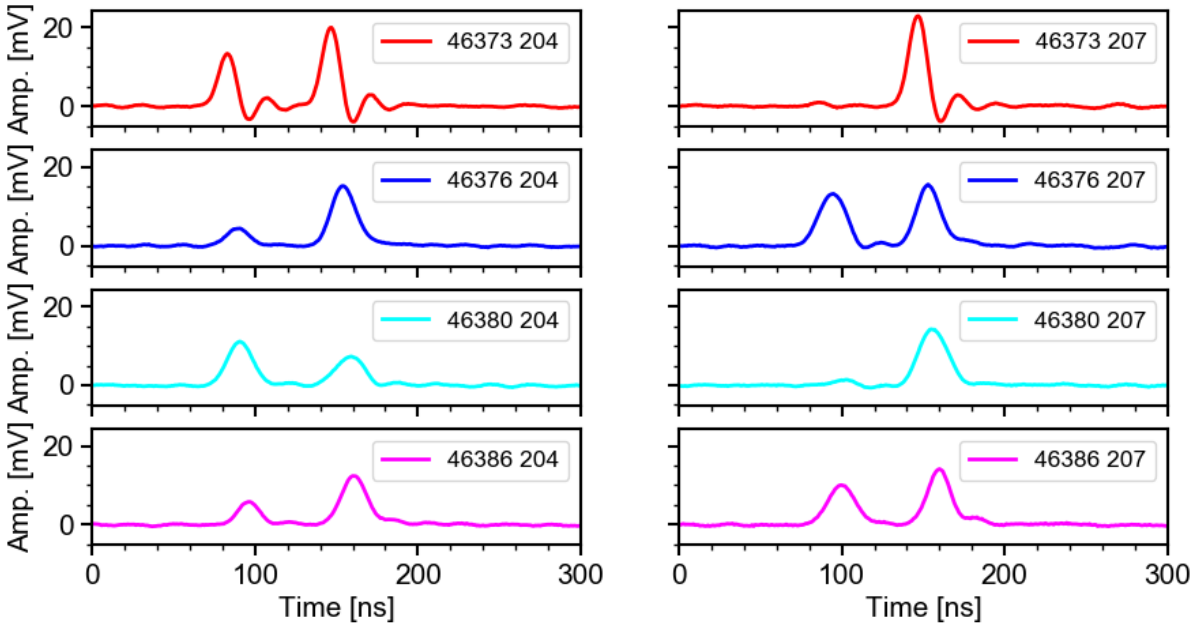

Figure 4.9: Bifurcated fibre signals during adjustments made to the fibre backplane

The integrated Raman signal for each polychromator can be used to evaluate any vignetting across the viewing chord. Given the closed geometry of the divertor and the likelihood of coils, cables or in-vessel components installed after the system design there is likely to be vignetting at some of the spatial points. As Raman scattering intensity, accounting for gas pressure and laser energy, produces a known intensity any losses due to vignetting will be accounted for with the individual calibration factor for each of the polychromators. To perform these measurements extra digitisation space was allocated which allowed all 12 spatial points, as shown in Table 3.1, to be active. This utilised all 8 of the divertor polychromators and 4 of the X-point polychromators, as shown in Figure 3.14.

The inclusion of the X-point polychromators was possible as they feature the same model of OD6 hard coated filters with the same central wavelength and bandwidth of filters on the blue shifted side of the wavelength spectrum. This allowed a Raman calibration to still be performed with the same spectral channels, as well as enable electron temperature measurements down to $\sim$1 eV. Even though there will be a difference in the transmission of these filters as they were produced during a different batch of production, any variation will be accounted for by the spectral and Raman calibrations.

It can be seen that there are two clear regions of vignetting due to the closed divertor covering. The first is from 1.25 m out to the Super-X divertor tile at 1.44 m. The second is from 1.18 m out to the 1.03 m. This is an important result as it demonstrated a good signal intensity across the entire viewing chord for the first time. Vignetting is inherently accounted for in the Raman calibration factor so that this does not factor into the electron density measurements at the spatial points that experience vignetting.

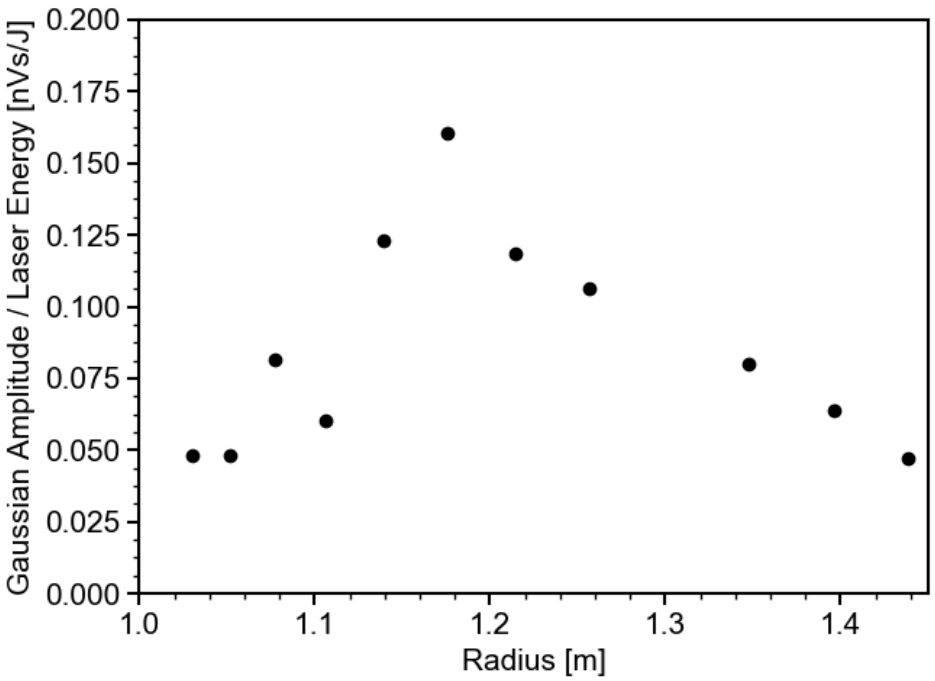

Figure 4.10: Gaussian integral from Raman scattering in Nitrogen normalised by the laser energy and the variation with radius for the divertor Thomson spatial points

Chapter 5

Thomson Scattering Analysis of Scrape-off Layer and Divertor Plasma

This chapter details analysis of data collected during MAST-U plasmas, with the exception of Section 5.6 which presents an analysis technique tested using MAST data collected in 2013. In Section 5.1 some of the background of MAST-U plasmas is discussed and a brief outline of the experiments that are covered in subsequent sections is provided. The work in Section 5.2 presents data from a number of MAST-U Super-X divertor plasmas collected using the divertor Thomson system. The parameter space of the electron density and temperature values is discussed and compared to MAST-U simulations. This data is compared to results from detachment experiments on the TCV tokamak where the electron temperatures observed during detachment is in contrast to that measured on MAST-U during this work.

Observation of Super-X divertor rollover in the electron density data measured by the divertor Thomson system is presented in Section 5.3. Radial electron density and temperature profiles from the divertor Thomson system are compared to Langmuir probe ion saturation measurements where the effects of detachment on these profiles is evident.

Measurements in plasmas achieving detachment in a single shot with a ramp in the gas fuelling are discussed in Section 5.4. Similar trends in the electron density and temperature are observed to those in the experiments discussed in Section 5.3. The divertor Thomson measurements are compared to the divertor monitoring

spectrometer (DMS) systems for one of these plasmas. Results from development of a divertor Thomson polychromator to include measurement of the Fulcher band, D_α and D_β emission are presented in Section 5.5. Each of their respective relationships with electron temperature during the gas ramp are investigated and show good agreement with other measurements in the Super-X divertor.

An analysis method for averaging Thomson scattering scattering signals is presented in Section 5.6. This enables measurements down to lower electron densities in the SOL. This method is benchmarked on MAST and compared to reciprocating Mach probe data which shows good agreement.

While analysis of data produced by the divertor Thomson system is still ongoing at the time of this thesis' writing, diagnostic work and data analysis has already resulted in, or contributed to, a number of publications:

J. G. Clark, M. D. Bowden and R. Scannell. *Low temperature Thomson scattering on MAST-U.* Rev. Sci. Instrum. **92**, 043545 (2021)

J. G. Clark, M. D. Bowden, Y. Kim, B. Parry, E. Rose, R. Sarwar and R. Scannell. *First divertor Thomson scattering measurements on MAST-U.* Rev. Sci. Instrum. **93**, 103534 (2022)

J. G. Clark, M. D. Bowden, J. R. Harrison and R. Scannell. *Thomson scattering measurements in MAST-U Super-X divertor plasmas.* Proc. 48th European Conference on Plasma Physics (2022)

K. Verhaegh, B. Lipschultz, J. R. Harrison, N. Osborne, A. C. Williams, P. Ryan, J. Allcock, **J. G. Clark**, F. Federici, B. Kool, T. Wijkamp, A. Fil, D. Moulton, O. Myatra, A. Thornton, T. O. S. J, Bosman, C. Bowman, G. Cunningham, B. P. Duval, S. Henderson, R. Scannell and the MAST Upgrade Team. *Spectroscopic investigations of detachment on the MAST Upgrade Super-X divertor.* Nucl. Fusion. **63**, 016014 (2023)

5.1 Introduction

A MAST-U experiment will consist of a number of plasmas, colloquially referred to as shots, that are designed to investigate a certain behaviour or engineering parameter. Generally the approach taken is to develop a number of baseline plasma scenarios. MAST-U scenarios are normally defined by their plasma current, divertor configuration and neutral beam heating power. A baseline scenario will be used for a number of different experiments with minor changes made according to the experimental parameter under test. This often forms a reference to change common parameters such as auxiliary heating, fuelling and plasma shape. Given that the divertor Thomson scattering system requires the plasma to be in a Super-X divertor configuration to obtain data, the diagnostic can only produce electron density and temperature data for plasmas operating in that configuration. During the work of this thesis there were a number of Super-X experiments run on MAST-U where the divertor Thomson system was producing data. Most of these experiments were centred around detachment access in the Super-X divertor configuration and comparison to the conventional divertor.

5.2 Super-X Divertor Parameter Space

The electron density and temperature parameter space was profiled by the divertor Thomson system which was operational for 68 plasmas in the first MAST-U campaign after commissioning. All of these plasmas were ohmically heated in their Super-X phase but there were generally two different scenarios used, either 600 or 750 kA plasma current. These scenarios used a number of different fuelling quantities and locations but the gas injected was always deuterium. As well as the different plasma current for the two scenarios there was a significant difference in the alignment of the divertor strike leg with the divertor Thomson laser line, shown in yellow in Figure 5.1.

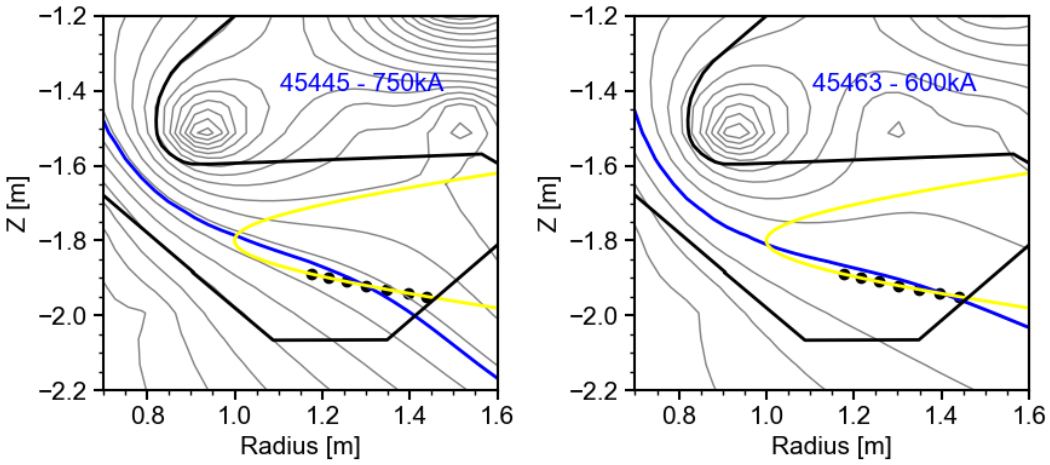

Figure 5.1: Comparison of divertor Thomson alignment in the Super-X configuration for 45445 (left) and 45463 (right) at 500 ms and 750 and 600 kA plasma current respectively

The 600 kA scenario incorporated specific adjustments to the divertor coils to align the strike leg with the divertor Thomson laser whereas the 750 kA scenario did not. As a result the angle the field line makes across the laser chord varies significantly between these two scenarios. It is expected that for the 750 kA scenario, in addition to any gradients in the electron density and temperature profiles inherent to the divertor, there will also be an additional impact of the alignment caused by proximity of the sampled spatial points to the strike leg. It can be seen that the spatial points are distributed either side of the strike leg. This means that some are in closed, confined magnetic field lines ($\psi_N < 1$) and some are in open magnetic field lines ($\psi_N > 1$) that are expanding out to the divertor tiles.

Given the Super-X is designed to operate with magnetic flux expansion to decrease the electron temperature at the target, it is expected that these two conditions would be distinguishable in terms of the electron density and temperature values. With the fall-off in the magnetic field strength it would be expected that spatial points at larger radius, or normalised poloidal flux, would correspond to a reduction in electron density and temperature. This is analogous to the fall-off in electron density and temperature seen in the SOL at the midplane, as measured by the core Thomson system. This is similar behaviour to that seen when the strike leg was placed right at the bottom of the Super-X tile and the electron density and temperature values measured by the divertor Thomson system were not able to be resolved due to low electron density and temperature values at the

measurement points. The low electron density and temperatures fell outside the operational limits of the diagnostic such that not enough scattered photons were collected in the at least two of the channels to be able to resolve a measurement. As the 600 kA scenario plasmas positioned the strike leg to align with the divertor Thomson laser, the variation associated with separation from the strike leg is less significant in comparison.

The electron density and temperature parameter space for 21 Super-X divertor plasmas is shown in Figure 5.2. These were chosen based on plasmas avoiding disruption events that terminated the plasma, events that caused the real-time plasma protection system into an early safe stop of the plasma or those that had poor laser alignment early in the scenario development, such that no usable data was obtained. The resulting dataset shows both the 600 and 750 kA scenario, which include different fuelling rates and fuelling locations. It shows that despite the differences in alignment, heating power and fuelling rate the majority of plasmas were at a lower electron density ($\sim 1 \times 10^{19}\,\mathrm{m}^{-3}$) and temperature ($\sim$1 eV) than expected based on simulations carried out before the first operation of the Super-X divertor [63]. Despite these values being lower than intended for routine operation, based on the initial design of the diagnostic, high quality data was still obtained as the plasma parameters did still fall within its operating range. Given the lower than expected electron temperatures measured in the Super-X divertor and the difference in electron temperature measurement range produced by the divertor and X-point polychromators, as discussed in Section 3.3, the X-point polychromators were used for the majority of the experimental results in this thesis. Results obtained using the divertor polychromators were made having carried out the adjustment to the angle of incidence of the 1061/2 nm filter based on the initial results operating this diagnostic, as described in Section 3.3.

It can be seen from Figure 5.2 that there is little difference in the range and distribution of electron density and temperature values between the 600 and 750 kA scenario. While there is a clear difference in the occurrence of these values, this is accounted for by the number of shots included in the two databases. Although there are clear alignment differences, it can be seen that even though the 750 kA scenario includes a number of shots at higher plasma current there is little difference in the

two distributions aside from a few data points at higher density and temperature. Given the difference in heating power it was expected that the two scenarios would have had a bigger difference in terms of electron density and temperature values but this was not observed.

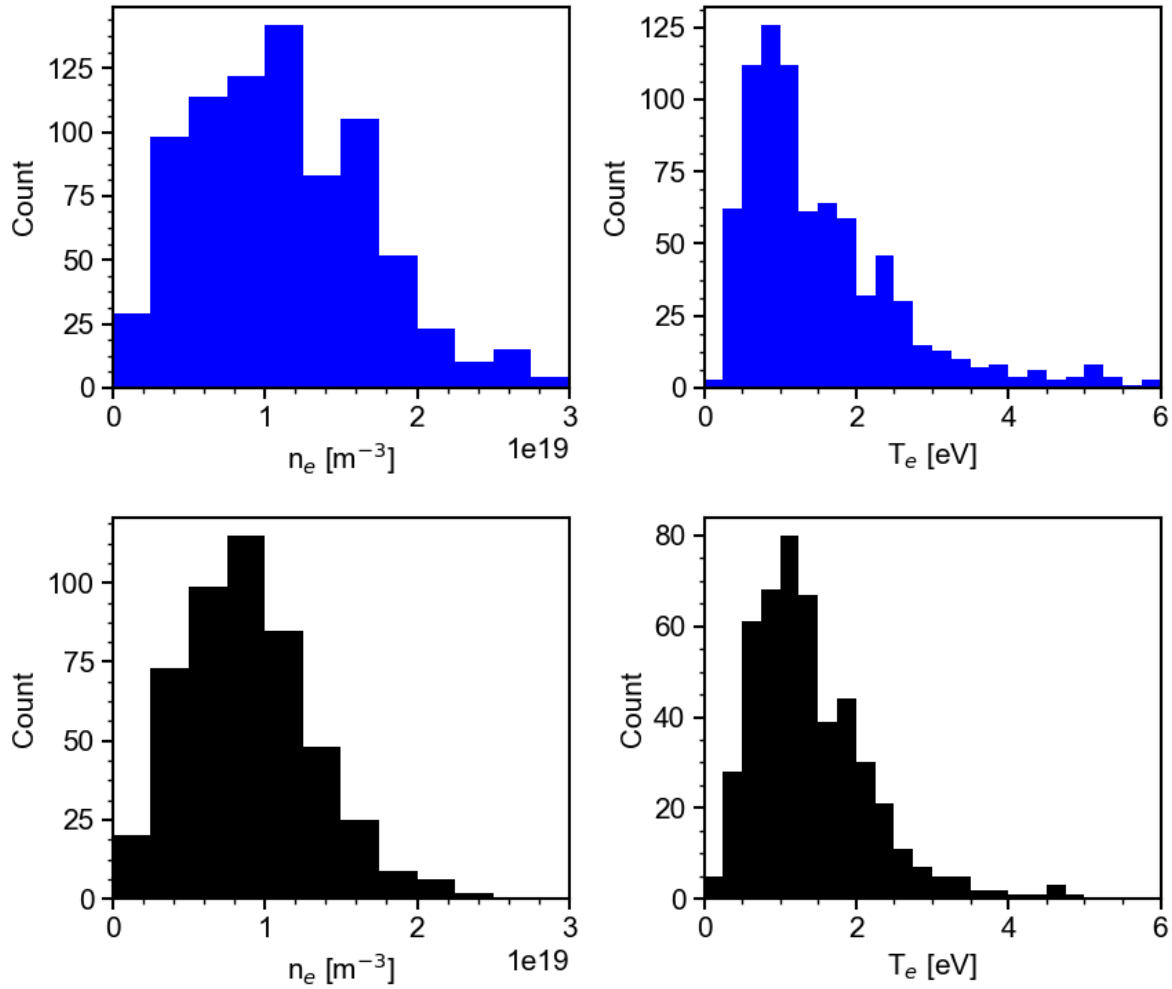

Figure 5.2: Histogram of electron densities (left) and temperature (right) values from divertor Thomson scattering spatial points for a 750 kA plasma scenario (blue) and 600 kA Super-X divertor plasmas

It was observed that these plasmas covered a range of attached, partially detached and deeply detached plasmas based on spectroscopy measurements, signatures of electron-ion recombination and Langmuir probe rollover measurements. This showed that despite the degree of detachment, the electron temperatures measured in the Super-X divertor were very low, on the order of a few eV. This is surprising given that other studies have found detachment onset below $\sim$5 eV

[64] where as MAST-U has observed attached plasma conditions at lower electron temperatures than that. The electron temperature values in particular were lower than predicted by simulations [63]. An explanation for this could be the lack of GDC in the divertor. Absence of this meant that any gas particles present on the divertor tiles after the previous plasma were not cleaned from the divertor chamber in between plasmas. The impact of this is that regardless of the set fuelling level the plasma could liberate deuterium gas stored in the tile surfaces so a higher concentration of neutrals would be present in the plasma. The effect of this would be a reduction in the electron density and temperature due to recycling from the divertor surface. There was also no cryopump, a designed enhancement for the MAST-U project, active during these plasmas. Due to this the level of neutrals was not controlled, or even accurately measured, during these plasmas. Combine this with the lack of GDC and recycling and various other atomic processes occurring in the divertor [15] this would explain the electron density and temperature of the Super-X divertor for these plasmas. In future campaigns it is expected that with greater neutral control from cryopumping and inter-shot divertor GDC, higher densities and temperatures will be observed by this system.

5.3 Super-X Divertor Detachment Measurements

As part of the first MAST-U physics campaign an experiment was carried out using the 600 kA scenario discussed in Section 5.2 and shown in Figure 5.1. The aim of this experiment was to achieve a divertor 'rollover' and observe detachment in the Super-X divertor. As previously discussed, these plasmas all prioritised alignment to the divertor Thomson laser line so any effect on the data from misalignment with the strike leg is negligible. The data selected for this study consists of 6 plasmas outlined in Table 5.1 that had 400 ms in their Super-X period until ramp down, apart from 45463 which only lasted 300 ms in Super-X phase.

Shot number	Divertor	Description
45443	Super-X	600 kA ohmic reference shot with 45 V midplane fuelling
45456	Super-X	Repeat of 45443 with 55 V fuelling
45459	Super-X	Repeat of 45456 with 60 V fuelling
45461	Super-X	Repeat of 45459 with 65 V fuelling
45462	Super-X	Repeat of 45461 with 70 V fuelling
45463	Super-X	Repeat of 45462 with 75 V fuelling

Table 5.1: Description of shots used in this section. Fuelling voltage refers to voltage supplied to piezo-electric fuelling valve

Each of these shots has a clear difference in the core line integrated density trace from the interferometer. These differences are the result of changes to the plasma fuelling, from the same midplane location, over a number of shots. Each fuelling level was kept constant throughout the Super-X phase of the plasma, as can be seen in Figure 5.3.

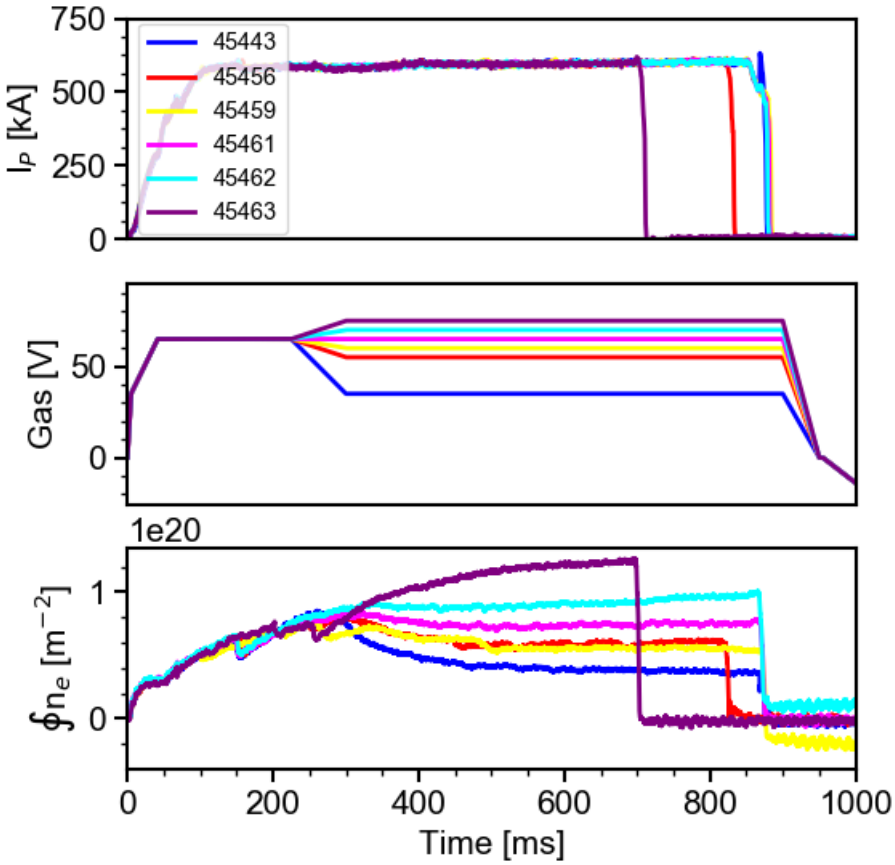

Figure 5.3: Plasma current (top) Deuterium gas fuelling (middle) and core line integrated density(bottom) diagnostic traces for the shots in Table 5.1

The effect of the fuelling scan can be examined in terms of radial Thomson profiles. Given the fuelling rates explored, it is expected that the density and temperature profiles will have different relationships with the fuelling rate. It is expected that at the low fuelling rates the divertor will be attached and as a result the divertor density will continue to increase with fuelling up until the point of rollover. Beyond that point any further increase in fuelling will result in a drop in the divertor density. It is expected that the divertor temperature will decrease monotonically throughout, as the degree of detachment increases. Evidence of these effects on the electron density and temperature in the divertor can be seen in Figure 5.4 where the electron density and temperature parameter space of the shots in Table 5.1 is shown.

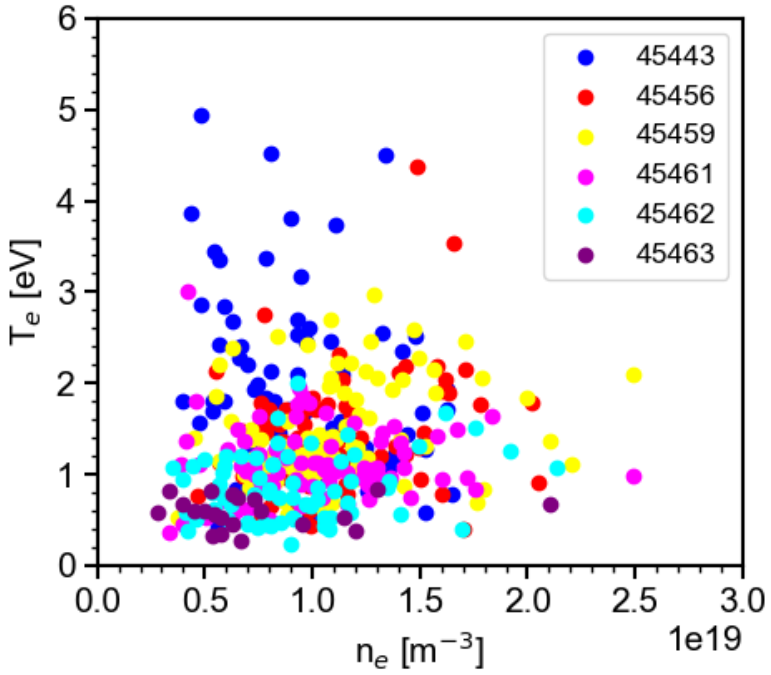

Figure 5.4: Electron density and temperature space for the shots in Table 5.1

Taking three of the shots from Table 5.1 with 45443 (low), 45461 (medium) and 45463 (high) fuelling rates the divertor Thomson profiles are shown in Figure 5.5 for these three shots at the same point in time, 545 ms. It can be seen that the low fuelling case has the highest electron temperatures of ∼2 eV and a density in the range 0.5 - 1 × 10^{19} m^{-3} across the radial profile. The increase in fuelling for 45461 shows a drop in electron temperature across the profile, particularly closer to the target. The density profile however sees an increase towards the divertor entrance but the density close to the target is beginning to drop. This behaviour is indicative of being close to the rollover point given the electron pressure is no longer being conserved at points along the profile, particularly those close to the divertor target.

The further increase in fuelling for 45463 shows a significant drop in the temperature down to ∼0.5 eV with a flat response across the profile. At this point in the shot there is little signal being measured at the spatial points near the target. This is due to the low electron temperature plasma where not enough scattered photons in the low temperature polychromator channels are detected to resolve a measurement. As a result the diagnostic is reaching its operating limit and a fit to produce electron density and temperature values is no longer possible at these

spatial points. The density for this profile sees a significant drop down to $\sim 5 \times 10^{18}$ m^{-3} with a reduction in the gradient across the spatial points. Divertor plasma at a density and temperature of such values is indicative of deep detachment. The three detachment stages of the Thomson profiles shown here agrees well with Langmuir probe ion saturation data which indicates that 45443 is in an attached state, 45461 is close to the rollover point and 45463 is in deep detachment.

Being able to observe such behaviour with the Thomson system and comparing favourably to other diagnostics operating in the divertor is vital. This is particularly encouraging at electron density and temperature values lower than anticipated during the design of the system. It shows that even below the expected MAST-U operating values [63], particularly based on the design of the system [16], the diagnostic is still able to measure to such low electron density and temperature values, and able to observe the consequences of detachment on the electron density and temperature profiles.

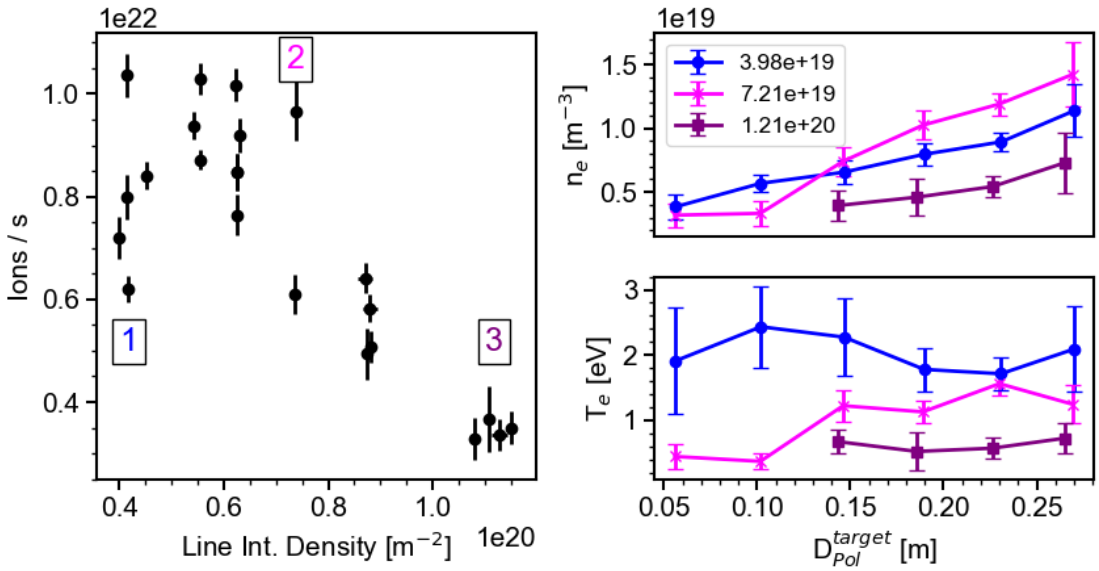

Figure 5.5: Langmuir probe ion flux measurements (left) showing divertor rollover and corresponding divertor Thomson profiles (right) plotted against the poloidal distance to the target based on the magnetic equilibrium reconstruction. Langmuir probe data provided by P Ryan (UKAEA)

To provide further insight into the electron density and temperature profiles in the midplane SOL, a comparison between the core and divertor Thomson systems

for the shots in Table 5.1 was performed. This is enabled by the timing of the MAST-U Thomson lasers [48] which allow midplane SOL and divertor Thomson profiles to be obtained simultaneously. As the midplane spatial points extend out into the SOL this allows the behaviour surrounding the separatrix to be compared with the two systems. This is done by mapping the radial points from the two Thomson systems into normalised poloidal flux space using the MAST-U equilibrium code [25].

Given the alignment of the strike leg to the divertor Thomson laser all of the spatial points in the Super-X phase of the shots in Table 5.1 fall within $0.95 \leq \psi_N \leq 1.05$ i.e. 5% of the separatrix position in normalised poloidal flux space. For the midplane Thomson system there are typically 3-4 spatial points that fall within this criteria. While the lasers used in the two systems during these plasmas had the same frequency, there are multiple lasers used in the midplane system to increase the temporal resolution and as a result the laser timing is spaced out. To minimise the difference in time between the two datasets, midplane Thomson data was taken from the laser that fired closest to the divertor laser. For these shots the separation between the two laser pulses was on the order of $\sim$10 ms.

Averages for electron density and temperature values were taken for the spatial points that fell within the ψ_N condition for the two systems. It can be seen in Figure 5.6 there are differing relationships between the electron density and temperature data in the midplane SOL and divertor with increasing upstream density. The electron density in the midplane SOL monotonically increases with the upstream density. Meanwhile the electron density in the divertor increases until $\sim 7 \times 10^{19}\,\mathrm{m}^{-2}$ where it starts to decrease with further increases in the upstream density. This is indicative of divertor rollover and corresponds to the behaviour seen for individual profiles in Figure 5.5. As expected, it can be seen that there is a monotonic decrease in the electron temperature surrounding the separatrix as measured by both systems during this detachment scan. As a result of this the electron pressure (en_eT_e), where e is the electron charge, is not being conserved once the divertor reaches the rollover point and begins to detach.

Due to the differing relationships with the upstream density, the ratio between the density and temperature measurements for the midplane SOL and divertor is

again in contrast. The ratio of the electron density data shows a large discrepancy between the midplane SOL and divertor densities during attached conditions but due to the outlined observations of the two relationships with the upstream density, there is a negative relationship between this ratio with the upstream density. During attached conditions the density in the divertor is ∼3x that in the midplane SOL but by the time the divertor is deeply detached the density measured in the two regions is approaching unity. In contrast, the ratio of the temperature in the SOL and the divertor has very little relationship to the upstream density which shows that they are varying at a similar rate.

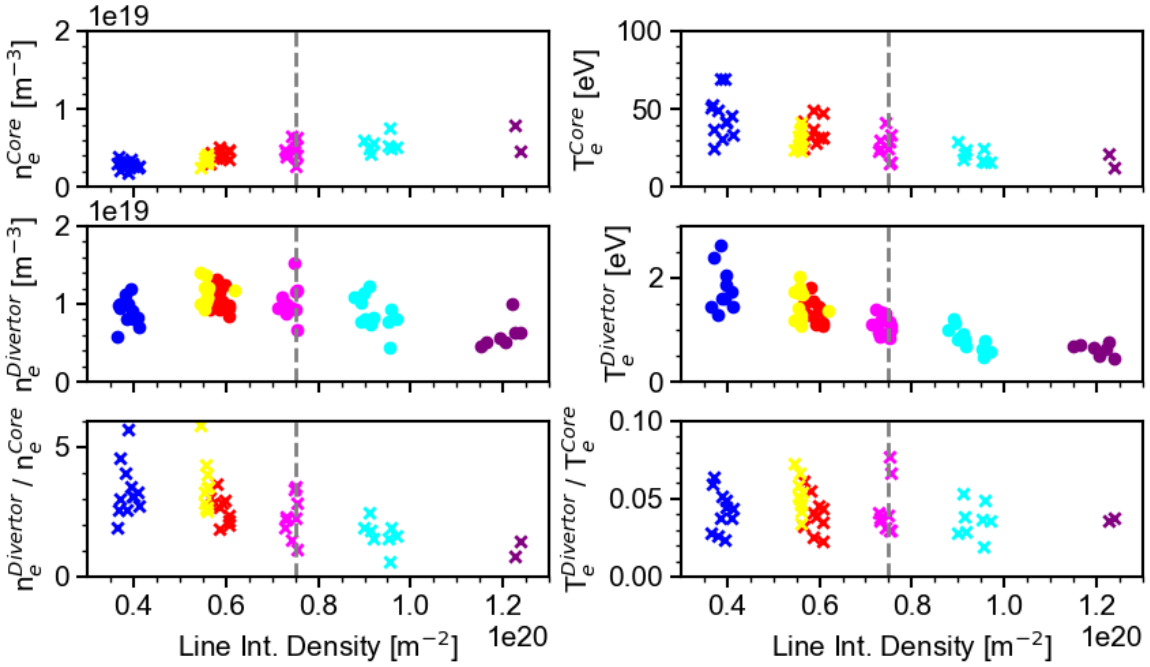

Figure 5.6: Average of midplane SOL (top) and divertor (middle) Thomson data and the ratio of the two (bottom) for electron density (left column) and temperature (right column) data between $0.95 \leq \psi_N \leq 1.05$

Even though the divertor conditions are of primary concern during a detachment experiment, the conditions in the midplane SOL are still of extreme importance. As the purpose of testing current divertor configurations is to achieve a suitable power solution for next generation devices. Any successful alternative divertor configuration will have to show the solution to the exhaust problem during reactor relevant conditions. During this experiment there were no shots that successfully injected significant auxiliary heating power into a stable Super-X plasma

while the divertor Thomson system was active. A comparison between the differences in electron density and temperature, between otherwise identical ohmic and neutral beam heated plasmas, would have been beneficial but this was not possible during this work.

Early MAST-U plasmas showed that the closed Super-X divertor reduced the L-H transition [10] power threshold due to improved confinement of neutrals in the divertor from the closed baffle which stopped them from reaching the core as impurities, as predicted by simulations [65]. While the operating regime of a future fusion power plant is unknown, given the benefit of high confinement mode (H-mode) [10] on core confinement and density and temperature profiles, it can be assumed that this is the most likely solution available at present. As a result, H-mode plasmas in the Super-X configuration are of great interest, particularly the access to detachment in this regime.

The results obtained show the ability of the divertor Thomson system to diagnose rollover in the electron density profiles during a detachment scan carried out over subsequent MAST-U plasmas. The two Thomson systems allow the first simultaneous analysis of electron density and temperature profiles in the midplane SOL and divertor during operation of the Super-X divertor. As the plasma results presented were intentionally kept in L-mode there is no comparison between the detachment access in the Super-X configuration or electron properties in L-mode and H-mode plasmas. There are H-mode Super-X divertor plasma experiments planned in future physics campaigns but development of a successful plasma scenario for this did not fall within the time frame of this work. The successful operation of this diagnostic has provided further insight into the consequences of detachment on the electron population as well as facilitating better comparisons to simulation and theory. In the future the commissioning of the X-point Thomson scattering system will further enhance the diagnostic capabilities of MAST-U and the ability to facilitate the study of particle transport, detachment and operation of the Super-X divertor through Thomson scattering analysis.

5.4 Gas Ramp Measurements

As well as achieving detachment over a series of shots, a number of experiments were carried out to take a plasma from close to the detachment threshold and into a detached state, with a ramp in the gas fuelling level. The reference plasma used for this was a 600 kA ohmically heated Super-X divertor plasma, as seen in Figure 5.7. The scenario used for this plasma did not align the divertor strike leg with the divertor Thomson laser. There will be some reduction in the electron density and temperature measured locally at a distance away from the strike leg. Given the results presented in Section 5.2 and the comparison to **??** the impact of the misalignment is not expected to be significant given the typical electron density and temperature values measured in detached Super-X plasmas in this work.

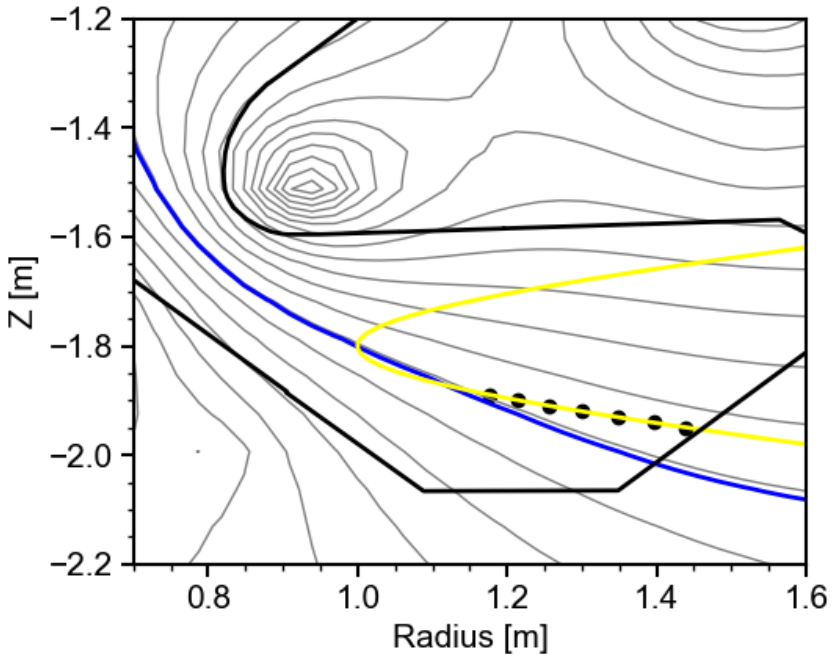

Figure 5.7: Plasma equilibrium reconstruction for MAST-U plasma 45371 at 500 ms

Based on previous generations of this scenario, the combination of this upstream density and fuelling was known to produce a plasma close to the onset of detachment. To bring about a detached state, once the plasma transitioned into Super-X at 400 ms deuterium gas was pumped in to the divertor on the low field side, close to the divertor target as seen in Figure 5.8. While increasing the fuelling in the core would be expected to increase the degree of detachment, fuelling

directly into the lower divertor near the target will have a more immediate impact on the divertor conditions.

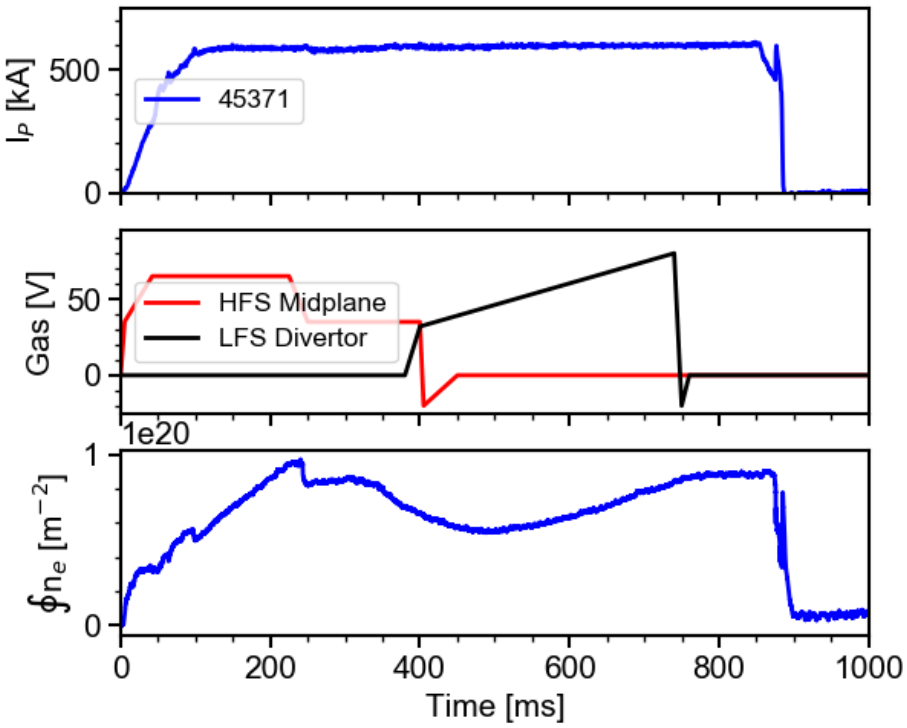

Figure 5.8: Plasma current (top), high and low field side gas fuelling (middle) and core line integrated density (bottom) data traces for 45371

Given the proximity to the detachment threshold it is expected that the electron density and temperature values would be $\sim 1 \times 10^{19}\,\mathrm{m}^{-3}$ $\sim 1.5\,\mathrm{eV}$ respectively. Based on the behaviour seen in Figure 5.6 an increase in the fuelling would be expected to bring about a period of increase in the electron density before seeing it begin to decrease with continued fuelling. Throughout this fuelling the electron temperature would be expected to decrease monotonically.

To observe the effect on the divertor conditions during this gas ramp the divertor Thomson system was active during the Super-X phase of this plasma. Figure 5.9 shows divertor Thomson profiles of the electron density and temperature with respect to the poloidal distance to the divertor tile at 100 ms intervals after the onset of the fuelling. It can be seen that there is an initial increase in the electron density up to 635 ms before a significant drop in electron density after this time. The electron temperature however decreases monotonically to the point where the diagnostic is operating close to its limit of detecting a plasma at this

temperature given that there is only one spatial point where a measurement point can be resolved. This corresponds to electron density and temperature values of $\sim 4 \times 10^{18}\,\mathrm{m}^{-3}$ and $\sim 0.3\,\mathrm{eV}$ respectively. This behaviour shows good agreement with the behaviour presented in Section 5.3 but replicated in a single shot with a gas ramp, rather than a constant fuelling level increased in stages over a number of subsequent plasmas.

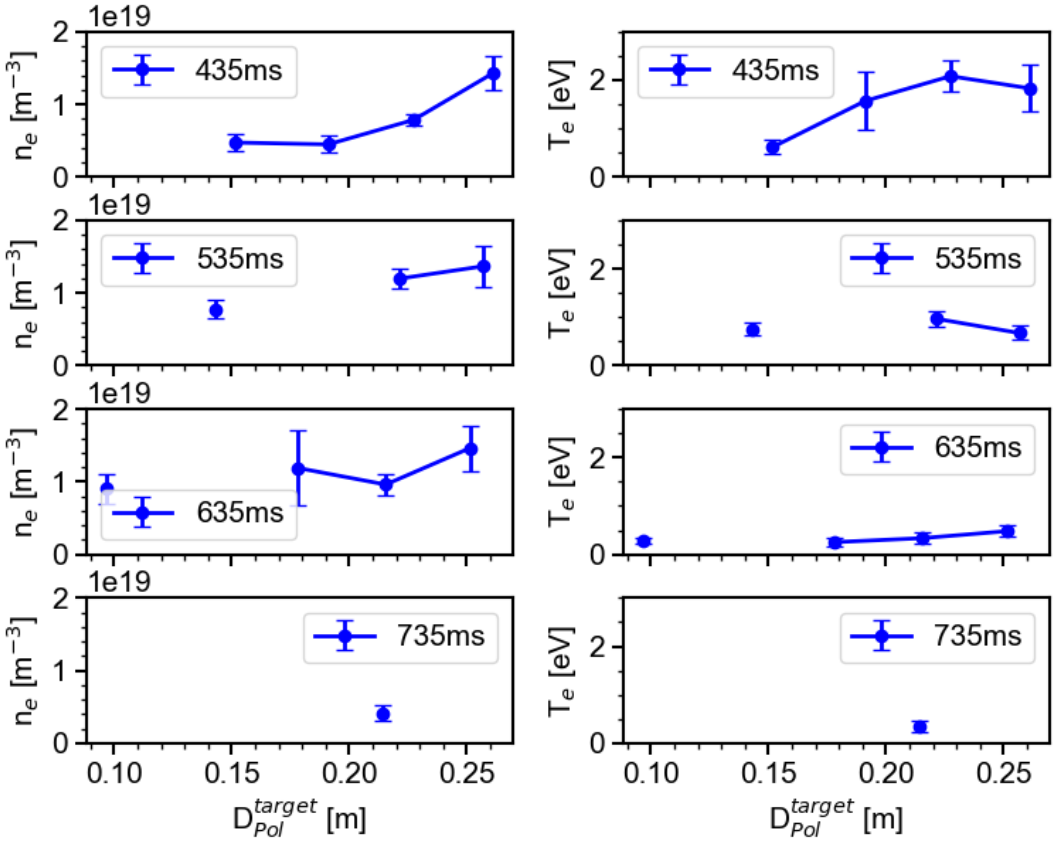

Figure 5.9: Temporal variation in electron density (left) and temperature (right) profiles with poloidal distance from Super-X target for 45371

Also operating during this plasma was the divertor monitoring spectrometer (DMS) which measures plasma emission at a number of wavelengths along 20 lines of sight across the divertor chamber. There are two DMS spectrometers, 'DMS-York' and 'DMS-CCFE' which operate in parallel from two different view points. The lines of sight of the two systems, the divertor Thomson spatial points and plasma equilibrium for 45371 can be seen in Figure 5.10. While the DMS lines of sight produce line integrated measurements, it does allow comparison with the divertor Thomson due to the overlap between the viewing chords of the two diag-

nostics.

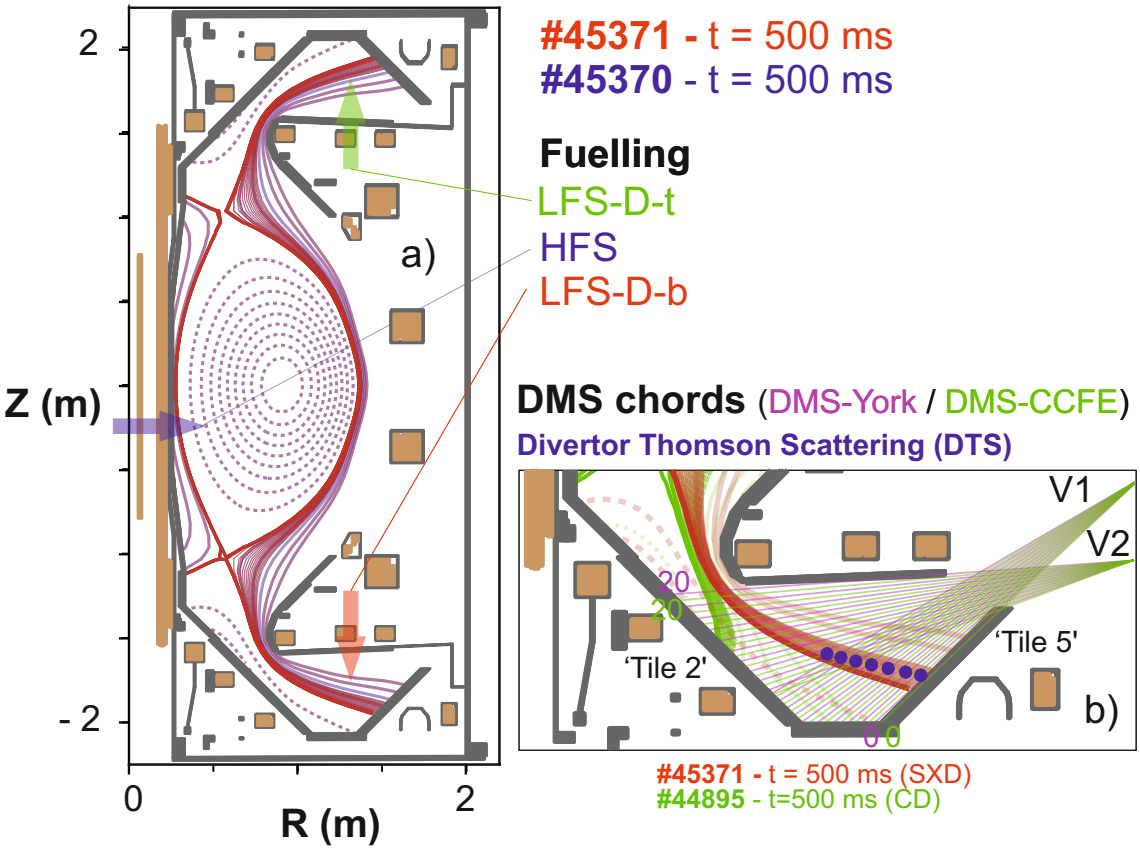

Figure 5.10: Geometry of DMS York (purple) and CCFE (green) spectrometers and divertor Thomson spatial points. LFS fuelling location (left) for 45371 indicated by red arrow. Figure courtesy of K Verhaegh (UKAEA) [15].

Using the DMS measurements a technique called Balmer Spectroscopy Plasma-Molecular Interactions (BaSPMI) [66] is applied to the MAST-U data. This technique allows electron density and temperature values to be inferred based on analysis of the Stark broadening and Fulcher band brightness respectively. For further detail on how the DMS spectrometers utilise the BaSPMI technique, the reader is directed to [15, 67–69]. To compare the BaSPMI analysis and the divertor Thomson measurements, the Thomson data was averaged across the spatial points within 25 cm of poloidal distance to the divertor target. For this plasma this is all of the Thomson spatial points. The DMS data was averaged for the points that fell within 30 cm of poloidal distance to the target. The comparison between the Thomson and inferred BaSPMI values can be seen in Figure 5.11.

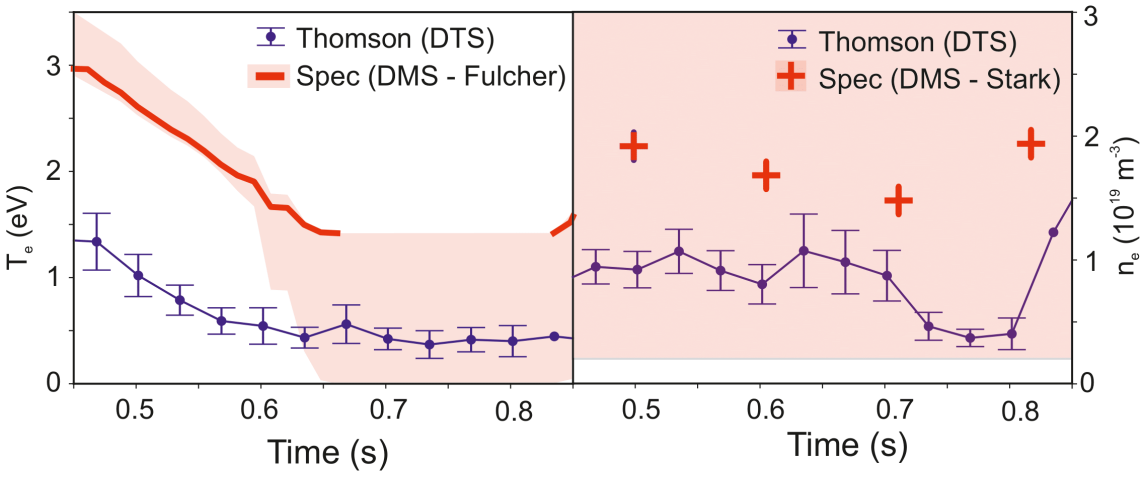

Figure 5.11: Temporal variation in divertor Thomson electron density (left) and temperature (right) values with Fulcher (left) and Stark (right) spectroscopy measurements for 45371. Figure courtesy of K Verhaegh (UKAEA) [15].

There is a qualitative agreement in the trend observed by both the divertor Thomson and DMS-Fulcher measurements which show the electron temperature decreasing over time. Even though the trend of the two measurements is in agreement, the absolute value of the electron temperature is not. This is because the BaSPMI analysis of the Fulcher band brightness has a lower detection limit of 1.3 eV which is indicated on Figure 5.11. In addition the line integrated nature of the measurement will result in a weighted measurement of the Fulcher emission at the hottest parts along the line of sight. Given that at such low electron temperatures close to the target, as indicated by the divertor Thomson, the Fulcher band will have receded from the target. As a result the disagreement in absolute value between these two systems is to be expected. Despite this, the agreement in the cooling of the divertor conditions over time is encouraging. The plasma being at a lower electron temperature than the Fulcher band detection limit as the degree of detachment increases with continued fuelling is a positive result. With the misalignment of the Thomson view to the strike leg it is expected that the local electron temperature at the divertor Thomson spatial points is even lower still. This inference is supported by the DMS measurements and the divertor Thomson reaching its own soft measurement limit, as seen in Figure 5.9.

There is a quantitative agreement between the divertor Thomson and the DMS-Stark measurements. This is due to the Stark inferred densities having large

uncertainty values (0.2-3 $\times 10^{19}\,\mathrm{m}^{-3}$). This is systematic due to the low electron density values leading to narrow Stark widths [15]. The use of a medium resolution grating to image the specific Balmer line required also impacted this value. This was required because of impurity emission in the divertor. There is also a qualitative agreement in the trend observed by the two measurements which show the electron density decreasing from 630 ms with increasing LFS gas fuelling as the divertor is detaching. Once the gas fuelling is stopped at 750 ms as seen in Figure 5.8, the density is seen to increase by both the divertor Thomson and DMS-Stark until the plasma ends at 900 ms. At this point the electron temperature does also increase but it is still very low and close to the soft detection limit of the Thomson system ($<$0.5 eV).

While there are limitations in the comparison between the two diagnostics, there is good qualitative agreement between the divertor Thomson and DMS-Fulcher and DMS-Stark measurements and quantitative agreement between the electron density measurements between the divertor Thomson and DMS-Stark. Comparison of these techniques showed that the divertor Thomson system is able to make measurements comparable to an established divertor diagnostic. It is able to observe sudden changes in the electron density and temperature profiles and the consequences of divertor detachment on these quantities, as a result of gas injection into the divertor chamber for a single MAST-U plasma. The commissioning of the 90 Hz laser for the divertor Thomson system in the future will enable measurements of this kind to be improved over those presented in this work as a result of tripling the temporal resolution.

5.5 Ultra Fast Divertor Spectroscopy Measurements

To further compare spectroscopy measurements with local Thomson measurements in the divertor, one of the divertor Thomson polychromators was adapted to measure the Fulcher band (600 nm), D_α (656 nm) and D_β (486 nm) lines. Due to digitisation space available at the time, these channels were measured in place of the existing Thomson channels meaning that electron density and temperature values from Thomson scattering at the same spatial location could not be produced. The

measured channels band pass the required wavelength and have strong rejection for light outside their pass band due to impurity emission in the divertor. The spatial point chosen for this polychromator was the furthest away from the divertor target as outlined in Table 3.1. This was chosen due to concerns surrounding low temperatures close to the target and the availability for comparison, particularly for detached plasmas and Fulcher band emission, which would limit analysis for the first implementation of this concept. The channels are digitised at 100 kHz and are integrated into the same hardware and data acquisition as the Thomson system. This ultra fast divertor spectrosopy (UFDS) unit was operational for a number of MAST-U plasmas but for this comparison MAST-U plasma 46860 was selected. There is good alignment to the strike leg of the divertor Thomson laser line so any affect on the local electron density and temperature measurements due to the distance from the strike leg is minimised. The plasma current, gas fuelling and core line integrated density can be seen in Figure 5.12. This plasma transitioned to Super-X at 300 ms and was fuelled from the LFS midplane with the fuelling ramped throughout the Super-X period until the end of the plasma at 800 ms. This plasma scenario was known to be close to the detachment threshold so with a large injection of gas into the SOL the divertor would be expected to detach within the Super-X period.

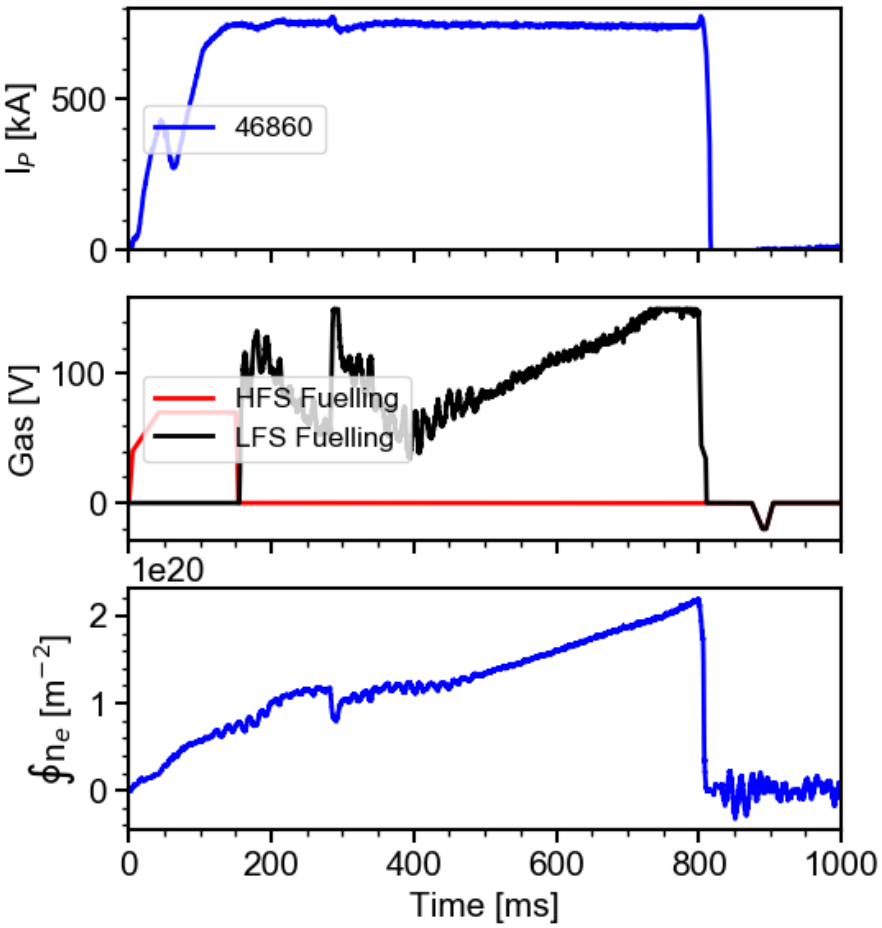

Figure 5.12: Plasma current (top), gas fuelling (middle) and core line integrated density (bottom) data traces for 46860

It can be seen in Figure 5.13 that as a result of the gas fuelling there is a steep rise in the core line integrated density. This corresponds to an increase in the neutral pressure in the core and divertor measured by their respective fast ionisation gauge (FIG). Beyond 450 ms there is a clear drop in the divertor temperature with the increase in fuelling. This temperature value is the average across the divertor Thomson spatial points so it is a good indicator of the macroscopic electron temperature of the divertor. At such low electron temperatures with minimal gradients previously observed across the spatial points, particularly in a detached state, taking an average of these spatial points is an appropriate method for monitoring the temporal change in electron temperature during a single plasma. The magnitude of the electron temperature observed during this time is indicative of detachment. As the electron temperature decreases so too does the emission from the Fulcher

band. This is expected because at these temperatures, during detachment, the Fulcher band will be receding from the divertor target towards the X-point. As the spatial location of this measurement of the Fulcher band emission is closer to the divertor entrance than the target, the drop in this emission is indicative of the Fulcher band receding towards the X-point, as expected. While the Fulcher band emission is observed to decrease, the D_β emission is observed to increase. This is an indicator of electron-ion recombination, particularly when D_β / D_α is increasing. This is a further indicator of divertor detachment. This indicator at sub-eV electron temperatures is routinely observed in MAST-U Super-X divertor plasmas by the two DMS systems.

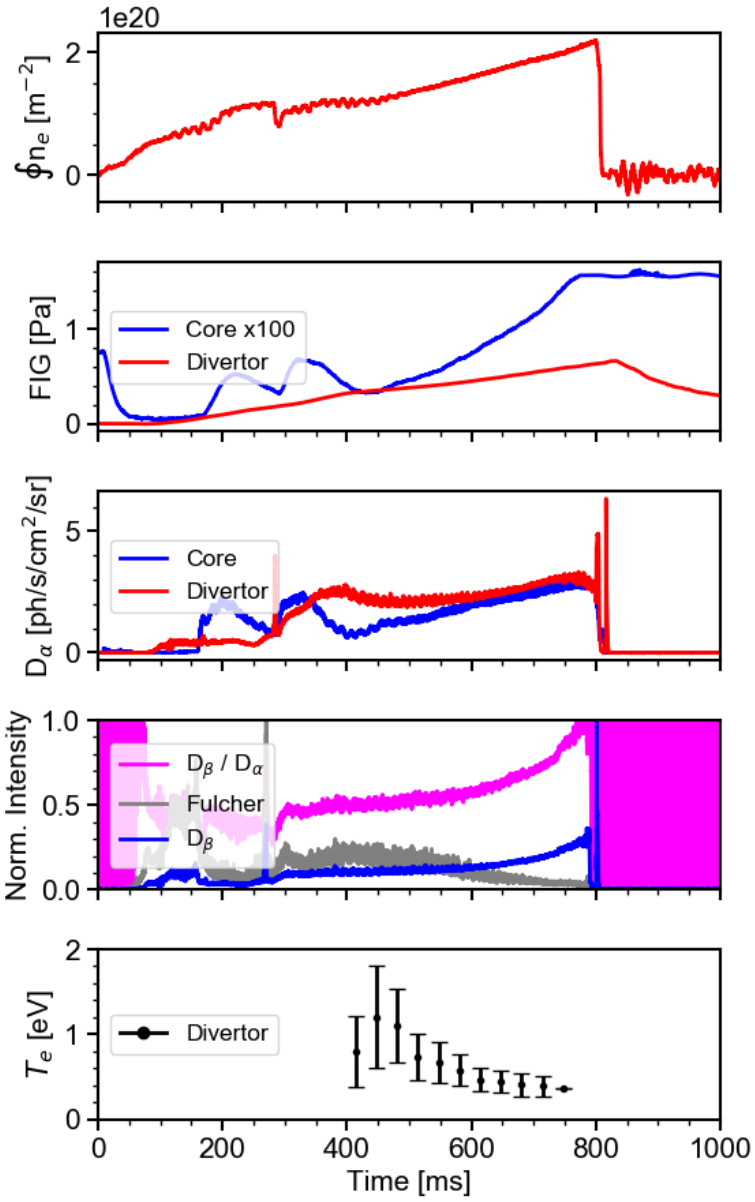

Figure 5.13: Core line integrated density (top), core and divertor neutral pressure (upper middle), core and divertor D_α emission (middle), Fulcher band and D_β emission (lower middle) and divertor electron temperature (bottom) for a gas ramp in MAST-U plasma 46860

To further analyse the relationship between the Fulcher band, D_α and D_β emission and the electron temperature, data from the closest Thomson spatial point was analysed for MAST-U plasma 46860. Figure 5.14 shows the Fulcher, D_α and D_β emission and the electron temperature values from 5.02 cm away in radial space. Given the detached divertor conditions and the magnitude of the electron temperature in this regime, there is expected to be a flat electron temperature profile so

a 5.02 cm radial difference is expected to have little impact on the electron temperature values despite the radial separation between these two spatial points. As expected based on the behaviour seen in Figure 5.13 there is a positive relationship between the electron temperature and the Fulcher band emission. It is observed that the Fulcher band emission measured as the electron temperature approaches 0.5 eV is negligible. Given the magnitude of the Fulcher band emission from plasma at electron temperatures in this plasma regime this is an expected result given the detached state of the divertor. In contrast there is an inverse relationship between the D_β and D_β / D_α emission and the electron temperature which expected given the trend observed in Figure 5.13. Given D_β / D_α emission is an indicator of electron-ion recombination, which is itself used by diagnostics such as DMS to indicate divertor detachment, it is expected that there is an inverse relationship with electron temperature.

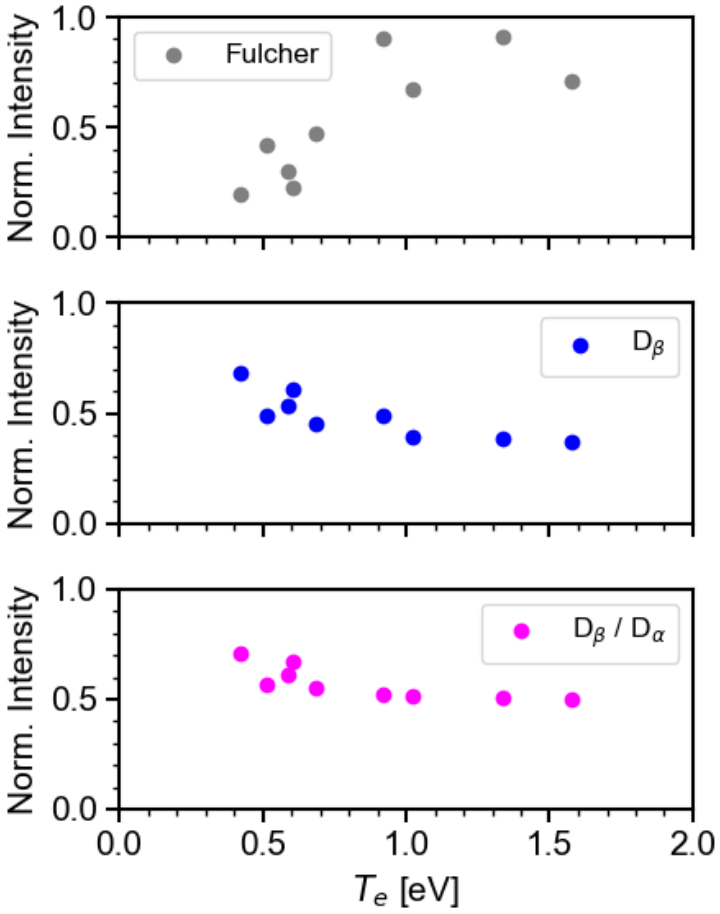

Figure 5.14: Normalised Fulcher band (top), D_β (middle) and D_β / D_α (bottom) emission with electron temperature measurements from nearest divertor Thomson spatial point (ΔR = 5.02 cm) for MAST-U plasma 46860

The observation of the Fulcher band, D_β and D_β / D_α emission and their respective relationships with the electron temperature are a first of its kind measurement in the Super-X divertor. Positive first results from this system has resulted in plans to expand the number of these UFDS measurements for future MAST-U experiments. With dedicated implementation of these channels there is the ability to design new divertor Thomson polychromators with these channels inbuilt to enable ultra fast spectroscopic measurements to be made with local electron density and temperature measurements at the same spatial location.

As a lower cost alternative if no further divertor Thomson polychromators are commissioned, bespoke UFDS units can be installed directly next to the existing Thomson spatial points. This is easily done given the space available to expand the

number of polychromators in the divertor Thomson collection cell backplane, as discussed in subsection 3.2.4. This would provide electron density and temperature measurements within a few millimetres of the spectroscopy measurements. These bespoke polychromators also allow channels measuring entirely different emission bands to be installed. These can even be installed in different spatial locations with the flexibility provided by the collection cell backplane. Given the success of these first results it would be of interest to consider installing one of the UFDS units close to the divertor target to further study the relationship between the spectral emission and local electron density and temperature measurements in the Super-X divertor. With the temporal resolution this system is able to operate at there is potential to use these measurements for measurements during ELM crashes and real time control in the future.

5.6 Edge Fall-off Averaging

The core Thomson scattering system can be used for electron measurements into the scrape-off layer (SOL). This facilitates the study of the pedestal structure and other plasma phenomena at the edge of the tokamak [26]. One method of reducing error in these measurements is averaging across multiple profiles. Averaging of density and temperature profiles works under the assumption that there is no change in plasma position or electron density and temperature over the time period chosen. Presence of phenomena such as ELMs and NTMs can invalidate these assumptions.

It is typically possible to measure down to electron densities of $\sim 5 \times 10^{18}\,\mathrm{m}^{-3}$ in the midplane SOL for a single laser pulse. Fitting anomalies to the scattered signal and the Selden function [46] are much more common at the plasma edge. These signals are limited by the noise floor and in particular for this system, the digitiser noise. The anomalies can even result in undefined values at the extremes of the plasma which makes averaging of the electron density and temperature profiles an unrealistic representation of this region of the plasma.

An averaging technique is applied to scattered signals over multiple laser pulses to allow measurements to electron densities of $\sim 1 \times 10^{18}\,\mathrm{m}^{-3}$, much lower than that

of a single laser pulse. This averaging reduces the background noise level by $N^{1/2}$ where N is the number of laser pulses used. The effect of this averaging can be seen in the reduction of the background noise level in Figure 5.15.

In Table 5.2 the integrated signal value and its associated error are shown for a single and averaged data trace. The effect of this averaging on the density and temperature values, produced from a fit to the Selden function, are also shown in Table 5.3. The results in these tables show a reduction in the error for the integrated signal in each channel and the resulting electron density and temperature values respectively when applying the averaging technique.

Profile	**C1** (nVs)	**C2** (nVs)	**C3** (nVs)
Single	0.173 ± 0.012	0.108 ± 0.009	0.000 ± 0.027
Averaged	0.194 ± 0.004	0.083 ± 0.004	0.000 ± 0.008

Table 5.2: Core Thomson polychromator 424 signal values for respective channels in 5.15

Profile	$\mathbf{n}_e$ (10^{18} $\mathbf{m}^{-3}$)	$\mathbf{T}_e$ (eV)
Single	5.82 ± 0.019	12.23 ± 5.649
Averaged	5.57 ± 0.003	12.95 ± 0.014

Table 5.3: Core Thomson polychromator 424 electron density and temperature values in 5.15

Results of this technique were used to compare with other diagnostics operating in the SOL. At the plasma edge reciprocating probes are often used. They are especially useful for determining the power fall-off in the SOL which is a key measurement for divertor survivability. Ohmic L-mode data, shown in Table 5.4, was analysed for the final MAST campaign where the reciprocating Mach probe was operational.

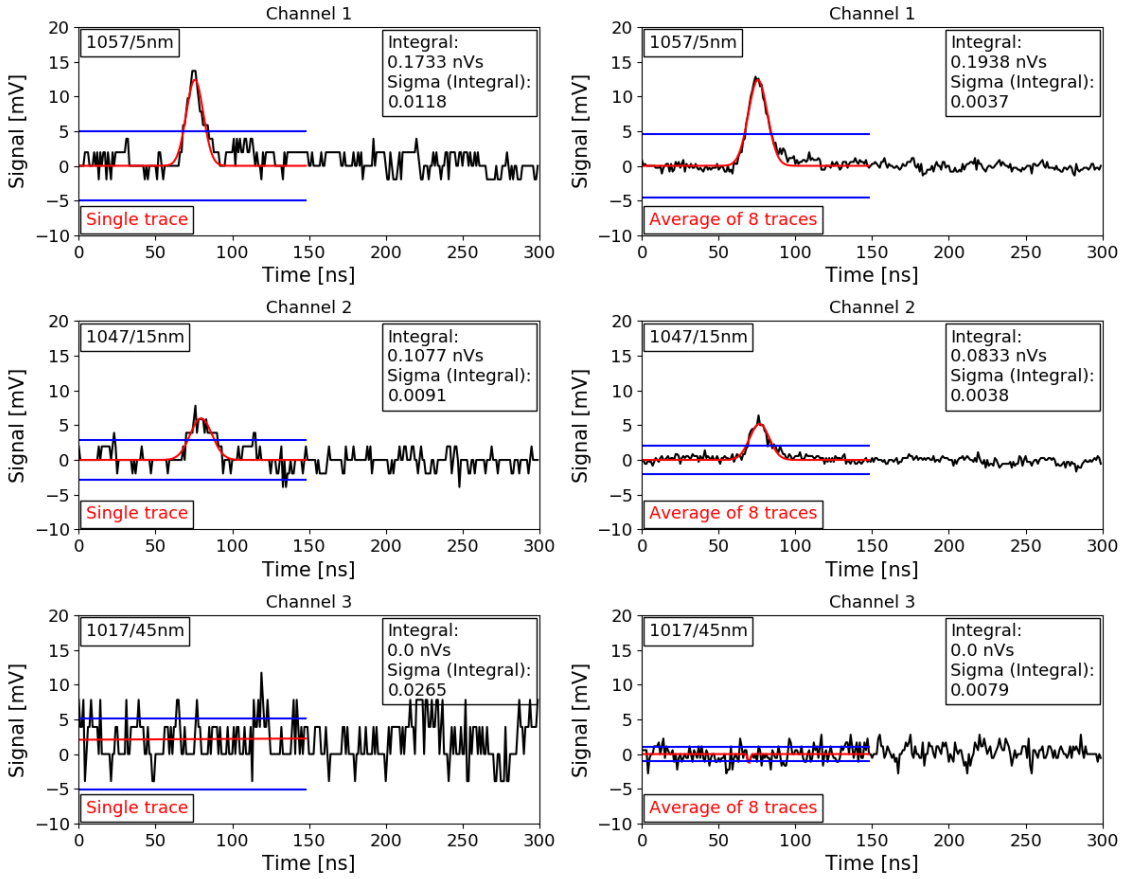

Figure 5.15: Core Thomson polychromator 424 signal trace for hot 29023 showing the first three channels at 0.29s (left) and averaged for 0.27-0.30 s (right). Horizontal blue lines demonstrate standard deviation in the background signal outside of the fitted Gaussian.

Shot	Plasma current (kA)	Toroidal field (T)	$\overline{n}_e$ (m^{-3})
29003	400	0.585	2.20×10^{19}
28996	400	0.585	1.30×10^{19}
29007	600	0.585	2.20×10^{19}
28998	600	0.585	1.30×10^{19}
29018	400	0.400	2.20×10^{19}
29027	400	0.400	1.65×10^{19}

Table 5.4: Physics and engineering parameters used during MAST reciprocating probe experiment

On MAST the Mach probe made direct measurements of the ion saturation current and did not produce electron density measurements. To enable comparison between the two diagnostics the Thomson measurements were converted into an ion saturation current:

$$I_{sat} = e n_e C_s = e n_e c \sqrt{T_e / m_e} \tag{5.6.1}$$

where e is the charge of an electron, n_e is the electron density, C_s is the speed of sound, c is the speed of light, T_e is the electron temperature and m_e is the electron mass.

Plasma shots 29003 and 28996 were used as the reference case with $B_T = 0.585\,\mathrm{T}$ and $I_p = 400\,\mathrm{kA}$. These shots were taken from a range of MAST experiments varying the line averaged density through control of deuterium gas injection. The core line averaged density was controlled during the flat top phase of the pulse between three separate values. Low (L), intermediate (I) and high (H) core line averaged densities of $\overline{n}_e \approx [1.30, 1.65, 2.20] \times 10^{19}\,\mathrm{m}^{-3}$ respectively were chosen. Low magnetic field ($B_T = 0.400\,\mathrm{T}$) and high current ($I_p = 600\,\mathrm{kA}$) were chosen as the other two cases which can be seen in Figure 5.16.

The region available for comparison is limited by the radial depth of the probe penetration, in the time period of its sweep, to an area close to the separatrix. The intermediate density profiles were omitted from the high current data due to the probe reciprocation not crossing the separatrix during its sweep. The intermediate density for the reference was excluded but there was no low density case for the

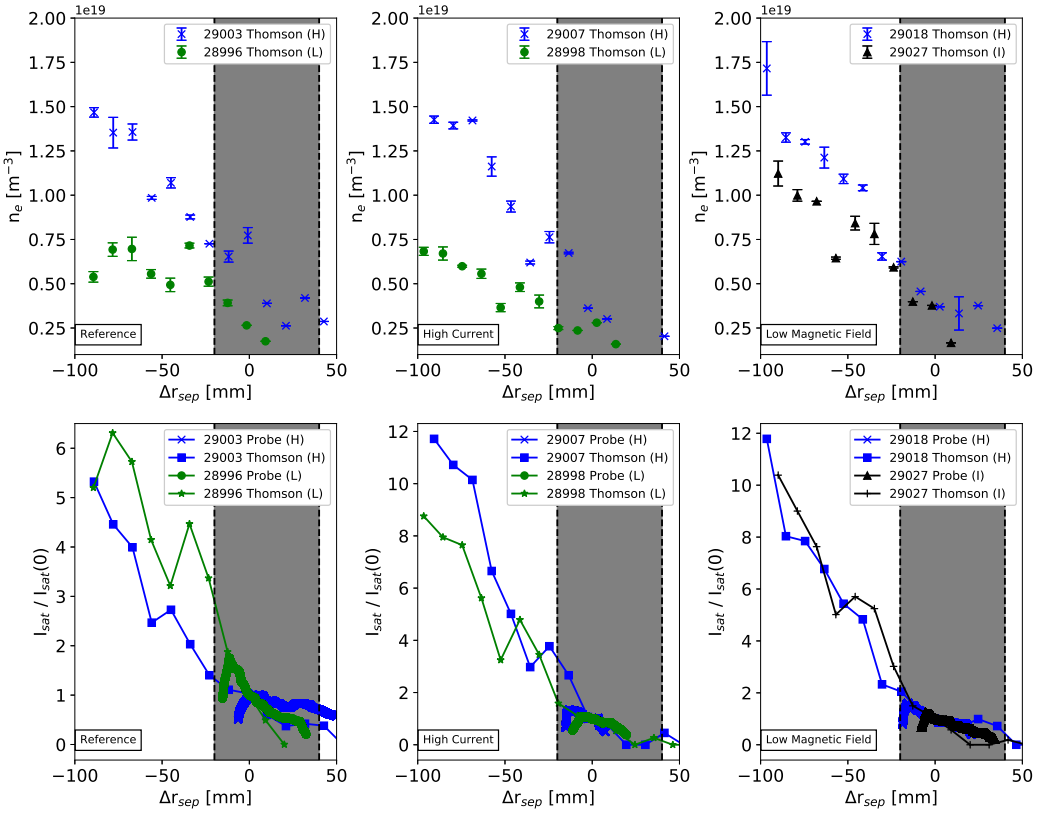

Figure 5.16: Thomson density profiles (top) and Mach probe and Thomson I_{sat} profiles (bottom) normalised by their separatrix value with all data from 0.25-0.30 s. Ion saturation values are normalised by the value at the separatrix position for each diagnostic respectively.

low magnetic field so an intermediate density was included instead.

The probe profiles were smoothed with a 15 ms window size convolution. Figure 5.16 shows Thomson profiles deep into the SOL measuring densities down to $\sim 1\times10^{18}\,\mathrm{m}^{-3}$, where 12 laser pulses were used to produce the averaged data. When measuring the ion saturation current with the Mach probe, error values of 15% or more are typically observed [70]. Considering the ion saturation current data within the sweep of the probe there is a good agreement between the Mach probe and the Thomson averaging for the ion saturation values, normalised to their separatrix value, in Figure 5.16. This shows the suitability of the Thomson diagnostic for SOL measurements and comparison with probe and other edge diagnostics, especially when implementing this averaging technique.

Power fall-off in the scrape-off layer was investigated using a similar processing

technique previously [70]. As this technique was tested on MAST data, future experiments were planned on MAST-U to continue these comparisons with the addition of infrared camera data to further investigate the power fall-off length. Unfortunately due to the unavailability of the reciprocating probe due to delays in its installation and commissioning on MAST-U these experiments were postponed until subsequent campaigns. This meant that they fell outside the time frame of the work in this thesis.

Despite this, a method of improving the quality of the Thomson scattering data in the scrape-off layer has been developed. This has shown to be effective at reducing the systematic noise level in the signal. Ion saturation current values converted from Thomson scattering data show good agreement with reciprocating Mach probe data in the SOL. Through control of uncertainties and measurement of electron densities on the order of $\sim 1 \times 10^{18}\,\mathrm{m}^{-3}$, the technique has shown its suitability for analysis of the MAST-U scrape-off layer. This is a significant improvement on previous analysis methods which due to system limitations at the plasma extremes, meant that data in the deep SOL from Thomson systems was not typically used without significant processing or unrealistic physical assumptions.

Chapter 6

Summary and Outlook

6.1 Summary

In the work carried out in support of this thesis the development, installation and operation of the MAST-U divertor Thomson scattering system has been presented. This has enabled new divertor analysis to be carried out in support of MAST-U with the ability to measure the electron density and temperature along the divertor strike leg. Successful operation of this system has led to a number of publications by the author both as a lead investigator and as a co-author. The work discussed in this thesis this has centred around the MAST-U tokamak and the development of plasma diagnostic techniques and analysis of data from MAST-U plasmas. This has mainly been as part of edge and exhaust experiments. Other contributions to the field were made in the topic areas of pedestal physics and development of polarimetric Thomson scattering measurements in high temperature JET D-T plasmas which were not relevant to the core body of work discussed in this thesis.

In Chapter 3 the MAST-U divertor Thomson scattering system is introduced. Integration of the divertor Thomson system with the existing core Thomson system is outlined. This enables parallel measurements of the electron density and temperature profiles in two areas of the MAST-U tokamak which are discussed in Chapter 5. Simulations and laser fluence testing of the in-vacuum laser mirror and focusing lens were carried out which showed that the mirror coating selected was expected to sustain the laser load from a MAST-U physics campaign in the optical setup chosen. This was shown to be correct during commissioning and operation

during the campaign and it continues to be operating without issue beyond the work carried out during this thesis.

The development of the low temperature polychromators and the modifications made to facilitate low electron temperature measurements in the Super-X divertor are presented. It was found that the inclusion of a 1061/2 nm filter was crucial to enabling electron temperature measurements below the limit of the previous generation of polychromator. Furthermore the reduction in the angle of incidence of this filter from 94.5° to 90° was found to have an impact on the quality of sub-eV electron temperature measurement in the Super-X divertor. This is supported by simulations which show a clear reduction in the fractional error for electron temperature measurements below 5 eV with this adjustment.

Simulations were carried out to test the addition of a 1067/2 nm filter to improve the sub-eV measurements of the divertor Thomson system. This was shown to reduce the fractional error that would be measured by the system and as a result this is being considered as a future improvement for the system in light of lower than expected electron temperatures in the Super-X divertor. Measurements of the plasma background emission while the Thomson laser was not firing were performed. These showed that there was a radial and spectral variation in the emission measured that did not scale with the filter bandwidth. Specific line emission governed by fluctuations in the electron temperatures is evidently being picked up in specific wavelength channels.

In Chapter 4 the process of calibrating the divertor Thomson scattering polychromators is outlined. A discussion on Rayleigh and Raman scattering and the rationale behind the use of Raman scattering for calibration of the MAST-U Thomson systems is covered. Parallel calibration of the core and divertor Thomson system allowed comparison between the two diagnostics. The divertor system showed a good signal level which was repeatable over 1 s (33 laser pulses) of data acquisition. This behaviour was observed to scale linearly with pressure with ∼5% error due to fluctuations in the laser energy. There was negligible stray light observed during the calibration and when accounting for the difference in laser energy and vignetting the signal level between the two systems compares favourably. With dedicated alignment of the collection cell to the laser line, the sensitivity of the

fibre backplane position was investigated. Good backplane alignment of the bifurcated fibres was observed which led to a good signal level being measured at each of the 12 spatial points across the viewing chord. Once all of the 12 spatial points had been commissioned during Raman scattering this allowed the vignetting curve of the collection cell to be measured and accounted for with the Raman calibration. Successful Raman calibration of this system in Nitrogen was crucial to its commissioning and it has facilitated high quality electron density measurements in the Super-X divertor which are presented in Chapter 5.

In Chapter 5 the main body of results from MAST-U plasma experiments is presented. The divertor Thomson system made the first electron density and temperature measurements along the Super-X divertor strike leg. The electron density and temperature parameter space of the Super-X divertor was measured over the course of 68 plasmas. Electron density values were typically in the region of $1 \times 10^{19}\,\mathrm{m}^{-3}$ and electron temperature values typically in the region of 1 eV which was in contrast to the values predicted by simulations previously which predicted 1.1 eV [65]. Despite the value predicted in these simulations agreeing with the values measured experimentally, there are a number of physical differences which would explain a discrepancy between the two values. The magnetic geometry in the simulated Super-X is different to that achieved experimentally, particularly in terms of the magnetic flux expansion. There is also a far higher concentration of neutrals in the plasma, crucially with these levels not controlled by the cryopump, as in the simulations. If these conditions were put into the model in [65] it is expected that they would predict higher temperatures than those measured by the divertor Thomson scattering system.

There was observed to be little change in the distribution in the parameter space between plasmas operating with 600 kA and 750 kA plasma current. Over the course of the 68 plasmas profiled there were differences in the magnetic geometry and the alignment of the strike leg with the divertor Thomson laser line. It was observed that while there was a difference in the electron density and temperature measured away from the strike leg, the impact of this was not as significant as expected. The electron density and temperature values measured were still typically in the region of $1 \times 10^{19}\,\mathrm{m}^{-3}$ and $\sim$1 eV respectively. This was due to the

lower than expected electron density and temperature values across the Super-X chamber and the lack of any significant gradient in the profiles, particularly in the case of detached plasmas.

The effect of divertor detachment was observed in the electron density measurements in the divertor. A rollover was seen in this data when analysing divertor Thomson scattering data. There was a good agreement between the Langmuir probe ion saturation measurements and the divertor Thomson measurements for the electron density at which the rollover was observed which was $\sim 7 \times 10^{19}\,\mathrm{m}^{-2}$ in line integrated density. There was also good agreement in the values for attached ($4 \times 10^{19}\,\mathrm{m}^{-2}$) and detached ($1.2 \times 10^{20}\,\mathrm{m}^{-2}$) plasma conditions as indicated by the rollover in the ion saturation current measurements. This was in contrast to the effect seen on the electron density at the midplane SOL as measured by the core Thomson system, which continued to increase with the core line integrated density. In contrast the electron temperature measurements made by both Thomson systems demonstrated identical behaviour during the detachment phase where a monotonic decrease was seen.

The effect of a ramp in the gas fuelling on the electron density and temperature profiles was investigated. This showed good agreement with the behaviour seen in other detachment experiments where the density increased until the point of rollover before dropping with further increases in upstream density. The electron temperature meanwhile decreased monotonically throughout the gas ramp as the divertor became more detached until around 0.5 eV where the soft detection limit of the divertor Thomson system restricted the measurements. These measurements were compared to the divertor monitoring spectrometer (DMS) systems which were operational during the same plasma. Electron density and temperature values inferred from Balmer Spectroscopy Plasma-Molecular Interactions (BaSPMI) analysis agreed favourably with the divertor Thomson measurements within the bounds of their error in this regime. Electron density values dropped from $\sim 1 \times 10^{19}\,\mathrm{m}^{-3}$ around detachment onset and dropped to below $\sim 5 \times 10^{18}\,\mathrm{m}^{-3}$ at the end of the fuelling ramp when the plasma was at its most detached. Meanwhile the electron temperature dropped from ~ 1.5 eV at the detachment onset down below 0.5 eV before Thomson scattering signal was no longer being transmitted, particularly at

spatial points closer to the target.

For a series of plasmas a divertor Thomson polychromator was replaced with 100 kHz measurements of D_β (486 nm), Fulcher band (600 nm) and D_α (656 nm) emission. Emission from the Fulcher band was shown to have a positive correlation with electron temperature up to the 1.5 eV peak temperatures observed in the Super-X chamber during this plasma. However D_β and D_β / D_α emission was shown to have a negative correlation with electron temperature from 0.75 eV at which point the emission was observed to increase with decreasing electron temperature. This data showed good agreement based on previous results and indications from the D_β and D_β / D_α emission of electron-ion recombination were observed during a detached plasma. This is a positive outcome for first results from this system with more of these polychromators planned to be implemented for future MAST-U experiments.

Prior to the start of MAST-U experiments an averaging technique was developed to allow measurements down to electron densities of $\sim 1 \times 10^{18}\,\mathrm{m}^{-3}$ in the SOL with the core Thomson scattering system. This allows measurements below the noise floor of the diagnostic by averaging the scattered signals and using the result of the averaged signals to produce electron density and temperature values. This technique was shown to reduce the background noise level and the minimum electron density measurable by the system by several factors. This technique was tested on a series of plasmas and the Thomson measurements, converted to ion saturation values for comparison, showed good agreement with reciprocating Mach probe measurements surrounding the separatrix.

As a result of the work carried out in support of this thesis there has been a number of techniques implemented that will impact the development of Thomson scattering systems in the future. The MAST-U divertor Thomson system has shown that in-vessel optics can be used to create a unique scattering geometry to suit the needs of the tokamak. The use of in-vessel optics will be affected in future tokamaks such as ITER operating with a D-T fuel mix where the resulting neutron fluxes will significantly affect the use of traditional optical coatings. Despite this, this work has shown that tokamaks operating outside of this bespoke fuelling scenario, only currently permitted by JET and ITER in the future, will be able to exploit a

similar technique.

This work has shown that sub-eV electron temperatures can be measured with a filter based polychromator in a high stray light region such as the baffled Super-X divertor. Implementation of OD6 light rejection filters and a filter transmissive to the laser wavelength facilitated this. Through comparison of stray light levels between a core and divertor Thomson polychromator in Section 3.3, in a spatial location that picks up significant stray light from the centre column, the effect of these mitigation techniques is demonstrated. Stray light mitigation will be extremely important for Thomson systems on tokamaks operating with metal divertor tiles and the development of advanced plasma scenarios. Metal divertor tiles will result in increased reflectivity and produce additional sources of stray light. Results from this work have shown the ability of this design to mitigate these effects over previous generations of hardware.

6.2 Future Work

Based on the work carried out during this thesis a few suggestions for future work are given below.

With the X-point Thomson scattering system due for installation and commissioning in the near future, integration of this system with the core and divertor Thomson system would enable further study into detachment access in the Super-X divertor, particularly with the electron density and temperature measurements in this area of the plasma which have not been produced from a Thomson scattering system before. The inclusion of this data into analyses such as that presented in Section 5.3 would be a significant improvement. It would also allow comparison between the Thomson measurements and the MAST-U bolometry systems [71, 72] and measurement of electron density and temperature fluctuations around the X-point during detachment.

The results presented in Chapter 5 showed that the electron density and temperature parameter space of the Super-X divertor was lower than predicted by simulations. The interference filters for the divertor Thomson system were chosen based on the assumption that the electron temperature, particularly in attached

plasmas, would be higher than the few eV measured. Including the 1067/2 nm filter, as discussed in Section 3.3, would improve the fractional error of the current polychromator configuration for measurements below 5 eV based on the simulations performed.

While it could be justified that improving the electron temperature range below ∼0.5 eV would be more beneficial, there is a limit to how narrow a bandwidth filter can be used in these polychromators based on the cone angle of the filters which is ±2°. This means that it would be difficult to implement a filter much closer to the laser wavelength than the 1061/2 nm filter is currently. With further MAST-U enhancements such as the divertor GDC and the cryopump in future plasmas, the electron density and temperature parameter space of the Super-X divertor is expected to increase, particularly in attached divertor plasmas. In the case that the divertor conditions do not improve, the inclusion of the 1067/2 nm filter, while not improving the electron temperature range of the system, would increase the number of captured photons and still provide a clear improvement in the sub eV measurements which will be beneficial during detachment regardless.

First results from the ultra fast divertor spectroscopy system are presented in Section 5.4. The Fulcher band, D_β and D_β / D_α emission were compared to electron temperature measurements from the divertor Thomson system and showed good agreement. Integration of this system with Thomson channels would allow electron density and temperature measurements to be made at the same spatial point to improve the understanding of the atomic and molecular processes influencing detachment access. In addition, the ability to add to the number of these units and place them along the viewing chord and sample along the strike leg would be of great benefit. Given the 100 kHz temporal resolution there is the potential to integrate these measurements into the MAST-U plasma control system [73] for real-time detachment control in the Super-X divertor which is far beyond the capability of any current tokamak.

Given the ability to run the core and divertor Thomson systems in parallel, this enables the study of ELM burn through from the SOL to the Super-X divertor. By putting the Thomson system into burst mode [48] the firing of the Thomson lasers can be separated by as little as 10 μs. This would allow the propagation of an ELM

to be tracked from the SOL and into the divertor with sufficiently small spacing between the time of the lasers firing. With a D_α filtered camera already measuring in the divertor, a type I ELM would clearly be visible in the divertor. The effect this has on the electron density and temperature of the divertor plasma is of great interest for the operation of next generation tokamaks, particularly those operating with advanced divertor configurations such as the Super-X. If these experiments were carried out with the ultra fast divertor spectroscopy system also operating it would allow further study into the atomic and molecular processes surrounding an ELM.

Appendix A

Raman Spectrum

The total Raman cross section measured by a given filter σ_{Raman} can be calculated based on the contribution of the Raman line intensities σ_{Raman}(J) and filter transmission $T(\lambda_{J)}$ at each wavelength for each rotational state J within the pass band of that filter [58]:

$$\Sigma\sigma_{Raman}(J)T(\lambda_J) \tag{A.1}$$

The intensity of Raman lines can be calculated from the fraction of molecules in each state $F(J)$ and their differential cross section $S(J)$:

$$\sigma_{Raman}(J) = F(J)S(J) \tag{A.2}$$

where the fraction of molecules in the state J is dependent on their rotation energy $E(J)$ and their nuclear spin statistical weight $g(J)$ such that:

$$F(J) = \frac{1}{Q}g(J)(2J+1)\exp\left(\frac{-E(J)}{k_B T_{gas}}\right) \tag{A.3}$$

$$g(J) = 6 \text{ for even } J \text{ in Nitrogen}$$
$$g(J) = 3 \text{ for odd } J \text{ in Nitrogen}$$

where k_B is the Boltzmann constant and T_{gas} is the gas temperature, measured as 294 K given the in-vessel and the gas achieving a thermal equilibrium overnight before the calibration was run.

$$E(J) = hc\left(B_0(J(J+1)) - D_0(J(J+1))^2 + H_0(J(J+1))^3\right) \tag{A.4}$$

where h is Plancks constant, c is the speed of light and the remaining constants are listed in Table A.1.

The differential cross section for anti-Stokes lines, given the wavelengths of concern during this calibration, making the transition $J \rightarrow J+2$ are given by:

$$S(J) = \sigma_{J \rightarrow J'} \times s(J) \tag{A.5}$$

$$s(J) = \frac{3J(J-1)}{2(2J+1)(2J-1)} \tag{A.6}$$

$$\sigma_{J \rightarrow J'} = \frac{7}{45}(2\pi^4)\left(\frac{\gamma}{\lambda_J^2}\right)^2 \tag{A.7}$$

Symbol	**Value**
B_0	$198.95\,\mathrm{m}^{-1}$
D_0	$5.72 \times 10^{-4}\,\mathrm{m}^{-1}$
H_0	$3.70 \times 10^{-10}\,\mathrm{m}^{-1}$
γ^2	$0.50 \times 10^{-60}\,\mathrm{m}^6$
Q	464.311

Table A.1: Raman constants for Nitrogen as used in Equation A.4 from [58] with the exception of γ^2 which is from [59]

Appendix B

Images of Divertor Thomson Scattering System Optics

The images in this appendix are from various stages along the beam path of the divertor Thomson system ranging from where the beam path splits from the other lasers in the core system through to where the alignment of the system is tested as in the pit below the MAST-U vessel. The layout of the cubicle containing these optics can be seen in Figure 3.4. The images were captured during optical alignment with a series of low power HeNe lasers attached to the optical path of each laser to aid in alignment of the invisible Nd:YAG lasers.

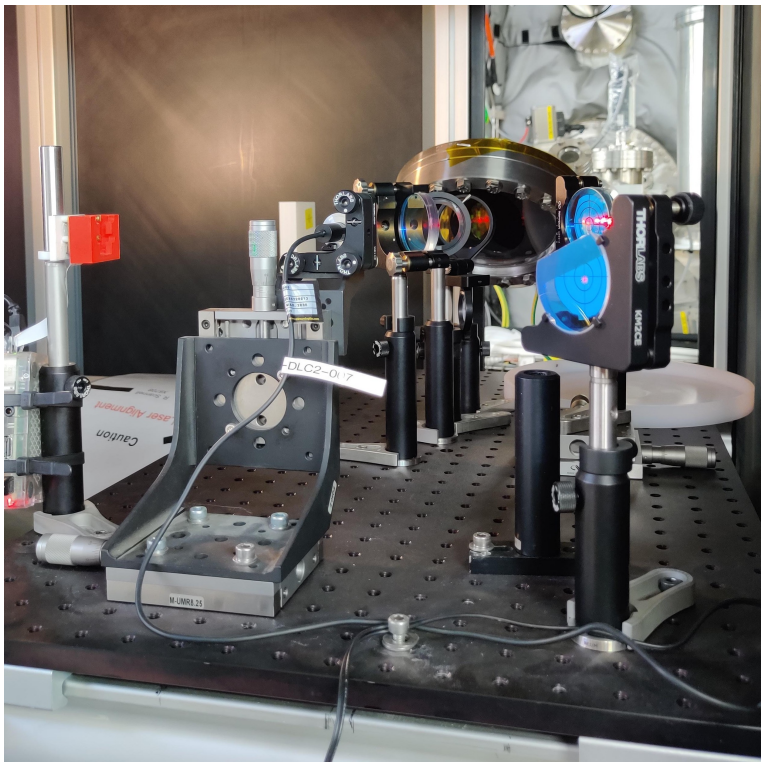

Figure B.1: D-shaped mirror inside Thomson scattering optics cubicle. Divertor laser spot can be seen on first mirror with remaining core lasers passing over the top. Red viewing camera (LHS) is used to check and adjust alignment in the locked tokamak hall.

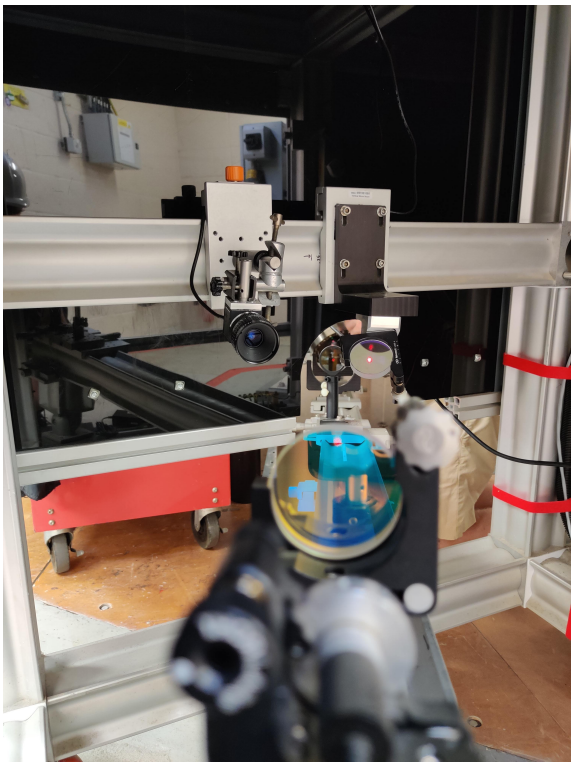

Figure B.2: A view of the zero degree mirror that rotates the beam polarisation (centre) and final mirror (bottom) that reflects the beam towards the focusing lens and Brewster window. Alignment camera (left centre) used to monitor and adjust the alignment in the locked tokamak hall. HeNe diode behind the final mirror is used to align the lasers in the pit below the vessel.

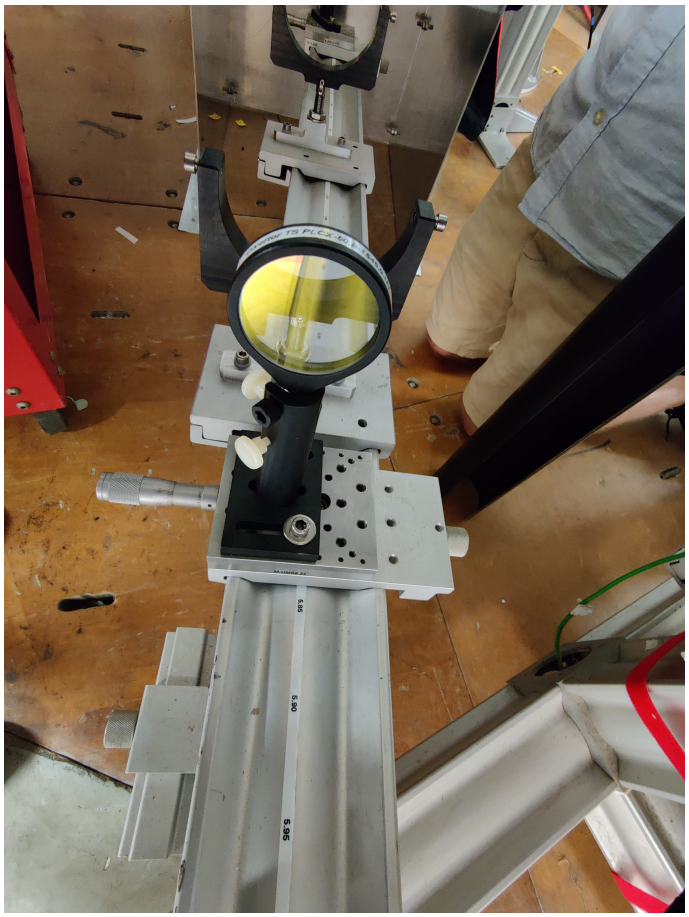

Figure B.3: 3.41 m focal length lens used to focus the laser into the scattering region in the lower Super-X null. Image taken of the lens in position as described in subsection 3.2.1.

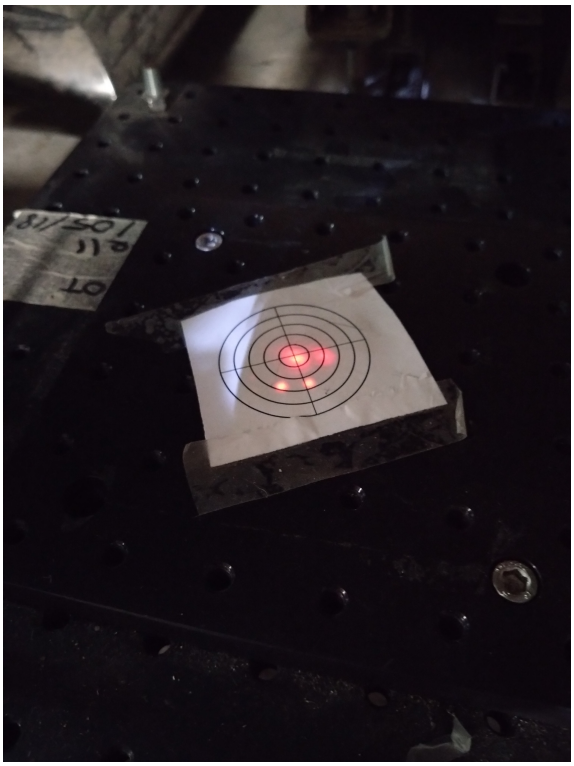

Figure B.4: Alignment of two HeNe diodes centred on the target in the pit below the MAST-U vessel. Bright central spot is from the laser room and the fainter spot is from behind the final mirror seen in Figure B.2 to check co-alignment. Laser spots below the central target are a back reflection from a mirror surface within the optical system.

Appendix C

Laser Beam Focussing Simulations

The images in this appendix are from simulations of the laser beam focusing as described in subsection 3.2.1. A graphical representation of these simulations with the quantitative results of mirror loading and the alignment margin listed on the images. There were four lens to Brewster window distances simulated during this work, which were 0 m, 0.5 m, 1.0 m and 1.5 m. The results of these simulations can be seen below.

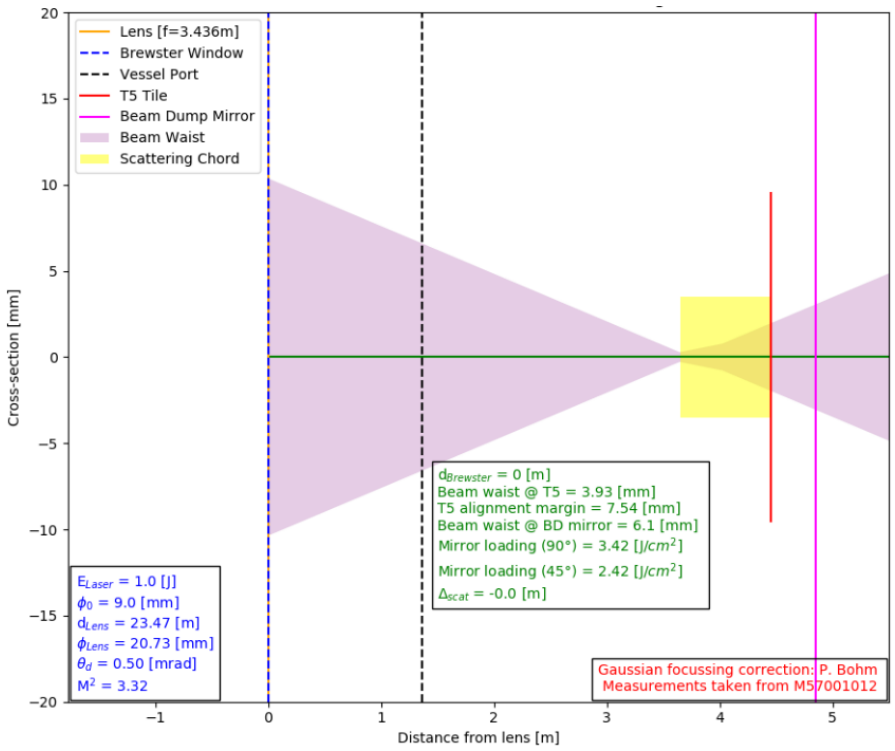

Figure C.1: Simulation of the laser beam focusing as described in subsection 3.2.1 with the lens positioned at the Brewster window

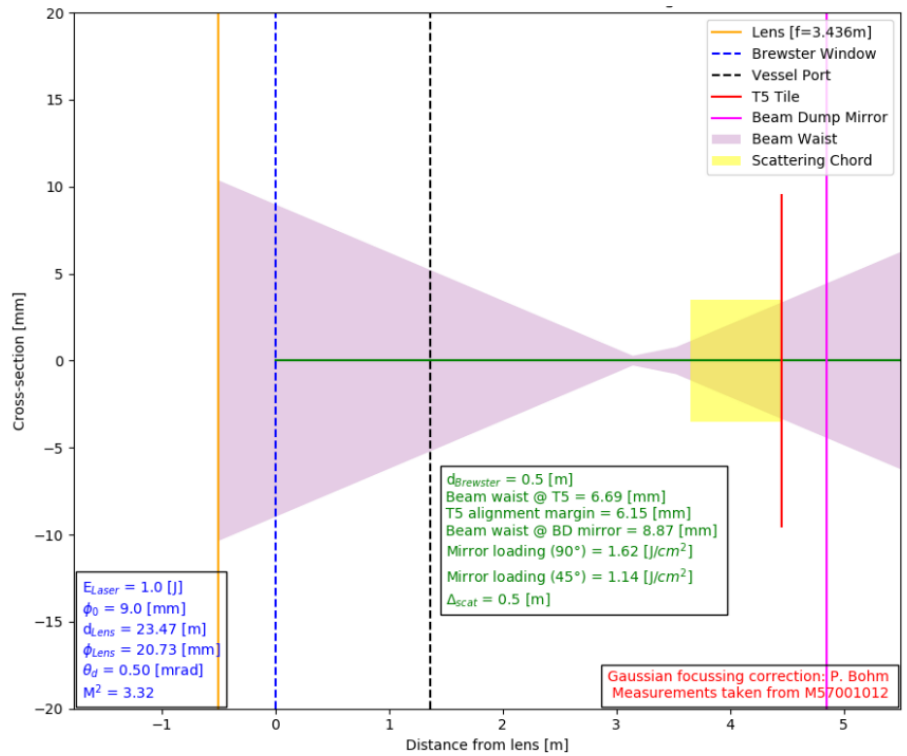

Figure C.2: Simulation of the laser beam focusing as described in subsection 3.2.1 with the lens positioned 0.5 m from the Brewster window

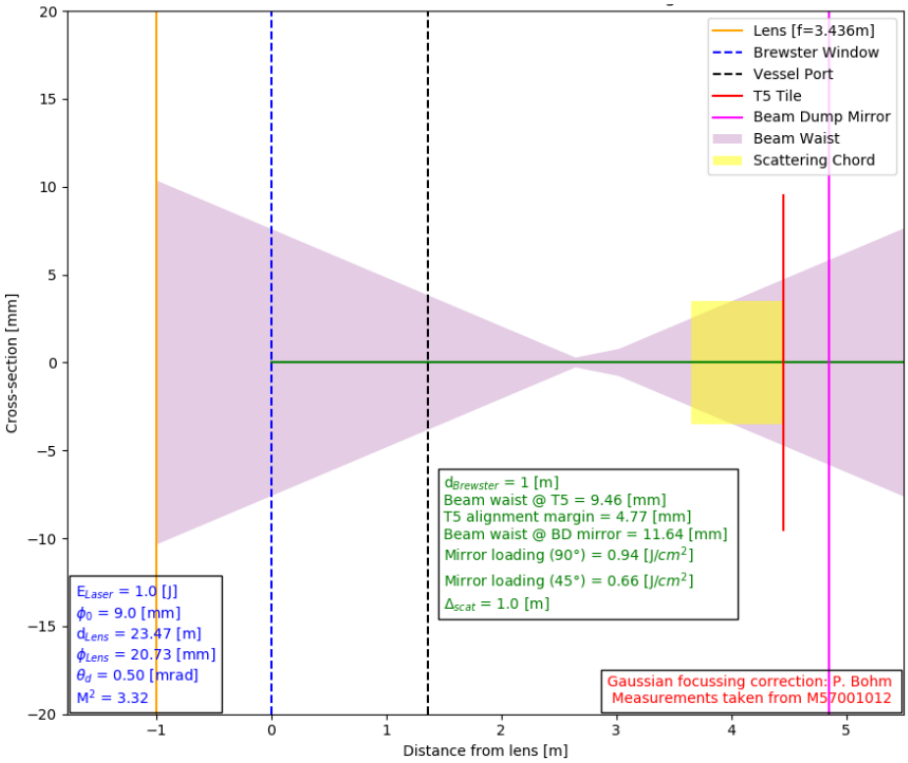

Figure C.3: Simulation of the laser beam focusing as described in subsection 3.2.1 with the lens positioned 1.0 m from the Brewster window

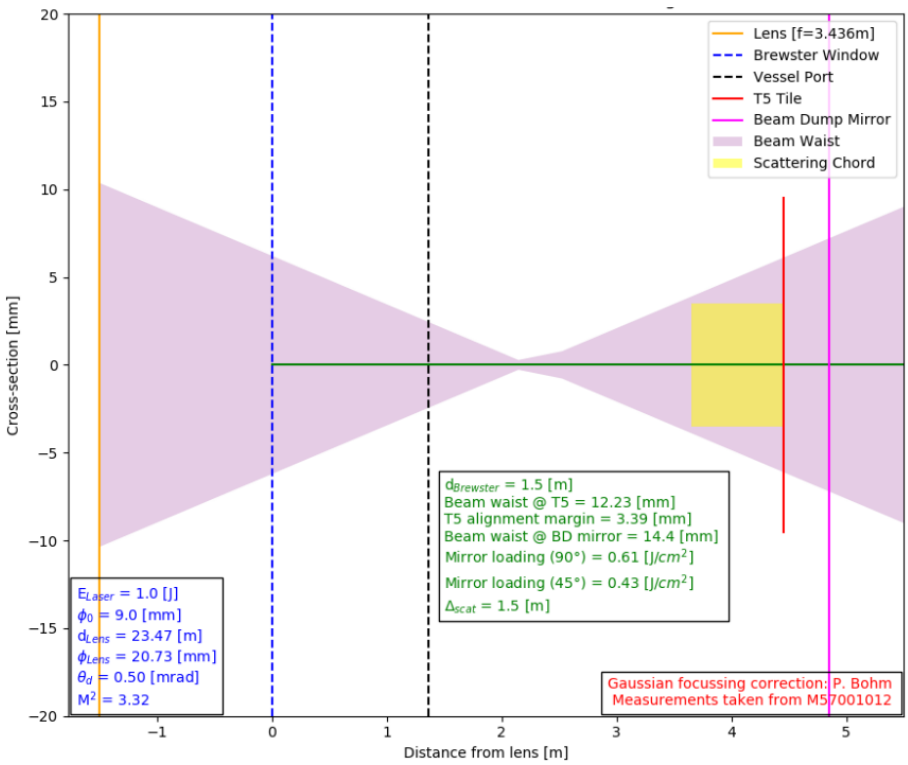

Figure C.4: Simulation of the laser beam focusing as described in subsection 3.2.1 with the lens positioned 1.5 m from the Brewster window

Bibliography

[1] J. Wesson. *Tokamaks*. 3rd ed. 2004.

[2] International Atomic Energy Agency. *Fusion Physics*. 2012.

[3] N. J. Peacock, D. C. Robinson, M. J. Forrest, P. D. Wilcock, and V. V. Sannikov. "Measurement of the Electron Temperature by Thomson Scattering in Tokamak T3". In: *Nature* 224 (5218 1969), pp. 488–490.

[4] J. R. Harrison. *MAST Upgrade Research Plan*. Culham Centre for Fusion Energy, 2019.

[5] J Milnes, N Ayed, F Dhalla, G Fishpool, J Hill, I Katramados, R Martin, G Naylor, T O'Gorman, and R Scannell. "MAST upgrade - Construction status". In: *Fusion Engineering and Design* 96-97 (2015).

[6] D. D. Ryutov and V. A. Soukhanovskii. "The snowflake divertor". In: *Physics of Plasmas* 22.11 (2015), p. 110901.

[7] P.M. Valanju, M. Kotschenreuther, and S.M. Mahajan. "Super X divertors for solving heat and neutron flux problems of fusion devices". In: *Fusion Engineering and Design* 85.1 (2010), pp. 46–52.

[8] R. Aymar, P. Barabaschi, and Y. Shimomura. "The ITER Design". In: *Plasma Phys. Control. Fusion* 44 (), p. 519.

[9] Howard Wilson, Ian Chapman, Tris Denton, William Morris, Bhavin Patel, Garry Voss, and Chris Waldon. *STEP—on the pathway to fusion commercialization*. 2053-2563. 2020.

[10] F. Wagner et al. "Regime of Improved Confinement and High Beta in Neutral-Beam-Heated Divertor Discharges of the ASDEX Tokamak". In: *Phys. Rev. Lett.* 49 (19 1982).

[11] A. Fil, B. Lipschultz, D. Moulton, A. Thornton, B. D. Dudson, O. Myatra, and K. Verhaegh. “Comparison between MAST-U conventional and Super-X configurations through SOLPS-ITER modelling”. In: *Nucl. Fusion* (62), p. 096026.

[12] J. Lovell, R. Stephen, S. Bray, G. Naylor, S. Elmore, H. Willett, M. Peterka, M. Dimitrova, A. Havranek, M. Hron, and R. Sharples. “A compact, smart Langmuir Probe control module for MAST-Upgrade”. In: *JINST* 12 (2017), p. C11008.

[13] G. De Temmerman, E. Delchambre, J. Dowling, A. Kirk, S. Lisgo, and P. Tamain. “Thermographic study of heat load asymmetries during MAST L-mode discharges”. In: *Plasma Phys. Control. Fusion* 52 (2010), p. 095005.

[14] X. Feng, A. Calcines, R. M. Sharples, B. Lipschultz, A. Perek, W. A. J. Vijvers, J. R. Harrison, J. S. Allcock, Y. Andrebe, B. P. Duval, and R. T. Mumgaard. “Development of an 11-channel multi wavelength imaging diagnostic for divertor plasmas in MAST Upgrade”. In: *Rev. Sci. Instrum.* 92 (2021), p. 063510.

[15] K. Verhaegh, B. Lipschultz, J. R. Harrison, N. Osborne, A. C. Williams, P. Ryan, J. Allcock, J. G. Clark, F. Federici, B. Kool, T. Wijkamp, A. Fil, D. Moulton, O. Myatra, A. Thornton, T. O. S. J. Bosman, C. Bowman, G. Cunningham, B. P. Duval, S. Henderson, and R. Scannell. “Spectroscopic investigations of detachment on the MAST Upgrade Super-X divertor”. In: *Nucl. Fusion* 63 (2023).

[16] J. G. Clark, M. D. Bowden, and R. Scannell. “Low temperature Thomson scattering on MAST-U”. In: *Rev. Sci. Instrum.* 92 (2021), p. 043545.

[17] J. G. Clark, M. D. Bowden, Y. Kim, B. Parry, E. Rose, R. Sarwar, and R. Scannell. “First divertor Thomson scattering measurements on MAST-U”. In: *Rev. Sci. Instrum.* 93 (2022), p. 103534.

[18] National Research Council. *Plasmas and Fluids*. National Academies Press, 1986.

[19] T. N. Carlstrom, J. H. Foote, D. G. Nilson, and B. W. Rice. “Design of the divertor Thomson scattering system on DIII-D”. In: *Rev. Sci. Instrum.* (1994).

[20] T. N. Carlstrom, D. N. Hill, C. L. Hsieh, R. Stockdale, and D. G. Nilson. “Initial operation of the divertor Thomson scattering diagnostic on DIII-D”. In: *Rev. Sci. Instrum.* (1996).

[21] B. Kurzan, A. Lohs, G. Sellmair, and M. Sochor. “Design and first measurements of the divertor Thomson scattering system on the ASDEX Upgrade tokamak”. In: *JINST* (2021).

[22] P. Blanchard, Y. Andrebe, H. Arnichand, R. Agnello, S. Antonioni, S. Couturier, J. Decker, T. De Kerchove D‘Exaerde, B.P. Duval, I. Furno, P.-F. Isoz, P. Lavanchy, X. Llobet, B. Marletaz, and J. Masur. “Thomson scattering measurements in the divertor region of the TCV Tokamak plasmas”. In: *JINST* 14 (2019), p. C10038.

[23] J. Hawke, R. Scannell, J. Harrison, R. B. Huxford, and P. Bohm. In: *JINST* 8 (2013), p. C11010.

[24] R. Scannell. “Investigation of H-mode edge profile behaviour on MAST using Thomson scattering”. PhD thesis. 2007.

[25] J. W. Berkery, S. A. Sabbagh, L. Kogan, D. Ryan, J. M. Bialek, Y. Jiang, D. J. Battaglia, S. Gibson, and C. Ham. “Kinetic equilibrium reconstructions ofplasmas in the MAST database andpreparation for reconstruction of thefirst plasmas in MAST upgrade”. In: *Plasma Phys. Control. Fusion* 63 (2021), p. 55014.

[26] A Kirk, T O’Gorman, S Saarelma, R Scannell, H R Wilson, and the MAST Team. “A comparison of H-mode pedestal characteristics in MAST as a function of magnetic configuration and ELM type”. In: *Plasma Physics and Controlled Fusion* 51 (2009).

[27] T. O’Gorman, G. Naylor, R. Scannell, G. Cunningham, K. J. Brunner, R. Martin, and D. Croft. “Design of a real-time two-color interferometer for MAST Upgrade”. In: *Rev. Sci. Instrum.* 85 (2014), p. 11D861.

[28] P. J. Ryan, J. W. Bradley, and M. D. Bowden. “Comparison of Langmuir probe and laser Thomson scattering for electron property measurements in magnetron discharges”. In: *Phys. Plasmas* 26 (2019), p. 073515.

[29] M. A. Law, F. Lockwood Estrin, M. D. Bowden, and J. W. Bradley. “Diagnosing asymmetric bipolar HiPIMS discharges using laser Thomson scattering”. In: *Plasma Sources Sci. Technol.* 30 (2021), p. 105019.

[30] S I Krasheninnikov and A S Kukushkin. “Physics of ultimate detachment of a tokamak divertor plasma”. In: *J. Plasma Phys* 83 (2017).

[31] A. Loarte, R. D. Monk, J. R. Martín-Solís, D. J. Campbell, A. V. Chankin, S. Clement, S. J. Davies, J. Ehrenberg, S. K. Erents, H. Y. Guo, P. J. Harbour, L. D. Horton, L. C. Ingesson, H. Jäckel, J. Lingertat, C. G. Lowry, C. F. Maggi, G. F. Matthews, K. McCormick, D. P. O'Brien, R. Reichle, G. Saibene, R. J. Smith, M. F. Stamp, D. Stork, and G. C. Vlases. "Plasma detachment in JET Mark I divertor experiments". In: *Nucl. Fusion* 38 (3 1998).

[32] F. F. Chen. *Introduction to Plasma Physics and Controlled Fusion: Volume 1: Plasma Physics*. Springer US, 1984.

[33] A. Piel. *Plasma Physics : An Introduction to Laboratory, Space, and Fusion Plasmas*. Springer, 2010.

[34] S. Kragh Nielsen. "Investigation of electron particle behaviour in the MAST spherical tokamak from Thomson scattering using Ruby laser and Nd YAG laser systems". PhD thesis. 2003.

[35] J. Sheffield, D. Froula, S. Glenzer, and N. Luhmman. *Plasma Scattering of Electromagnetic Radiation*. 2011.

[36] I. H. Hutchinson. *Principles of Plasma Diagnostics*. 2002.

[37] H. Bindslev. "On the Theory of Thomson Scattering and Reflectometry in a Relativistic Magnetized Plasma". PhD thesis. 1992.

[38] E. E. Salpeter. "Scattering of radio waves by electrons above the ionosphere". In: *Journal of Geophysical Research* 65 (1960), pp. 1851–1852.

[39] A. A. Ovsyannikov and M Zhukov. *Plasma diagnostics*. 2000, p. 575.

[40] M. J. van de Sande. "Laser scattering on low temperature plasmas : high resolution and stray light rejection". In: (2002).

[41] D E Evans and J Katzenstein. "Laser light scattering in laboratory plasmas". In: *Reports on Progress in Physics* 32 (1969), p. 305.

[42] R. E. Pechacek and A. W. Trivelpiece. "Electromagnetic Wave Scattering from a High-Temperature Plasma". In: *The Physics of Fluids* 10 (1967).

[43] J Sheffield. "The incoherent scattering of radiation from a high temperature plasma". In: 14 (1972).

[44] T Matoba, T Itagaki, T Yamauchi, and A Funahashi. “Analytical Approximations in the Theory of Relativistic Thomson Scattering for High Temperature Fusion Plasmas”. In: *Japanese Journal of Applied Physics* 18 (6 1979).

[45] V. A. Zhuravlev, G. D. Petrov, V. A. Zhuravlev, and G. D. Petrov. “Scattering of radiation by finite volumes of relativistic plasma streams”. In: *Soviet Journal of Plasma Physics* 5 (1979).

[46] A. C. Selden. In: *Phys. Lett. A* 79 (5-6) (1980), p. 405.

[47] Supriya Jaiswal. *Thomson Scattering*. 1995.

[48] G. Naylor. “Synchronization of Thomson scattering measurements on MAST using an FPGA based ”smart” trigger unit”. In: *Rev. Sci. Instrum.* 81 (2010), 10E110.

[49] Radiant ZEMAX. *ZEMAX® Optical Design Program User’s Manual*. 2011.

[50] S. Silburn, J. Harrison, T. Farley, J. Cavalier, S. Van Stroud, J. McGowan, A. Marignier, E. Nurse, C. Gutschow, M. Smithies, A. Wynn, and R. Doyle. *Calcam*. 2022.

[51] T. N. Carlstrom, J. C. DeBoo, R. Evanko, C. M. Greenfield, C. L. Hsieh, R. T. Snider, and P. Trost. In: *Rev. Sci. Instrum.* 61.10 (1990), pp. 2858–2860.

[52] R. Scannell, M. J. Walsh, P. G. Carolan, A. C. Darke, M. R. Dunstan, R. B. Huxford, G. McArdle, D. Morgan, G. Naylor, T. O’Gorman, S. Shibaev, N. Barratt, K. J. Gibson, G. J. Tallents, and H. Wilson. In: *Rev. Sci. Instrum.* 79 (2008), 10E730.

[53] R. Scannell, M. J. Walsh, M. R. Dunstan, J. Figueiredo, G. Naylor, T. O’Gorman, S. Shibaev, K. J. Gibson, and H. Wilson. In: *Rev. Sci. Instrum.* 81 (2010), p. 10D520.

[54] Schott. “Interference Filters Special Filters”. In: (2015).

[55] J. Hawke. “Measurement of electron kinetic profiles in the divertor region and during magnetic perturbations using Thomson scattering”. 2015.

[56] T. N. Carlstrom, G. L. Campbell, J. C. DeBoo, R. Evanko, J. Evans, C. M. Greenfield, J. Haskovec, C. L. Hsieh, E. McKee, R. T. Snider, R. Stockdale, P. K. Trost, and M. P. Thomas. “Design and operation of the multipulse Thomson scattering diagnostic on DIII-D”. In: *Rev. Sci. Instrum.* (1992).

[57] B. G. Streetman and S. Banerjee. *Solid state electronic devices*. 5th ed. Prentice Hall, 2000, p. 558.

[58] S. C. McCool, I. L. McCool, R. D. Bengston, and P. E. Phillips. *Calibration of Thomson scattering density measurements*. Tech. rep. University of Texas, 1981.

[59] B. P. Leblanc. "Thomson scattering density calibration by Rayleigh and rotational Raman scattering on NSTX". In: *Rev. Sci. Instrum.* 79 (2008), 10E737.

[60] F. Glass, T. N. Carlstrom, D. Du, A. G. McLean, D. A. Taussig, and R. L. Boivin. "Upgraded divertor Thomson scattering system on DIII-D". In: *Rev. Sci. Instrum.* 87 (2016).

[61] R. Scannell, M. Beurskens, M. Kempenaars, G. Naylor, M. Walsh, T. O'Gorman, and R. Pasqualotto. "Absolute calibration of LIDAR Thomson scattering systems by rotational Raman scattering". In: *Rev. Sci. Instrum.* 81 (2010).

[62] S. L. Prunty. "A primer on the theory of Thomson scattering for high-temperature fusion plasmas". In: *Phys. Scr.* 89 (12 2014).

[63] E. Havlickova, W. Fundamenski, M. Wischmeier, G. Fishpool, and D. Coster. In: *J. Nucl. Mater.* 438 (2013), S545.

[64] K. Verhaegh, B. Lipschultz, B. P. Duval, J. R. Harrison, H. Reimerdes, C. Theiler, B. Labit, R. Maurizio, C. Marini, F. Nespoli, U. Sheikh, C. K. Tsui, N. Vianello, and W. A. J. Vijvers. "Spectroscopic investigations of divertor detachment in TCV". In: *Nuclear Mater. Energy* 12 (2017), pp. 1112–1117.

[65] E. Havlíčková, M. Wischmeier, B. Lipschultz, and G. Fishpool. "The effect of the Super-X divertor of MAST Upgrade on impurity radiation as modelled by SOLPS". In: *Journal of Nuclear Materials* 463 (2015), pp. 1209–1213.

[66] K. Verhaegh, B. Lipschultz, B. P. Duval, A. Fil, M. Wensing, C. Bowman, and D. S. Gahle. "Novel inferences of ionisation and recombination for particle/power balance during detached discharges using deuterium Balmer line spectroscopy". In: *Plasma Phys. Control. Fusion* 61 (12 2019), p. 125018.

[67] K. Verhaegh, B. Lipschultz, J. R. Harrison, B. P. Duval, A. Fil, M. Wensing, C. Bowman, D. S. Gahle, A. Kukushkin, D. Moulton, A. Perek, A. Pshenov, F. Federici, O. Février, O. Myatra, A. Smolders, and C. Theiler. "The role of plasma-molecule interactions on power and particle balance during detachment on the TCV tokamak". In: *Nucl. Fusion* 61 (10 2021), p. 106014.

[68] K. Verhaegh, B. Lipschultz, C. Bowman, B. P. Duval, U. Fantz, A. Fil, J. R. Harrison, D. Moulton, O. Myatra, D. Wünderlich, F. Federici, D. S. Gahle, A. Perek, and M. Wensing. "A novel hydrogenic spectroscopic technique for inferring the role of plasma–molecule interaction on power and particle balance during detached conditions". In: *Plasma Phys. Control. Fusion* 63 (2021), p. 035018.

[69] K. Verhaegh, B. Lipschultz, J.R. Harrison, B. Duval, C. Bowman, A. Fil, D. Singh Gahle, D. Moulton, O. Myatra, A. Perek, C. Theiler, and M. Wensing. "A study of the influence of plasma–molecule interactions on particle balance during detachment". In: *Nuclear Materials and Energy* 26 (2021).

[70] F. Militello, L. Garzotti, J. Harrison, J. T. Omotani, R. Scannell, S. Allan, A. Kirk, I. Lupelli, and A. J. Thornton. "Characterisation of the L-mode scrape off layer in MAST: Decay lengths". In: *Nucl. Fusion* 56 (1 2016).

[71] J. Lovell, M. L. Reinke, A. R. Field, B. A. Lomanowski, and MAST Upgrade Team. "Overview and first measurements of the MAST Upgrade bolometer diagnostic". In: *Review of Scientific Instruments* 94 (2 2023), p. 023509.

[72] F. Federici, M. Reinke, B. Lipschultz, A. Thornton, J.R. Harrison J. Lovell, M. Bernert, and MAST Upgrade Team. "Design and implementation of a prototype infrared video bolometer (IRVB) in MAST Upgrade". Article Submitted. 2023.

[73] Graham McArdle, Luigi Pangione, and Martin Kochan. "The MAST Upgrade plasma control system". In: *Fusion Engineering and Design* 159 (2020), p. 111764.

[74] K J Gibson, N Barratt, I Chapman, N Conway, M R Dunstan, A R Field, L Garzotti, A Kirk, B Lloyd, H Meyer, G Naylor, T O'Gorman, R Scannell, S Shibaev, J Snape, G J Tallents, D Temple, A Thornton, S Pinches, M Valovic, M J Walsh, and H R Wilson. "New physics capabilities from the upgraded Thomson scattering diagnostic on MAST". In: *Plasma Phys. and Control. Fusion* 52 (12 2010), p. 124041.

[75] Excelitas Technologies. *Avalanche Photodiode*. 2011.

[76] Solid State Division. *Characteristics and use of Si APD (Avalanche Photodiode)*. 2004.

[77] E.E. Mukhin, R.A. Pitts, P. Andrew, I.M. Bukreev, P.V. Chernakov, L. Giudicotti, G. Huijsmans, M.M. Kochergin, A.N. Koval, A.S. Kukushkin, G.S. Kurskiev, A.E. Litvinov, S.V. Masyukevich, R. Pasqualotto, A.G. Razdobarin, V.V. Semenov, S.Yu. Tolstyakov, and M.J. Walsh. "Physical aspects of divertor Thomson scattering implementation on ITER". In: *Nuclear Fusion* 54 (4 2014), p. 043007.

[78] Matthew Rogers. *A Low Cost Laser Thomson Scattering System*. 2015.

[79] M. Walsh, N. Conway, M. Dunstan, M. Forrest, and R. Huxford. "Interactive optical design and realization of an optimized charge coupled device Thomson scattering system for the spherical tokamak START". In: *Rev. Sci. Instrum.* 70 (1999).

[80] D. G. Nilson, D. N. Hill, J. C. Evans, T. N. Carlstrom, C. L. Hsieh, and R. E. Stockdale. "Thomson scattering stray light reduction techniques using a CCD camera". In: *Rev. Sci. Instrum.* (1998).

[81] J. Figueiredo, G. Naylor, M. Walsh, M. Dunstan, R. Scannell, and F. Serra. "MAST YAG Thomson scattering upgrade alignment system". In: vol. 81. 2010.

[82] William Morris, Joe Milnes, Tom Barrett, Clive Challis, Ian Chapman, Martin Cox, Geof Cunningham, Fahim Dhalla, Geoff Fishpool, Philippe Jacquet, Ioannis Katramados, Andrew Kirk, Ken McClements, Richard Martin, Hendrik Meyer, Michele Romanelli, Samuli Saarelma, Sergei Sharapov, Vaughan Thompson, Martin Valovic, Glenn Whitfield, and Dan Wolff. "MAST accomplishments and upgrade for fusion next-steps". In: *IEEE Transactions on Plasma Science* (2014).

[83] L. A. Berni and B. F C Albuquerque. "Stray light analysis for the Thomson scattering diagnostic of the ETE Tokamak". In: *Rev. Sci. Instrum.* 81 (12 2010).

[84] James Harrison. "Characterisation of Detached Plasmas on the MAST Tokamak". 2010.

[85] R Scannell, A Kirk, N Ben Ayed, P G Carolan, G Cunningham, J McCone, S L Prunty, and M J Walsh. "Experimental investigation into ELM filament formation on MAST". In: *Plasma Phys. Control. Fusion* 49.9 (2007), p. 1431.